Louisiana State University
LSU Digital Commons

LSU Doctoral Dissertations | Graduate School

2008

An investigation into fuel cells and flow cytometers optimal design

Etim Sunday Udoetok
Louisiana State University and Agricultural and Mechanical College

Follow this and additional works at: https://digitalcommons.lsu.edu/gradschool_dissertations

 Part of the Mechanical Engineering Commons

Recommended Citation
Udoetok, Etim Sunday, "An investigation into fuel cells and flow cytometers optimal design" (2008). *LSU Doctoral Dissertations*. 1638.
https://digitalcommons.lsu.edu/gradschool_dissertations/1638

This Dissertation is brought to you for free and open access by the Graduate School at LSU Digital Commons. It has been accepted for inclusion in LSU Doctoral Dissertations by an authorized graduate school editor of LSU Digital Commons. For more information, please contactgradetd@lsu.edu.

AN INVESTIGATION INTO FUEL CELLS AND FLOW CYTOMETERS OPTIMAL DESIGN

A Dissertation

Submitted to the Graduate Faculty of the
Louisiana State University and
Agricultural and Mechanical College
in partial fulfillment of the
requirements for the degree of
Doctor of Philosophy

in

The Department of Mechanical Engineering

By

Etim S. Udoetok
B.S., Louisiana State University, 2004
August 2008

ACKNOWLEDGEMENTS

With great pleasure, I thank my major professor, Dr. Tryfon Charalampopoulos, for taking his time to supervise my work on this dissertation. Secondly, I thank all the members of my examining committee for taking part in examining my work on this dissertation. I thank my laboratory colleagues, my roommates, friends and all well-wishers at LSU who directly or indirectly contributed to providing a friendly atmosphere that was conducive for my stay and work on this dissertation.

PREFACE

This research work deals with two subtopics; namely, the optimal design of fuel cells and flow cytometers. Practically, fuel cells have very little or no connection with flow cytometers; however, the two topics have been brought together under one title because a common tool, which is fluent Computational Fluid Dynamics code, was used to perform greater parts of the research work on both systems.

TABLE OF CONTENTS

LIST OF TABLES

LIST OF FIGURES

LIST OF SYMBOLS AND NOMENCLATURE

A	Area
AFC	Alkaline fuel cell
c_i	Molar concentration of specie i
C	Experimental correction factor
CFD	Computational Fluid Dynamics
D, d	Diameter
D_i	Diffusivity of specie i
err	Error (+/- Value)
E	Voltage, Electromotive force
Eqn(s).	Equation(s)
F	Faradays constant
Fig(s).	Figure(s)
FC	Fuel cell
g	Gravitational constant
G	Gibbs free energy
H	Enthalpy
i	Current per unit area
I	Current (Amps)
ICE	Internal Combustion Engine
KOH	Potassium hydroxide
L	Membrane thickness
n	Number of moles
n_e	Number of electrons

n_p	Number of protons
M	Mass
P	Pressure
PAFC	Phosphoric Acid Fuel Cell(s)
PEM	Polymer electrolyte membrane
Q	Heat
q	Charge
R	Universal gas constant
Re	Reynolds number
Ref.	Reference
S	Entropy
SOFC	Solid Oxide Fuel cell
t	Time
V	Volume, Voltage
Y	Mass fraction
β	Number
ρ	Density
η	Efficiency
Δ	Change
μ	Viscosity

Subscripts:

a	Anode
c	Cathode
e	Electron

f	Final
H	Henry
j	Specie
m	Membrane
o	Standard state
opt	Optimum
r	Reversible

Superscripts:

o	Standard state
θ	Property at Temperature, T = 298K

ABSTRACT

The aim of the fuel cells part of this project was to investigate the performance of Proton Exchange Membrane Fuel Cells and closely related fuel cell types like the Alkaline Fuel Cells and Phosphoric Acid Fuel Cells. The investigation involved understanding the performance of fuel cells, addressing the shortcomings of currently used designs, and finding new methods for improving the performance of fuel cells. CFD was used to study flow channels and information learned from the study was used to design a new and improved flow channel. A prototype of the new design was fabricated, tested and found to perform better than conventional designs. Protons mass flow equation and equation for the diffusivity of hydrogen protons in PEM were derived. In addition, the effects of electrodes area ratio on selected fuel cells were studied theoretically and experimentally.

The aim of the second part of this work was to model flow cytometers using fluent, which is the same CFD code used in the first part, and use the simulation result to optimize the design. Ren Yang [1, 2] designed the flow cytometers that were simulated. It was observed from the simulation results that blood cells were hydrodynamically focused within a range of sheath flow rate, and it was observed that bigger flow cytometer exit pipe diameter requires higher sheath flow rates for hydrodynamic focusing of blood cells. The simulation results were compared to the result from Ren Yang's experiments and both results matched under the same flow conditions. Plots of the trajectories of blood cells, animation of the performance of the flow cytometer, and recommended operational flow rates for the given flow cytometer shape configurations were obtained from the simulation result. The simulation result was used to obtain an optimized design by making geometric configuration changes to correct the shortcomings in the original design. The optimized design was modeled and simulated. A comparison of the optimized design simulation results and the original design simulation results showed that the

hydrodynamic focusing of the optimized design was better. Quantitatively, for a sheath flow of 0.000018 kg/s, the optimized design has 300% improvement in hydrofocusing effect compared to the original design.

1. INTRODUCTION

Since the invention of fuel cell in 1839, the development of fuel cells has been slow compared to other power generation systems like the internal combustion engine. The current need for more efficient and clean power generation systems has renewed interest in the development of fuel cells. Practical fuel cells operate at efficiencies lower than the theoretically expected values, so most research works on fuel cells are aimed at improving fuel cells performance. In the past, research work on fuel cells involved only theoretical and experimental work, but with the development of computers and Computational Fluid Dynamics (CFD), it now involves computational work. CFD modeling of a Proton Exchange Membrane (PEM) fuel cell requires the knowledge of the transport property of protons in PEM. The most widely used model for the transport of protons in PEM was developed by Yeo and McBreen [3], but a careful study of their work reveals that their work was done with a fuel cell setup which is different from the typical setup of a PEM fuel cell. Therefore, a new transport model for protons in PEM was developed in this study. The new transport model was used in the CFD modeling of a PEM fuel cell, and the modeling result was used to study and design a PEM fuel cell flow field. The flow field developed in this project involved the combination of parallel and serpentine flow field designs and the specification of serpentine straight path length for high performance. Experiments showed that the new design actually performed better. The use of CFD as an aid in the design of PEM fuel cell flow field is not novel, so current related works were reviewed and compared. Additionally, the effect of equal electrodes area on the performance of a fuel cell was studied. Experiments showed that the electrode area ratio affects the efficiency of PEM fuel cells and adjusting the area ratio can be used to obtain higher efficiencies in PEM fuel cells operating at low current, i.e. low electrical load.

Early flow cytometers were used to count and sort cells only. In the 1990s, computer technology was incorporated into flow cytometers, and this resulted in higher cell counting rate and added ability to read off several data from individual cells. This computerization of flow cytometry requires an improvement of the flow chamber design for better hydrodynamic focusing of the blood cells. Therefore, fluent CFD code was used to simulate flow cytometry in the second part of this research work. Flow cytometers are usually tested experimentally using flourecein dyed micro-spheres and there is no known flow cytometry computational modeling work. Therefore, in this project, it was demonstrated that it is possible to model flow cytometry with fluent. The simulation results were compared to experimental results and were used to optimize the flow cytometer design. Simulations of the optimized model showed improved performance of the flow cytometer.

Concisely, this research work provides the following:

1 Brief introductions to CFD, fuel cells and flow cytometry.

2 New expressions for the mass flow rate of hydrogen protons and the diffusivity of hydrogen protons in a PEM based on the electrochemical process in a PEM fuel cell.

3 An answer to why specially designed flow fields improve the performance of fuel cells, and an improved flow field design for a PEM fuel cell.

4 An answer to what effect the use of electrodes with equal areas has on the performance of fuel cells, the limiting efficiency of some fuel cell with equal electrodes area, and a method of changing electrodes area ratio to obtain high efficiency.

5 A CFD simulation of a flow cytometer, and an optimized design of a flow cytometer

The next chapter deals with the fuel cells part of the study.

2. AN INVESTIGATION INTO THE PERFORMANCE OF PEM FUEL CELLS

2.1 Introduction to Fuel Cells

2.1.1 Background

William Grove, who was a British professor of experimental philosophy, invented fuel cell in 1839. The first fuel cell consisted of a series of cells made with a dilute solution of sulphuric acid and pairs of test tubes of Hydrogen and Oxygen (See Fig. 2.1 below.) Grove observed that the ratio of consumption of the Hydrogen to Oxygen was 2:1. The volume ratio is in agreement with the simple reaction equation of Hydrogen with Oxygen to produce water.

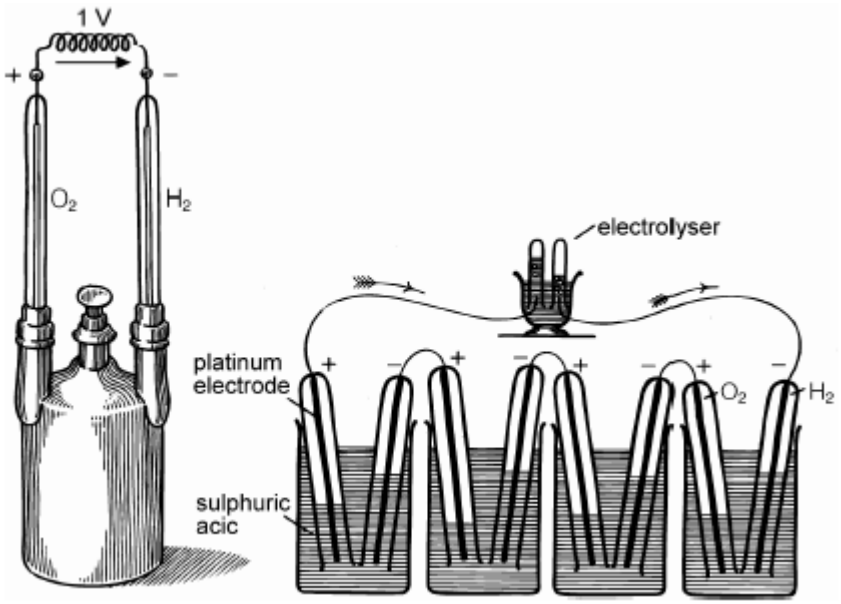

Figure 2.1: Grove's 'gas battery' (1839) produced a voltage of about 1 volt, shown left. Grove's 'gas chain' powering an electrolyzer (1842), shown right. [4].

William Grove also conducted other experiments with different electrolytes and fuels. He made this famous quote; "Every chemical synthetic action may by a proper disposition of the constituents, be made to produce a voltaic current." [5]

True to Grove's quote, other types of fuel cells have been developed over the years, and some of these fuel cells include the following:

1. Proton Exchange Membrane(PEM)
2. Solid Oxide Fuel Cell (SOFC)
3. Phosphoric Acid Fuel Cell
4. Alkaline Fuel Cell (AFC)
5. Molten Carbonate Fuel Cell
6. Direct Methanol Fuel Cell

Let's briefly discuss the above fuel cells. **Alkaline fuel cells** use potassium hydroxide (KOH) solution as electrolyte. Increase in the concentration of the KOH electrolyte results in increase of operating temperature and pressure. KOH has a very high conductance, and does not require the use of noble metal electro catalysts in the electrode. Alkaline fuel cells were initially very costly, but some companies have continuously reduced the cost. AFCs in the market have power output of 300Watts to 5 kW per cell and have an average efficiency of 70%. In most cases, water is removed by evaporation. At the anode, hydrogen oxidation still accounts for 20% of total polarization at high current densities. At the cathode, oxygen reduction is reversible, and the formation of hydrogen peroxide is a reaction that must be avoided, because it deteriorates the carbon based support. Operation at higher temperature (above room temperature) is very favorable for the oxygen reduction. AFCs are stable, reliable, and can provide several thousand hours of operation. AFCs operate within the temperature range of 90-100 ^{o}C. [5, 6, 7]

The **Proton Exchange Membrane (PEM) fuel cell** consists of a solid polymeric membrane, which acts as the electrolyte. Typical PEM FCs in the market have power outputs of 50 to 250 kW per cell and have efficiencies of 40-50%. PEM FCs have neither cracking problems nor leakage problem, because their electrolyte is a solid film. PEM FCs operate within the temperature range of 60-100^{o}C. These FCs use platinum-catalyzed porous electrodes, which are costly. PEM FCs are very sensitive to impurities. Carbon based impurities in the fuel causes

degradation of the electrolytic membrane, so high purity fuels are desirable for PEM FCs. A schematic diagram of a PEM Fuel Cell is given in Fig. 2.2. [5, 6, 7]

Phosphoric acid fuel cells are fuel cells that use phosphoric acid as electrolyte. They reject CO_2, and tolerate small amounts of CO. Phosphoric acid has good electrolyte conductivity at temperatures above 150 ^oC. Phosphoric acid fuel cells have efficiency of 40-80%, and operate between the temperatures of 150-200 ^oC. PAFCs use expensive platinum electrodes. PAFCs generally have a large size and weight to accommodate the high temperature and pressure [5, 6, 7]. Fig. 2.2 shows how a PAFC and PEM work.

Solid Oxide Fuel Cells are all solid-state electrochemical systems. SOFC uses ceramic material of solid zirconium oxide and small amount of ytrria as electrolyte. SOFCs have an operating temperature range of 600-1000^oC, and efficiency of up to 60%. The high operating temperature of SOFC limits its application, and its units are usually very large. The solid electrolyte of SOFCs has the advantage of not leaking, but it can crack. [5, 6, 7]

In **Molten Carbonate Fuel Cells**, Molten alkali carbonate (like sodium or magnesium carbonate) is used as the electrolyte. Efficiency ranges from 60-80%, and it operates within the temperature range of 600-1000 ^oC. The alkali carbonate electrolytes used have high conductivity at high temperatures; hence, it is operated at high temperature. It requires the use of noble metal catalysts, which are very expensive. A disadvantage common to the SOFC and MCFC is that their high operating temperature promotes corrosion and breakdown of fuel cell components. Due to the high operation temperatures of SOFC and MCFC, they are usually used as hybrid in combination with steam or gas power generation systems. [5, 6, 7]

DMFC uses a polymer membrane as the electrolyte, has cell efficiency of up to 40%, and operates within the temperature range of 50-100^oC. DMFC draws hydrogen directly from liquid

methanol. A major problem with it is that fuel sometimes crosses from the anode to the cathode without producing electricity. [5, 6, 7]

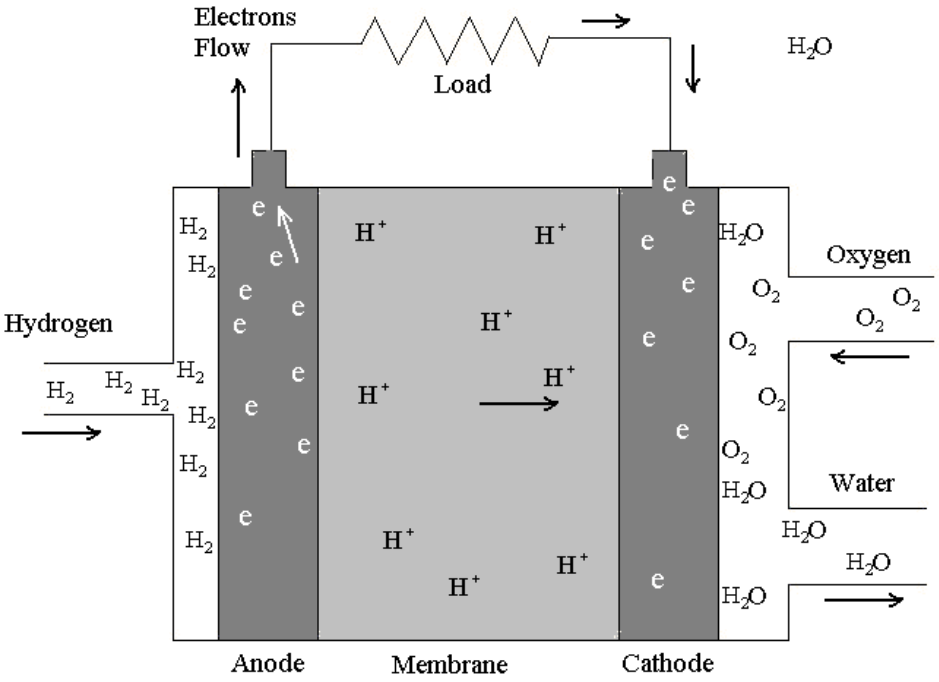

Figure 2.2: How PAFC and PEM fuel cells work (Drawn to match [5, 6, and 7])

2.1.2 Fuel Cell Applications

Fuel cells have been widely used for power generation over the last two decades and are very attractive alternatives to Internal Combustion Engines (ICEs) because of their high efficiency and non-polluting operation. Fuel cells have been used to power spacecrafts, automobiles and buses. Some mini power plants that use fuel cells have been built; such power plants deliver 5-10KW of power. Some portable fuel cells have also been developed for use in powering of electronic devices for camping, yachting, traffic monitoring, medical treatment, and warfare. In general, fuel cells produce electricity and can power any device or equipment that runs on electricity. Once again, the main advantage of fuel cell application is that it does not emit pollutants like carbon dioxide, the green house gas well known for its global warming effect [7].

2.1.3 Fuel Cells Operational Principles

A fuel cell is an electrochemical device that combines hydrogen and oxygen to produce electricity and waste products of heat and water. In parallel with this definition, Fig. 2.3 gives a typical functional diagram of a fuel cell. In reality, the individual subsystems are more complex.

In a typical PEM FC in operation, at the node, hydrogen atoms electrochemically split into electrons and protons. The split is enhanced by the potential of the electrode cell couple and effect of electrode catalysts. The electrons flow through the circuit to the anode, while the hydrogen ions (protons) diffuse through the electrolyte to the cathode. At the cathode, hydrogen protons combine with electrons and oxygen to produce water and heat. The flow of electrons through the circuit provides useful power for the load (see Fig. 2.3).

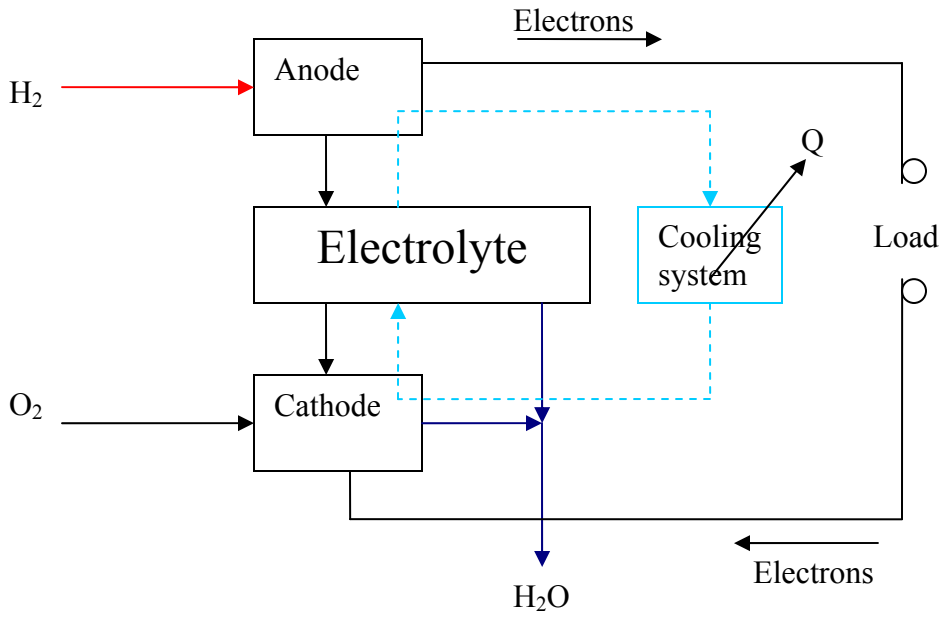

Figure 2.3: Functional diagram of a typical fuel cell system

The half-cell electrochemical reactions that occur at the electrodes are driven by electrode potential and catalysis. These reaction equations form the basis for the operation of the fuel cells. Table 2.1 gives some of these reaction equations for common fuel cells. Common to all the fuel

cell reactions is the liberated electrons, which flow to provide electrical current. It can also be seen that the reactions at the anode and cathode are different and connect to form the overall reaction.

Some important fuel cell mathematical equations, terms, and definitions are usually used along with the chemical reaction equations to thermodynamically analyze fuel cells. The electrical energy generated by a fuel cell is the change in free energy from its overall chemical reaction given as

$$\Delta G^o = -nFE_r^o \qquad \text{(eqn. 1), [Ref. 5]}$$

where n is the number of moles of electrons, F is Faradays constant, and E_r^o is the difference between anode potential and cathode potential. E_r^o depends on the reacting chemical species. The reversible cell potential derived from eqn. 1 is given as

$$E_r = E_r^o - \frac{(\Delta n)RT.Ln(P)}{nF} \qquad \text{(eqn. 2), [Ref. 5]}$$

where R is gas constant, T is temperature and P is pressure.

The heat supplied to the fuel cell is the change in enthalpy of the overall fuel cell reaction. Therefore, using eqn. 1 and the definition of efficiency, the efficiency of a fuel cell is given as

$$\eta = \frac{\text{Produced Electrical Energy}}{\text{Total Thermal Energy Produced During the Reaction}} = \frac{nFE}{\Delta H} = \frac{\Delta G}{\Delta H} = \frac{\Delta H - T\Delta S}{\Delta H} = 1 - \frac{T\Delta S}{\Delta H} \qquad \text{(eqn. 3), [Ref. 5]}$$

where ΔH is enthalpy change, and ΔS is the entropy change of the overall reaction equation. The enthalpy change is evaluated using higher heating value.

As an example of the application of some of the above equations, consider a PEM fuel cell operating under standard state conditions.

Table 2.1: Common fuel cells reaction equations

FUEL CELL	ELECTROLYTE	ELECTRODE	T RANGE (^{O}C)	ANODE REACTION	CATHODE REACTION	OVERALL REACTION
AFC	KOH	Ni-based	60-100	$H_2 + 2(OH)^- \rightarrow 2H_2O + 2e^-$	$\frac{1}{2}O_2 + H_2O + 2e^- \rightarrow 2(OH)^-$	$H_2 + \frac{1}{2}O_2 \rightarrow H_2O$
PEM	Poly-perflourosulfonic acid	Pt-based	60-100	$H_2 \rightarrow 2H^+ + 2e^-$	$\frac{1}{2}O_2 + 2H^+ + 2e^- \rightarrow H_2O$	$H_2 + \frac{1}{2}O_2 \rightarrow H_2O$
PAFC	$H_4P_2O_7$	Pt-based	150-225	$H_2 \rightarrow 2H^+ + 2e^-$	$\frac{1}{2}O_2 + 2H^+ + 2e^- \rightarrow H_2O$	$H_2 + \frac{1}{2}O_2 \rightarrow H_2O$
SOFC	YSZ(ZrO & Y_2O_3 based)	Ni-ZrO_2 & $La_{1-x}Sr_xMnO_3$	600-1000	$H_2 + O^{2-} \rightarrow H_2O + 2e^-$	$\frac{1}{2}O_2 + 2e^- \rightarrow O^{2-}$	$H_2 + \frac{1}{2}O_2 \rightarrow H_2O$
MCFC	Li_2CO_3 & K_2CO_3	Ni-Cr & Litiated NiO	600-1000	$H_2 + CO_3^{2-} \rightarrow H_2O + CO_2 + 2e^-$	$\frac{1}{2}O_2 + CO_2 + 2e^- \rightarrow CO_3^{2-}$	$H_2 + \frac{1}{2}O_2 + CO_2 \rightarrow H_2O + CO_2$
DMFC	Poly-perflourosulfonic acid	Platinum-based	50-100	$CH_3OH + H_2O \rightarrow CO_2 + 6H^+ + 6e^-$	$\frac{3}{2}O_2 + 6H^+ + 6e^- \rightarrow 3H_2O$	$CH_3OH + \frac{3}{2}O_2 + H_2O \rightarrow CO_2 + 3H_2O$

From Table 2.1, the overall reaction is $H_2 + \frac{1}{2} O_2 \rightarrow H_2O$

Enthalpy change, $\Delta H = h^o_{f_{H_2O}} - h^o_{f_{H_2}} - \frac{1}{2} h^o_{f_{O_2}} = h^o_{f_{H_2O}} = -241820$ kJ

Entropy change, $\Delta S = s_{H_2O} - s_{H_2} - \frac{1}{2} s_{O_2} = -44.16$ kJ/K

Standard state emf using eqn. 1: $E = \frac{-\Delta G}{nF} = \frac{-(\Delta H - T\Delta S)}{nF} = 1.185$ V

Efficiency using eqn. 3: $\eta = \frac{\Delta G}{\Delta H} = .945 \cong 94.5\%$

The results obtained in the example above show that the efficiency of a typical fuel cell is high compared to the maximum efficiency of a heat engine, but practical values of fuel cell efficiencies are always lower than the theoretical values due to losses. In summary, fuel cells have been introduced as a simple power generation device with potential to perform with high efficiency.

In the next section, the development of a new expression for proton transport through PEM used in fuel cell is presented.

2.2 Protons Mass flow and Diffusivity through PEM

2.2.1 Introduction to PEMs

Proton exchange membranes (PEM) are membranes made from ionomers and are designed to conduct protons while being impermeable to gases and electrons [7]. PEMs have the advantages of chemical inertness, mechanical stability and thermal stability when applied in fuel cells. PEMs are water absorbent and electrolytic in nature, so they are also called polymeric electrolyte membrane. The mass flow rate of protons needs to be known, because it will be used in the computational simulation of the performance of fuel cell in this project. There are existing methods of finding protons mass flow through PEM. These existing methods, which include the use of proton diffusivity and/or mobility, have some limitation as discussed in section 2.2.3. To

obtain high accuracy in the fuel cells simulation, a new equation was derived for the diffusivity of protons through the membrane of a PEM fuel cell in section 2.2.4.

2.2.2 Theories and Mechanism of Proton Transport in PEM

There are two existing theories for explaining transport through membranes. The first is the **solution-diffusion theory**, which explains that permeant dissolves in membrane, and diffuses through the membrane. The second is the pore flow theory, which explains that permeant flows through micro or nano pore in the membrane. I.e., the second theory models the membrane as a porous material. [8]

In PEM FCs, the transport of protons through PEM is more of a diffusion process than pore flow. This is because the protons dissolve into the water content of PEM, form an aqueous solution and transport through the membrane. The aqueous formed by dissolving the proton is a mixture of H_3O^+, H_2O and H^+. [9, 10] The protons are transported due to electric field influence, due to movement of protonic species carrying some protons, and due to concentration gradient. The protonic species or proton carrying species includes H_3O^+ and $H^+.nH_2O$. As additional detail, the PEM matrix (or structure) contains fixed ionic groups (also known as functional sites or ionizable groups) whose charges are compensated by mobile ions, which can be exchanged with adjoining media. In other words, the mobile ions move through the membrane by passing from one ionic group to the other in a direction across the membrane. This contributes to the electric field influence on proton transport. [9, 10]

Fig. 2.4 shows a schematic of the ionic transport of PEM. In Fig. 2.4, the back diffusion of water shown contributes to maintaining the concentration gradient.

2.2.3 Literature Review of PEM Transport Properties Advances

Yeo and McBreen [3] used an experiment and the Arrhenius equation to develop the proton diffusivity as a function of temperature. The experiment they performed involved using

hydrochloric acid as solvent and source of the reactants, so their experimental setup was different from the commonly used fuel-oxidizer setup shown in Fig. 2.2.

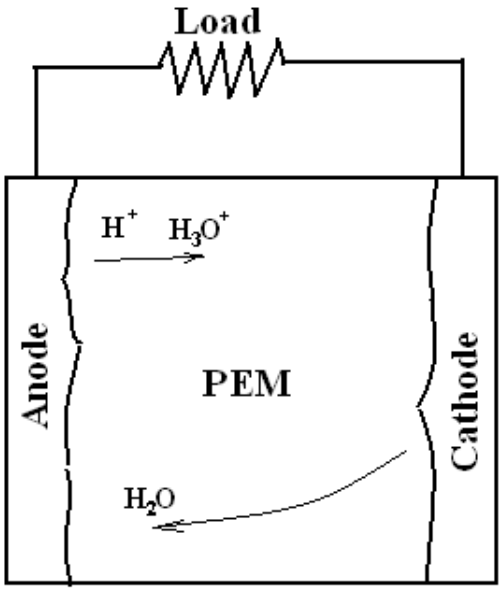

Figure 2.4: Ions transport through PEM due to electro-osmotic pressure [8]

The Arrhenius equation relates a chemical reaction rate to temperature. The diffusivity equation they developed is given in eqn. 4 below

$$D_H = 4.1\times10^{-7}\exp\left(-\frac{2602}{T}\right) \qquad (4)$$

where D_H is in m^2/s and T is in degree Kelvin. Their equation is widely used, e.g. it is used in Fluent fuel cell model.

Din and Michaelis [11] simulated the transport of water and protons through PEM by assuming that the membrane is a band of parallel pores through which protons and water pass. They treated the protons and water molecules as particles whose motions were driven by electrostatic interaction with the pore walls. Their work was based on statistical pore size

distribution, was more of statistical mechanics and agreed with the second theory of membrane transport.

The above review introduced current related research work and the next section will outline the derivation of the mass flow rate of protons in an operational PEM fuel cell.

2.2.4 Protons Mass Flow through PEM

In order to find protons mass flow through PEM, it was assumed that the membrane is moist, and has constant moisture content. Practically, PEM can conduct protons only when moist. PEM fuel cells will not work when the membrane is dry, because the membrane works by having the hydrogen protons dissolve into its water content, form an aqueous solution, and then the protons diffuse. Constant moisture content is assumed to ensure that membrane does not dry out during operation. Effects of moisture content on fuel cell operation will automatically show as change in the current density. I.e. as the moisture content decreases, the current density decreases. Note that current density is zero when moisture content is zero, no matter what size of electrical load is applied. Therefore, the changes in diffusivity of PEM due to moisture change will automatically show up due to the change in current density (see eqn. 26). Practically, water is produced in the fuel cells and additional humidification systems are used in complex systems to keep the membrane moist. PEM fuel cells operate at temperatures below the boiling point of water (see Table 2.1), so the water loss rate is low. It is known from the definition of PEM that the membrane conducts protons only and is impervious to hydrogen gas. Consider Fig. 2.2, at the anode of the fuel cell, hydrogen atoms dissociate into electrons and protons. The electrons flow through the circuit with electrical load, while the protons diffuse through the membrane. By conservation of mass at the anode (see Fig. 2.5),

$$\dot{m}_H = \dot{m}_{e^-} + \dot{m}_{H^+} \qquad (5)$$

where $\dot{m}_H$, $\dot{m}_{e^-}$, and $\dot{m}_{H^+}$ are the mass flow rates of hydrogen, electrons and protons respectively.

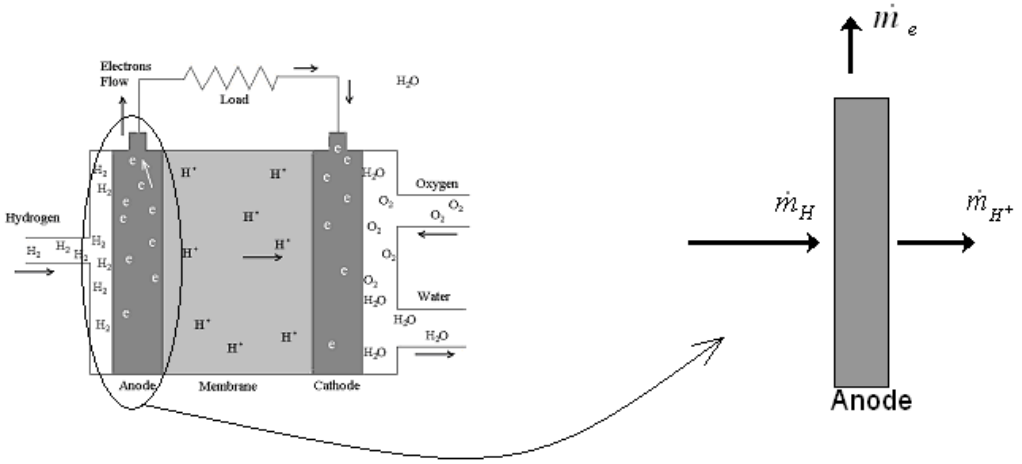

Figure 2.5: Dissociation of hydrogen at the anode.

Theoretically, the mass flow rate of the electrons is found by measuring the current. From the definition of current,

$$I = \frac{dq}{dt} = \frac{d(n_e q_e)}{dt} = \frac{d}{dt}\left(\frac{m_e}{M_e} q_e\right) = \frac{q_e}{M_e}\frac{d}{dt}(m_e) = \frac{q_e}{M_e}\dot{m}_e$$

where I is current, t is time, q_e is charge on an electron, and M_e is the mass of an electron. Therefore, the mass flow rate of the electrons is

$$\dot{m}_e = \frac{I \cdot M_e}{q_e} \qquad (6)$$

One hydrogen atom is made up of an electron and a proton. At the anode, the electron and protons are separated. Therefore, for every one electron flowing through the circuit, there is a corresponding one proton flowing through the membrane, and this is mathematically expressed as

$$\dot{n}_{e^-} = \dot{n}_{H^+} \tag{7}$$

where $\dot{n}_{e^-}$, $\dot{n}_{H^+}$ are the number of electrons flowing through the circuit per unit time and the number of protons flowing through the membrane per unit time. In terms of mass flow rate, eqn. 7 becomes

$$\frac{d}{dt}\left(\frac{m_{e^-}}{M_{e^-}}\right) = \frac{d}{dt}\left(\frac{m_{H^+}}{M_{H^+}}\right)$$

$$\frac{\dot{m}_{H^+}}{M_{H^+}} = \frac{\dot{m}_e}{M_e} \tag{8}$$

where M_H is the mass of one proton. Substituting eqn. 8 into eqn. 6 yields the mass flow rate of protons through the membrane,

$$\dot{m}_{H^+} = \frac{I \cdot M_{H^+}}{q_e} \tag{9}$$

Eqns. 9 and 6 into eqn. 5 gives

$$\dot{m}_H = \frac{I \cdot \left(M_{H^+} + M_e\right)}{q_e} \tag{10}$$

The current, I, is the only unknown variable which can be measured by using an ammeter as shown in Fig. 2.6. Consider the whole fuel cell as a volume absorbing hydrogen gas, the mass flow rate of hydrogen gas is given as

$$\dot{m}_{H_2} = \dot{m}_H = \frac{I \cdot \left(M_{H^+} + M_e\right)}{q_e} \tag{11}$$

where $\dot{m}_{H_2}$ is in kg/s, I in is Amps, M_H is in kg, M_e is in kg and q_e is in C.

In the section 2.2.6, the mass flow rate equations derived in this section will be used to derive diffusivity constant for protons in PEM.

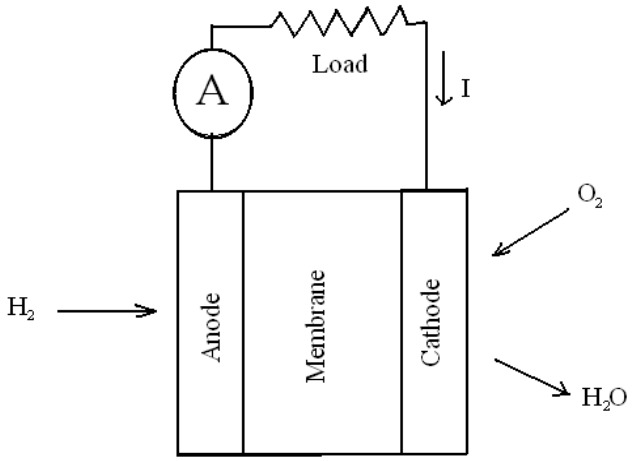

Figure 2.6: PEM fuel cell with ammeter connected.

2.2.5 Mass Flow Rate from Mass Conservation vs. Mass Flow Rate from Proton Diffusivity/Mobility

An alternative method of finding the mass flow rate of protons through the membrane is by use of proton diffusivity constant and mobility terms. In a PEM used in fuel cell, the protons transport driving forces are both due to concentration and electric potential gradients. This can be mathematically expressed as [8]

$$\dot{m}_{H^+} = D_{H^+} \frac{\left(Y_{H^+}(L) + Y_{H^+}(0)\right)}{(L-0)} + \frac{t_{H^+} I}{F} \tag{12}$$

where D_{H^+} is diffusion coefficient of proton in membrane's water content, $Y_{H+}(x)$ is the mass fraction of protons at location x in the membrane, x = L is the thickness of membrane, t_{H+} is the transport number of protons given by $t_{H^+} = \frac{u}{u+v}$ where u is the velocity of proton in an

externally applied field strength of E and v is the velocity of electron in an externally applied field strength of E. u and v are the mobility terms. I and F are current and faradays constant respectively.

It can be seen in eqn. 12 that the alternative method of finding the mass flow rate of proton involves knowing the mass fraction gradient and mobility terms. In a manner similar to other thermodynamic constants the diffusivity constant is used to cover up for the complex mechanism of transport in the membrane. Therefore, eqn. 12 depends on the accuracy of the methods used to find the diffusivity constant, mass fraction (or concentration) gradient and mobility terms. The most commonly applied diffusivity constant was found by Yeo [3] and their experimental measurement involved a fuel cell setup that is different from the typical setup of a PEM fuel cell. No information on the concentration gradient was found; however, Yeo and others [3] assumed a linear gradient with zero concentration at the cathode-membrane interface and saturated concentration of protons at the anode-membrane interface. The mobility terms are not readily available for PEM. Usually the effects of the electric field potential driving forces are absorbed into the diffusivity, so eqn. 12 reduces to Fick's law [10]. Another alternative is to use statistical mechanics and/or nanotransport methods to find the mass flow of protons by considering all particles involved with no continuum assumption. However, the new equation (eqn. 9) for mass flow of protons provides a more direct and simplified method of finding proton mass flow rate through PEM applied in fuel cells. All the nano effect in the membrane shows up in the current used in the new equation.

2.2.6 Diffusivity of Protons through PEM

In order to find the diffusivity of protons through PEM, it was assumed that the diffusivity constant contains the effects of all the driving forces for the protons motion, and the saturated concentration of protons in the membrane water was assumed to be equal to the

saturated concentration of hydrogen in water. The late assumption was made because there is no available information on the dissolution of protons in water as a function of temperature and/or pressure. However, hydrogen is closest in property to protons. Due to the assumptions that this section is based on, the diffusivity constant found in this section was mainly used for comparison with existing models. The new diffusivity constant is also a second option to finding mass flow of protons through PEM.

Consider Fick's law for 1-D case in a membrane, mass flux of protons is

$$\dot{m}_{H^+}{}'' = -\rho D_{H^+} \frac{dY_{H^+}}{dx} \tag{13}$$

where ρ is the density of aqueous mixture (protons + water), Y_H is the mass fraction of protons, and x is the distance across the membrane as shown in Fig. 2.7.

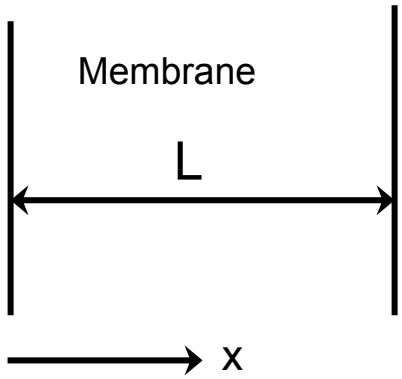

Figure 2.7: Thickness of membrane and x-axis

A linear variation of Y with x was assumed. The boundary conditions at the membrane ends are

$$Y_{H^+}(x=0) = Y_0 \tag{14}$$

$$Y_{H^+}(x=L) = 0 \tag{15}$$

The linear gradient assumption was used, because there are two known conditions: the proton saturated anode side and the proton deficient cathode side due to proton consumption. With two

boundary conditions, a straight line is the best fit, though other authors [3, 8] who used the same assumption gave no explanation. Substituting eqn. 14, 15 into eqn. 13 gives

$$\frac{\dot{m}_{H^+}}{A} = \rho D_{H^+} \frac{Y_0}{L} \tag{16}$$

Substituting eqn. 9 into eqn. 16 gives

$$D_{H^+} = \frac{I \cdot M_{H^+} \cdot L}{A \rho Y_0 q_e} \tag{17}$$

Let current density, $i = {}^{I}\!/_{A}$, then eqn. 17 becomes

$$D_{H^+} = \frac{i \cdot M_{H^+} \cdot L}{\rho Y_0 q_e} \tag{18}$$

where i is measurable. L is measurable, but it is usually readily available from membrane manufacturers. Table 2.2 shows L for some common nafion membranes. ρ and Y_o are the unknown variables left for eqn. 18. Y_o is the mass fraction of protons, when water in membrane is saturated with hydrogen protons. Therefore, Henry's law, which relates molar concentration to pressure and temperature, gives the value of Y_o. Molar concentration, $c_{j,}$ is defined as

Table 2.2: Typical thicknesses of nafion membrane [3, 12, and 13]

Membrane type	Typical L (μm)
N-112	51.00
NE-1135	89.00
N-115	127.00
N-117	183.00
NE-1110	254.00
N-120	250.00
NRE-211	25.40
NRE-212	50.80

$$c_j = \frac{\text{Number of moles of j}}{\text{Volume of mixture}} \tag{19}$$

Definition of mass fraction

$$Y_j = \frac{\text{mass of specie j}}{\text{total mass of mixture}}$$

$$Y_j = \frac{\text{Number of moles of j}}{\text{Volume of mixture}} \cdot \frac{\text{Molar mass of j}}{\text{density of mixture}} \tag{20}$$

combining eqns. 19 and 20 gives

$$Y_j = \mathrm{c_j} \times \frac{\text{Molar mass of j}}{\rho} \tag{21}$$

Eqn. 21 in terms of Y_o is

$$Y_0 \rho = c_0 \times \text{Molar Mass of } \mathrm{H_2} \tag{22}$$

According to Henry's law,

$$c_0\big|_{H_2} = K_{Henry} \cdot P_{H_2(g)} \tag{23}$$

where K_{Henry} is Henry's constant and P_{H2} is the pressure of hydrogen gas on the anode side of the fuel cell. Eqn. 23 into eqn. 22 yields

$$Y_0 \rho = K_{Henry} \cdot P_{H_2(g)} \times \text{Molar Mass of } \mathrm{H_2} \tag{24}$$

Values of K_{Henry} can be found in References 14, 15, and 16. References 15 and 16 provide K_{Henry} with high degree of accuracy over a wide temperature range but in a complex equation form. Reference 14 provides K_{Henry} accurately over a small temperature range which falls within the operational temperature of PEM FCs and has a simpler equation form. Therefore, using K_{Henry} from Reference 14 in eqn. 24 gives

$$Y_0 \rho = 8.418628 \times 10^{-3} \times P_{H_2\,(g)} \times exp\left(-\frac{500}{T}\right) \tag{25}$$

where $Y_0\rho$ is in kg/m^3, P_H is in atm and T is in Kelvin. (See appendix A1 for details of K_{Henry} simplification from Reference.) Eqn. 25 into eqn. 18 gives the diffusivity equation

$$D_{H^+} = \frac{iM_{H^+}L}{8.418628\times10^{-3}\times q_e P_{H_2(g)} \exp\left(-\frac{500}{T}\right)} \tag{26}$$

where D_{H+} is in m^2/s, i is in A/m^2, M_{H+} is in kg, L is in m, q_e is in C, P_{H2} is in atm and T is in Kelvin. $M_{H+} = 1.67263 * 10^{-27}$ kg and $q_e = 1.60217733 * 10^{-19}$ C in eqn. 26 gives

$$D_{H^+} = 1.240075\times10^{-6}\times\frac{iL}{P_{H_2(g)} \exp\left(-\frac{500}{T}\right)} \tag{27}$$

To check the validity of eqn. 27, its comparison with the most widely used existing equation (eqn. 4) is provided below.

From Yeo and McBreen's paper [3], the operating conditions and properties of membrane used are as follows:

Membrane type: Nafion 120

Thickness, L: 0.025cm = 0.00025m

Operating temperature, T: 25 ^oC = 298K

Assuming typical current density, i = 300mA/cm^2 = 3000A/m^2 and assuming pressure, P_H = 1 atm, since the experimental setup diagram (see Reference 3 for diagram) shows HCl open to atmosphere.

Substituting the above data into eqn. 26, which is the new model, gives $D_{H^+}\big|_{NEW} = 4.97\times10^{-6} m^2/s$. Similarly, substituting the above data into eqn. 4, which is Yeo and McBreens model, gives $D_{H^+}\big|_{YEO} = 0.662\times10^{-10} m^2/s$.

The error in $D_{H^+}\big|_{YEO}$ may be due to the difference in Yeo's experimental setup and the typical setup of a PEM fuel cell. Typical current density value in a PEM fuel cell ranges from 0 to 12000 A/m^2, so at i = 0.037473 A/m^2, $D_{H^+}\big|_{NEW} = D_{H^+}\big|_{YEO}$.

Graphically plots of D_{H+} for PEM fuel cell loaded with a fixed load while its operational temperature is varied are given in the plots below. The plots revealed that for constant load and varying temperatures, the new diffusivity equation predicts slight decrease in diffusivity as temperature increases. The temperature was varied over the operating temperature range of a PEM fuel cell. On the other hand, the variation of diffusivity given by Yeo's equation predicts that the diffusivity slightly increases as temperature increases. The variation of diffusivity given by Yeo's equation follows a fixed curve, while the new diffusivity equation predicts a shift in the

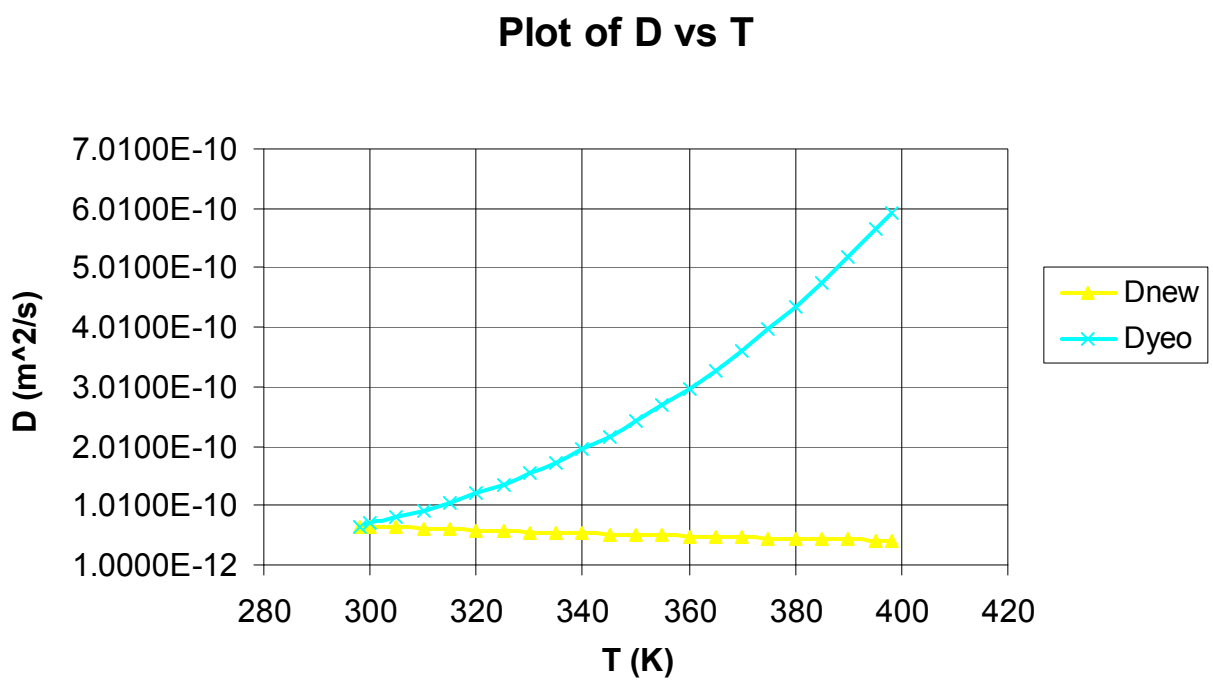

Figure 2.8: Plot of Diffusivity vs. Temperature for
$V^{\theta} = 1.0199,\ i^{\theta} = 0.03981 \Rightarrow R = V/i = 25.6192 \Omega m^2 = \text{constant}$

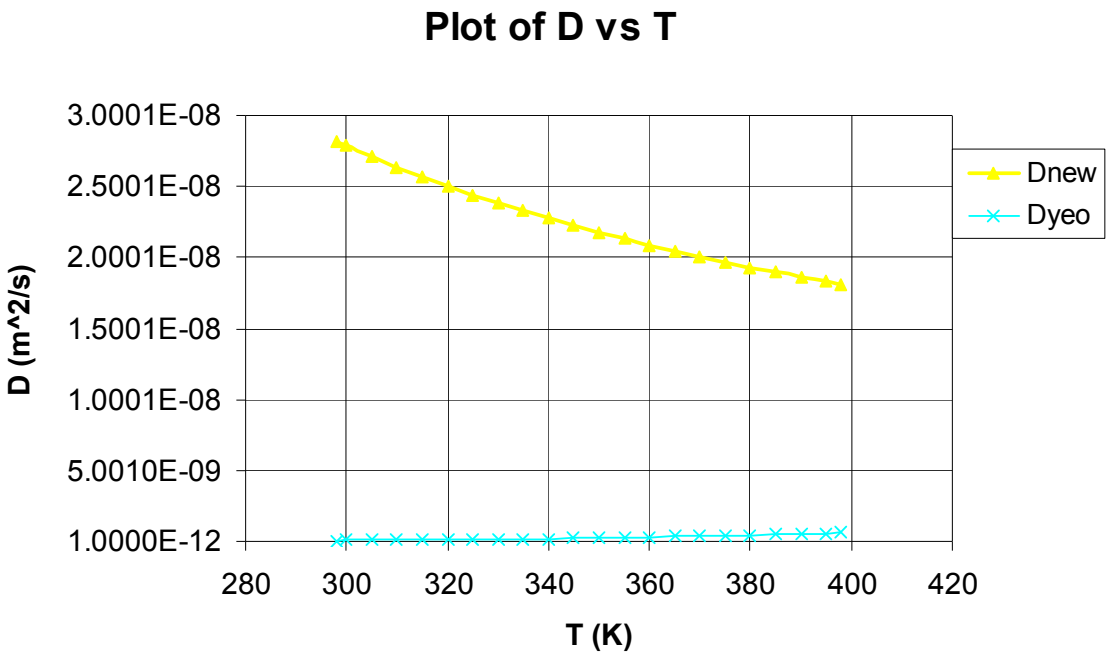

Figure 2.9: Plot of Diffusivity vs. Temperature for $V^{\theta} = 0.96, \mathrm{i}^{\theta} = 17 \Rightarrow R = V/i = 0.05647 \Omega\mathrm{m}^2 = \text{constant}$

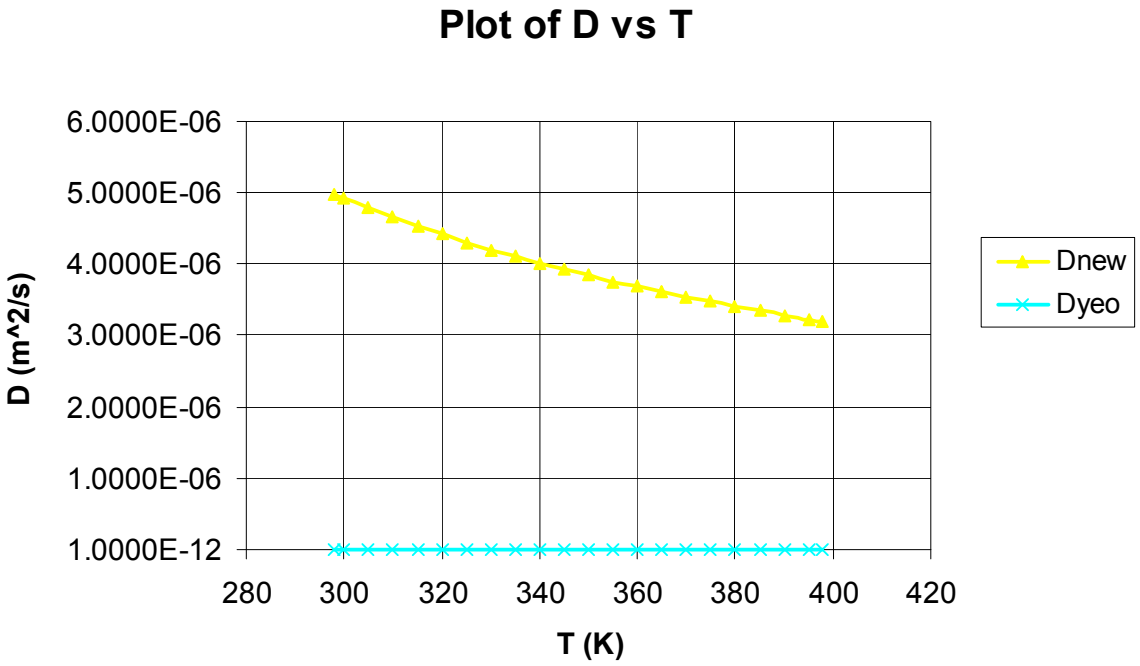

Figure 2.10 Plot of Diffusivity vs. Temperature for $V^{\theta} = 0.7, \mathrm{i}^{\theta} = 3000 \Rightarrow R = V/i = 2.333 \times 10^{-4}\ \Omega\mathrm{m}^2 = \text{constant}$

curve in an increasing direction as the load decreases. (See Figs. 2.8, 2.9 & 2.10.) It can be inferred that Yeo's eqn. is valid for high cell voltages, say $V \geq 1$ Volt. (See appendix A.2 and A.3 for details used to obtain plot.) A 3-d plot of the new diffusivity equation was generated and included in the appendix (See appendix Figs. A.1-A.3). The 3-D plot provides the same information as Figs. 2.8-2.10 in a different perspective.

2.2.7 Summary of the Derivation of Protons Mass Flow Rate and Diffusivity Equation

The mass flow rate of hydrogen through a membrane in a PEM fuel cell has been determined as a function of current. The model for the diffusivity of protons through a PEM was also developed as a function of current, pressure, and temperature. The new models have been developed in relation to the electrochemical process in a fuel cell. The development of the models was based on the application of the law of mass conservation. The new model is current and temperature dependent, while the model developed previously by Yeo and McBreen is only temperature dependent. However, the two models equalizes at a certain value of current on the load curve of a simple PEM fuel cell. The variation of diffusivity provided by the new equation can be explained by the fact that the voltage is directly proportional to the free energy change ($V \alpha \Delta G$) and the free energy change of a PEM fuel cell reaction decreases with increase in temperature. (A brief derivation of V as a function of T using best curve fits for $\Delta H(T)$ and $\Delta S(T)$ is given in appendix A.2) In addition, the solubility of hydrogen protons in water increases with increase in temperatures. The increase in dissolution of hydrogen protons results in an increase in mass flow rate which suppresses the effect of the slight decrease in diffusivity. The above mentioned factors contribute to the decrease in diffusivity as temperature increases. However, for temperatures beyond the operational temperature range of a PEM fuel cell, the membrane will fail leading to formation of pores and the free flow of hydrogen across failed membrane. (Additional, as explained earlier, the membranes are made from polymeric material,

which is not resistant to high temperature. [13]) Usually, D_H is used to find mass flow rate (as shown in eqn. 12), and eqn. 9 provides $\dot{m}_H$. Therefore, if mass flow rate is the main interest, then eqns. 6 and 9 can be directly used and the complex derivation of D_H can be optionally skipped. The new model will be used in this project. The next section will involve simulating a PEM fuel cell with a free flow channel and studying the cathode flow region to understand why a new design will be later developed.

The next section is focused on work done to improve the performance of fuel cells flow channel.

2.3 Investigation of Flow Field Design for PEM Fuel Cells

2.3.1 Literature Review

The design of special gas flow channels for high absorption and easy removal of wastewater is a major research area of interest for fuel cell researchers. This section gives a literature review on current research works in this area.

Recently, Nguyen and coworkers [17] used CFD to provide information about temperature distribution and potential distribution in a PEM fuel cell with serpentine gas flow channels. Their work was more of computational development than problem solving. Williams and coworkers [18] investigated the influence of convection through gas-diffusion layers on limiting current in PEM fuel cells with serpentine flow channels. They conducted experiments at different operating conditions to evaluate, the influence of cell temperature, oxygen mole fraction, and relative humidity on the limiting current. The gaseous convection was varied between flow rates of 50 and 1000 cm^3/min, and it was found that convection has significant effect on the limiting current. It was also found that increase in flow rate of oxidizer results in increase of limiting current. Van Zee and coworkers [19] investigated the effect of changing the flow field configuration on the performance of a fuel cell. They studied two configurations of the serpentine flow channels: A

single pass flow field and a double pass flow field. They concluded that the double pass flow field gives a more uniform current distribution and better water removal. The work of Cha and coworkers [20] showed that making the channels cross-section smaller improves the performance of fuel cells, but it brews up problem with water removal. Karvonen and coworkers [21] investigated the behavior of gas flows in a parallel channel. They did not consider the serpentine flow channel. However, their work is of interest because they concentrated their work on studying the effects of the channel. Maharudrayya and coworkers [22] used numerical simulations to investigate the pressure drop along the channels of a serpentine flow channel. The major disadvantage of serpentine flow channel is its high pressure drop across the flow field compared to the parallel flow channel. Their investigation showed the pressure drop is greatest at the sharp corners of the serpentine flow field, so they modified serpentine design by changing the 90^0 turns to radial bends in order to reduce the pressure drop. Shimpalee and coworkers' [19] work involved the experimental study of the effect of a serpentine channel path length on the performance of a fuel cell. Their work is of interest, since they found that the channel with smaller path lengths performs better than channel with longer channel path lengths. Progress has been made in flow fields design, but fuel cells still lack behind their expected performance. Therefore, in this project, an investigation will be done to better understand fuel cells flow field and come up with a new improved design. The effects of flow field design to the performance of fuel cells are addressed in the next section.

2.3.2 Effects of Gas Flow Field Design

A single fuel cell generates about 1 volt, so to power loads that operates at high voltages, a number of single cells are usually stacked together (see Fig. 2.11 below). The stack of fuel cells is analogous to a battery of voltaic cells. The stack is usually compact to avoid having a bulky fuel cell, so the gas channels are usually small. The gas is usually delivered as shown in Fig.

2.11. The control volume selected in the cathode channel (yellow rectangle in Fig. 2.11) will be used in the next sub-section to study the performance of the channel while the fuel cell is in operation. A fuel cell in operation will be simulated, and the selected cathode region will be studied in order to find out why there is need for designing special channels.

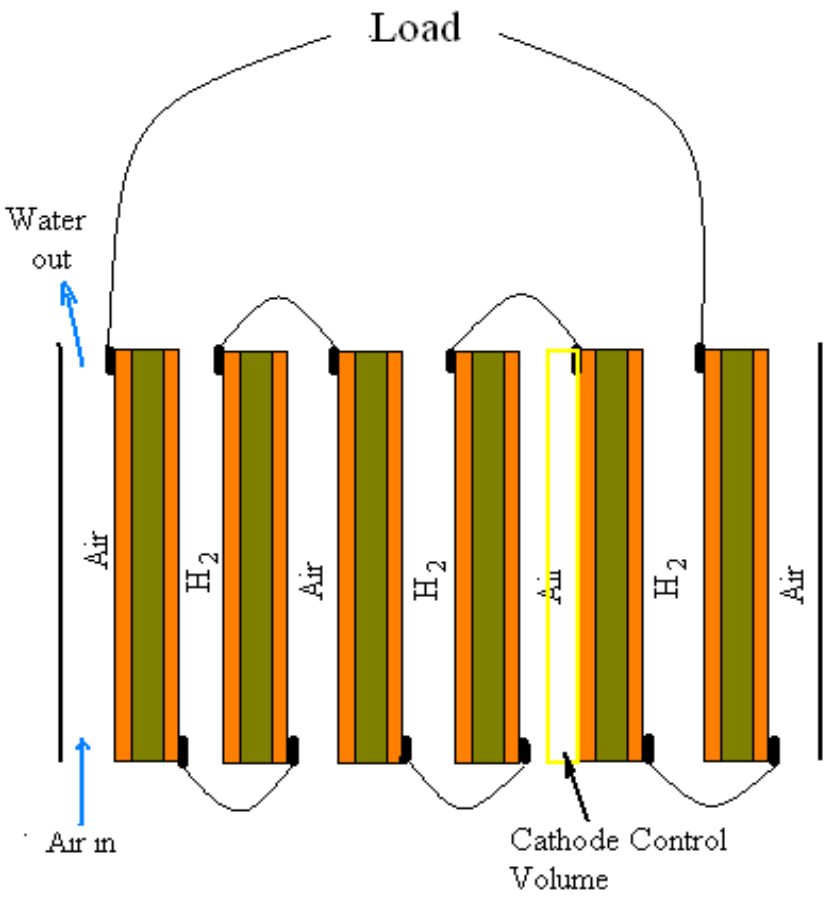

Figure 2.11: A typical fuel cell stack diagram.

2.3.3 Simulation of Free Flow Channel

A model of the control volume selected in Fig. 2.12 and a structured grid was generated for the region (Fig. 2.13), since the shape of the region is not complex. The simulation was done at Re = 800 with respect to the flow rate of the oxygen. The reaction rate and generation of water vapor were simulated assuming a typical current density of 3500 A/m^2 and using the new transport model developed in section 2.2. (eqns. 6, 9)

2.3.4 Simulation Results and Discussion

A careful inspection of the simulated cathode flow region in terms of the volume fraction of oxygen revealed that as water vapor forms at the surface of the cathode and close to the cathode, a boundary layer of water vapor develops and subsequent oxygen tends to flow over the

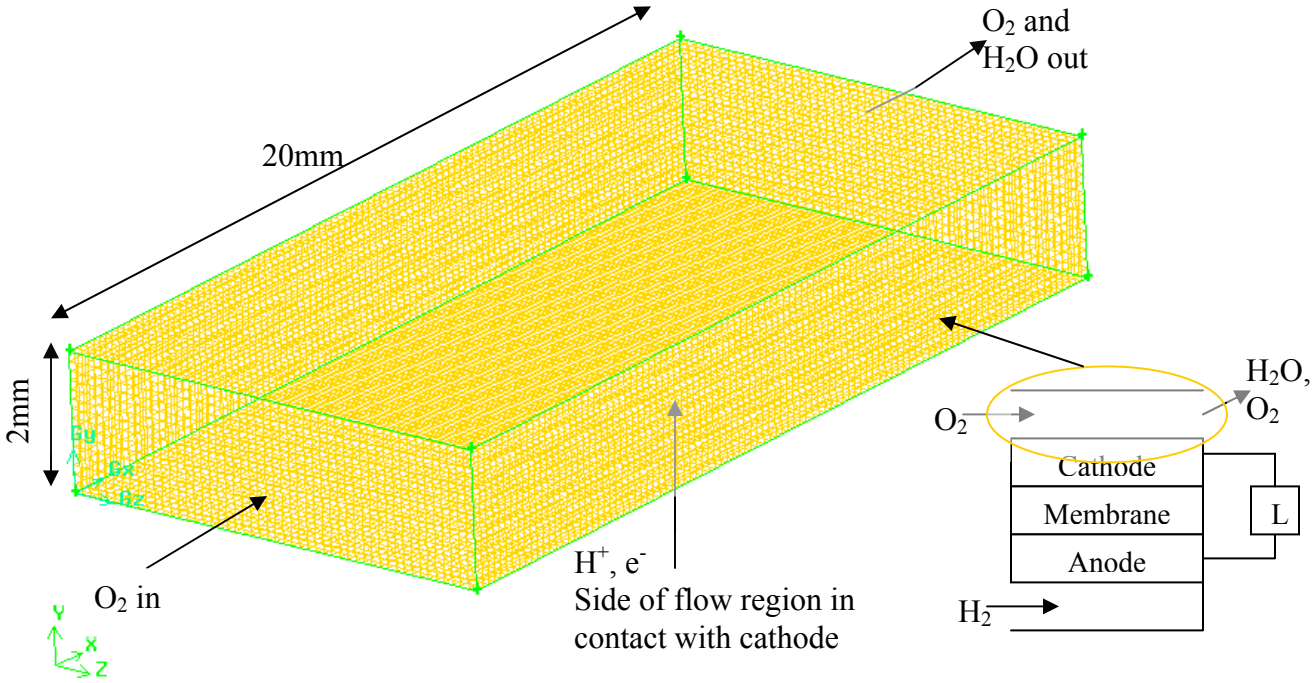

Figure 2.12: Model of cathode side flow region

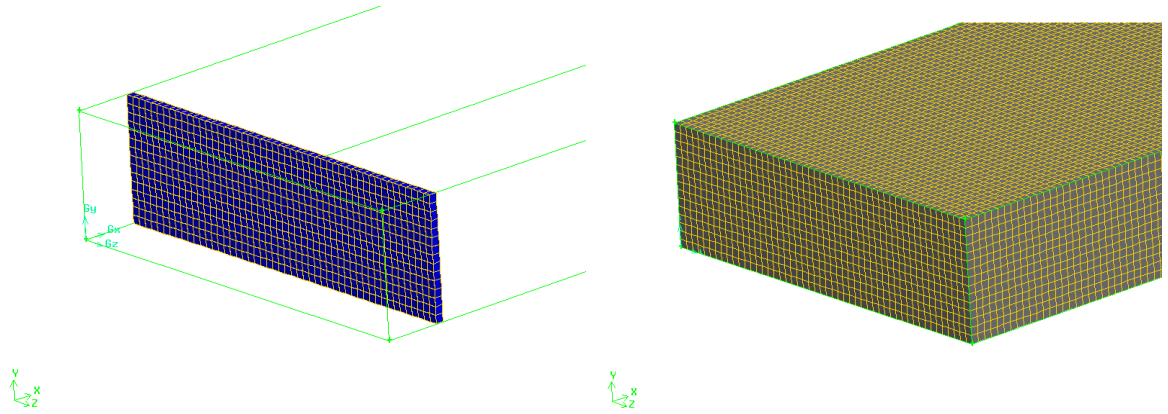

Figure 2.13: Structured grid generated for cathode flow region

water vapor boundary layer (see Fig. 2.14). A view of the bottom of the cathode flow region in contact with the cathode electrode shows higher concentrations of oxygen at the inlet and lower concentration of oxygen towards the outlet. The developed boundary layer over the cathode

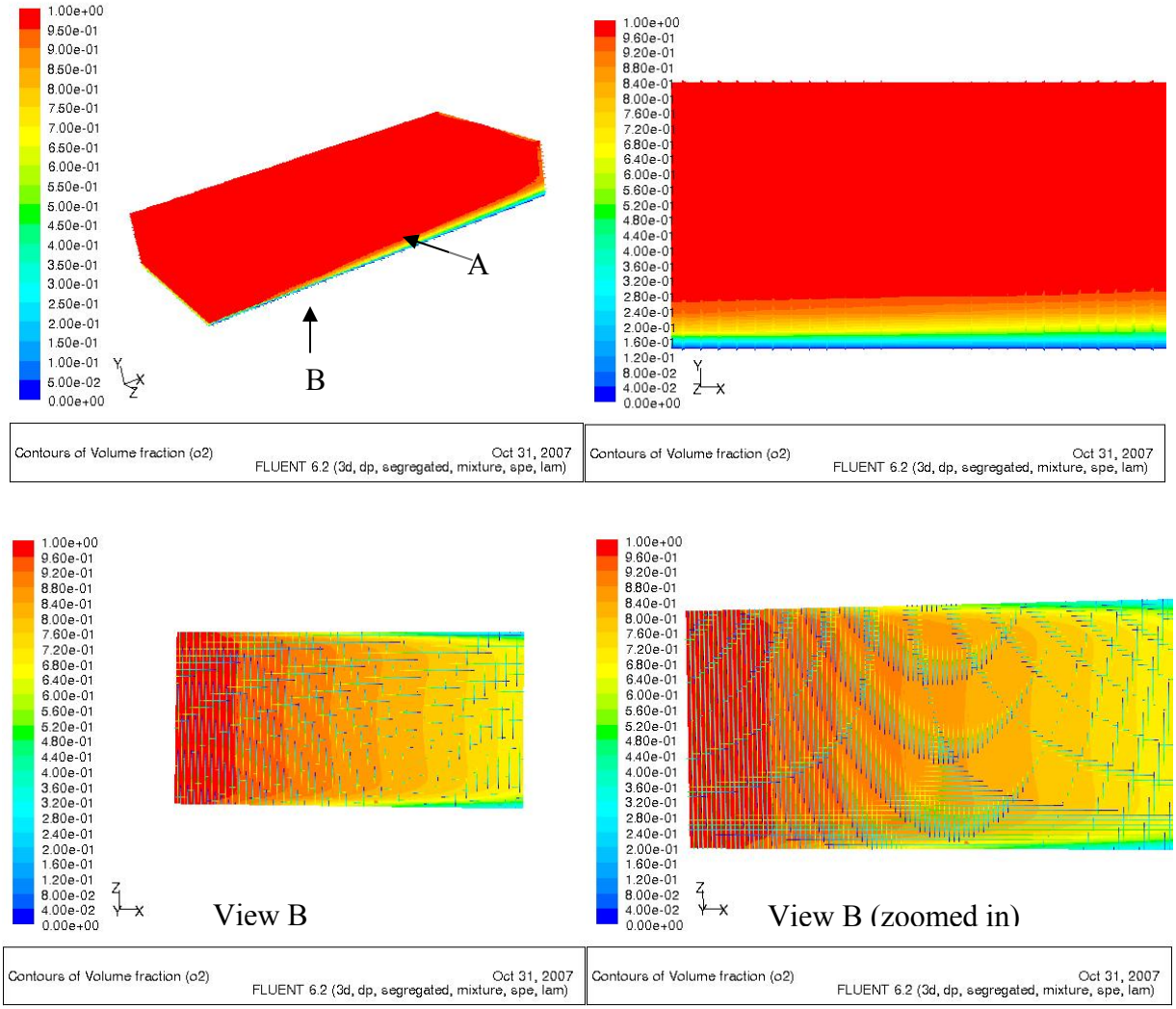

Figure 2.14: Cathode flow region simulation for Re = 800. Showing contours of O_2 volume fraction.

surface area is undesirable, since fuel cell operation requires that the oxygen in the cathode flow region gets in contact with or sufficiently close to the electrode surface where it reacts with protons and electrons to produce water vapor. This observed phenomenon creates the need for mixing in the flow region in order to ensure that there is proper mixing of oxidizer and to ensure

that the oxidizer reaches the cathode. This boundary layer doesn't usually occur in the anode, since the H_2 gas always get to the anode before splitting. (See fuel cell diagram Fig. 2.2: It is clear that there is only one specie on the anode side and more than one specie on the cathode side. It is also clear that oxygen needs to be supplied to the cathode and water needs to be removed from the cathode.) However, for structural stability and current collection, bipolar flow channels should be used in fuel cells. Bipolar flow channels are interchangeable which means that they can be switched between the electrodes. [5, 7, 19]

The above observations of the simulation results points to the need for specially designed flow fields. There are several types of flow field designs of which the serpentine and the parallel flow fields (Fig. 2.15) are the most widely applied. The serpentine flow field has a meandering flow path with 180^o turns in flow direction. The serpentine flow field performs best and easily flushes out liquid water. [5, 7, 19]

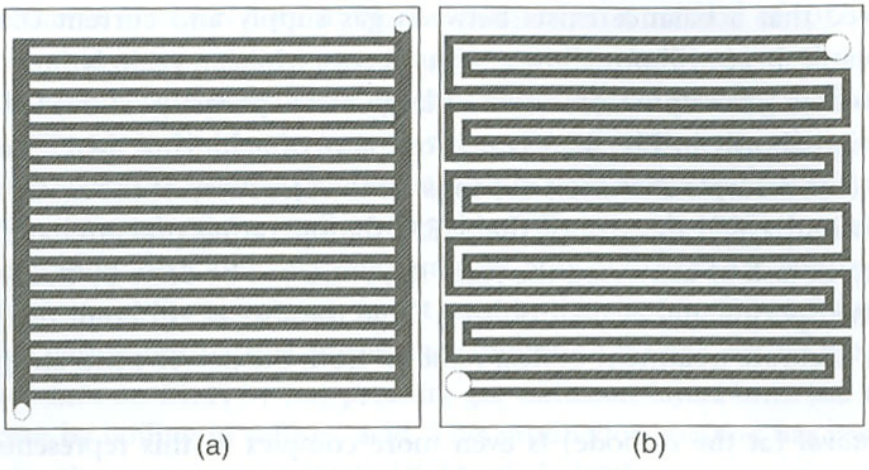

Figure 2.15: (a) Parallel flow field, (b) Serpentine flow field [18]

However, it has a high pressure drop across the flow line. The parallel flow field is second to the serpentine flow field in terms of performance. It consists of a flow field path that splits into several parallel flow paths over the electrode area. The parallel flow paths recombine at the exit.

It has the advantage of supplying fresh oxidizer to each parallel flow path and the pressure drop across the flow region is low, compared to that of the serpentine flow channel. Its major disadvantage is that when liquid water forms in some of the parallel paths, the oxidizer flow skips the waterlogged paths and flows through the free flow paths. The water logged paths or regions are consequently deprived of oxidizer supply and the overall performance of the fuel cell drops. Therefore, the parallel flow field is preferable as long as the water formed at the cathode does not condense.

The serpentine flow field is the flow field of choice for modifying its design in this project. This is because the channel causes the flow to turn creating mixing and as such oxidizer reaches the cathode.

2.3.5 Design to Enhance Mixing

The Reynolds number (Re) in fuel cells oxidizer gas flow is usually in the laminar flow regime. In laminar flow, the entrance length of a pipe flow is typically as shown in Fig. 2.16. In the inviscid length, L_i, the entrance flow properties remain approximately the same. This means that a uniform velocity flow will tend to retain its uniformity in the L_i length and similarly an unsteady flow will tend to retain its unsteadiness along L_i. Along the profile development length, the profile develops. The profile development length and the developed length are not desirable in the serpentine flow field, since the eddy flow caused by the turns will have decayed at this length. Therefore, each straight flow line of the serpentine flow channel should be about L_i, which is $L_i = 10\ D$ [23] and D is the cross-sectional hydraulic diameter.

Flow development phenomena will be demonstrated in the flow simulation in section 2.3.5 and will serve as the basis for the new design. The simulation studies using the criteria discussed in this section and aimed at finding a generalized length that ensures eddy flow and no

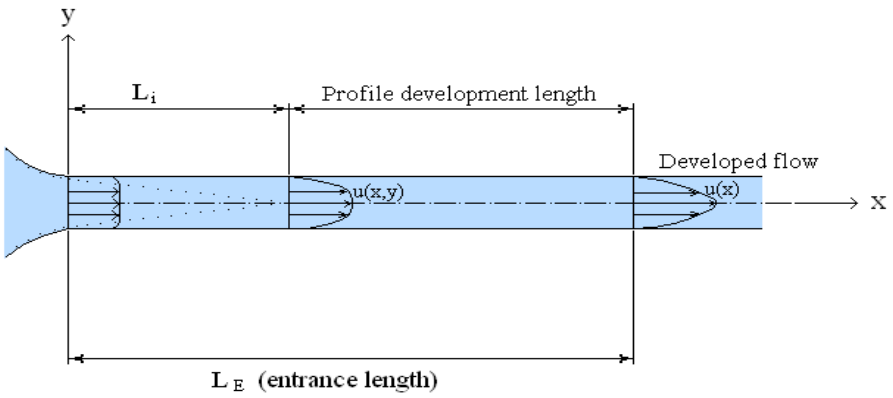

Figure 2.16: Flow development in a laminar flow through a pipe. [23]

flow development is presented in the next section.

2.3.5.1 Simulation

Serpentine flow channels with different lengths of flow line between turns were modeled as shown in Fig. 2.17. Structured grids were generated for the flow regions (see Fig. 2.18), since the flow region does not have a complex shape. Flows through the modeled serpentine flow fields were simulated for Re = 800 (Re 800 was selected because it is less than 2200 and in the laminar regime). The inlet dimensions are a = 2mm and b = 2mm, which implies that D = 2mm. The channel lengths were L = 50D, 20D and 10D. It was expected that due to profile development phenomena, eddy flows will die out over longer flow channels.

2.3.5.2 Results and Discussions

By inspection of the simulation results, it was observed that for L > 10D, the flow was mixing as it emerged from the turns. As the flow approaches the next turn at distances > 10D, the flow develops. The serpentine flow channel modeled with L = 10D had mixing flow over its whole path lengths, hence it will be best for mixing of oxidizer and water vapor so that there is a supply of oxidizer to the cathode surface. The mixing of product water vapor with oxidizer will

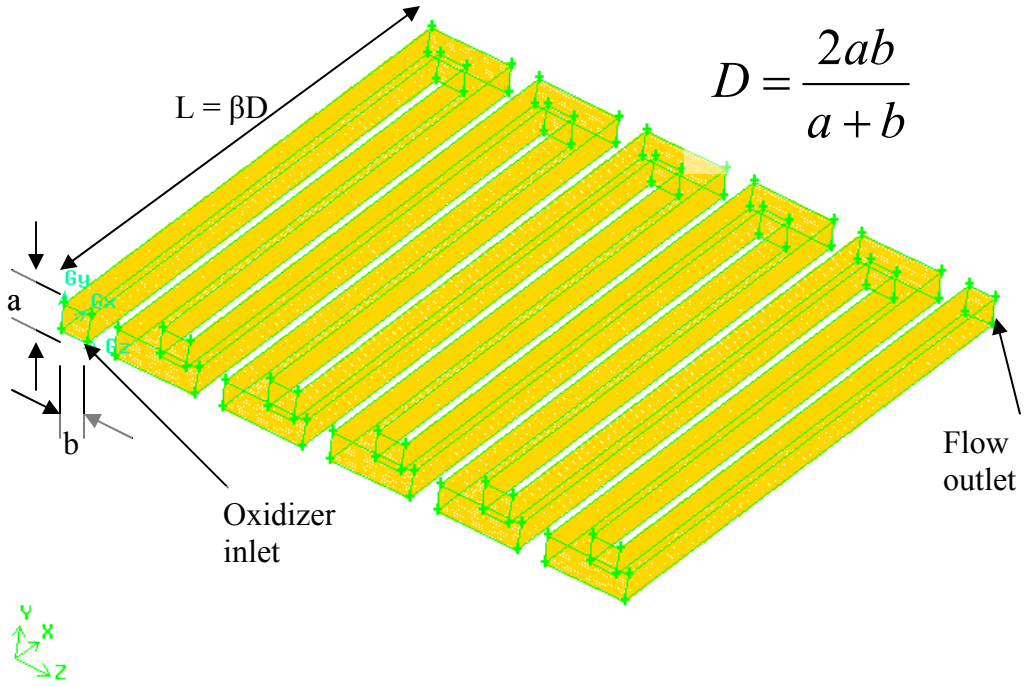

Figure 2.17: Model of serpentine flow channel

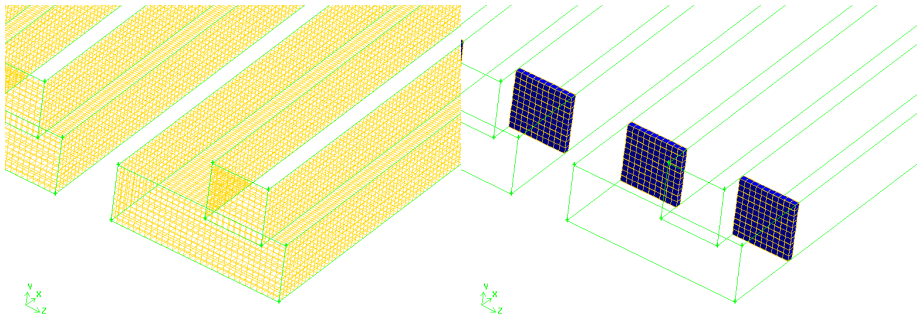

Figure 2.18: Structured grid generated for serpentine flow channel model

Reduce the condensation of water and consequently facilitate the removal of product water. Shortening the length between corners does not necessarily have to reduce the electrode area, so parallel flow field design can be combined with the short paths serpentine flow field as shown in Fig. 2.25. The final design (Fig. 2.25) has specified straight path length and is a hybrid of Parallel and Serpentine flow field designs. (See References 5, 7, and 24 for other designs.)

2.3.5.2.1 Results for L=50D

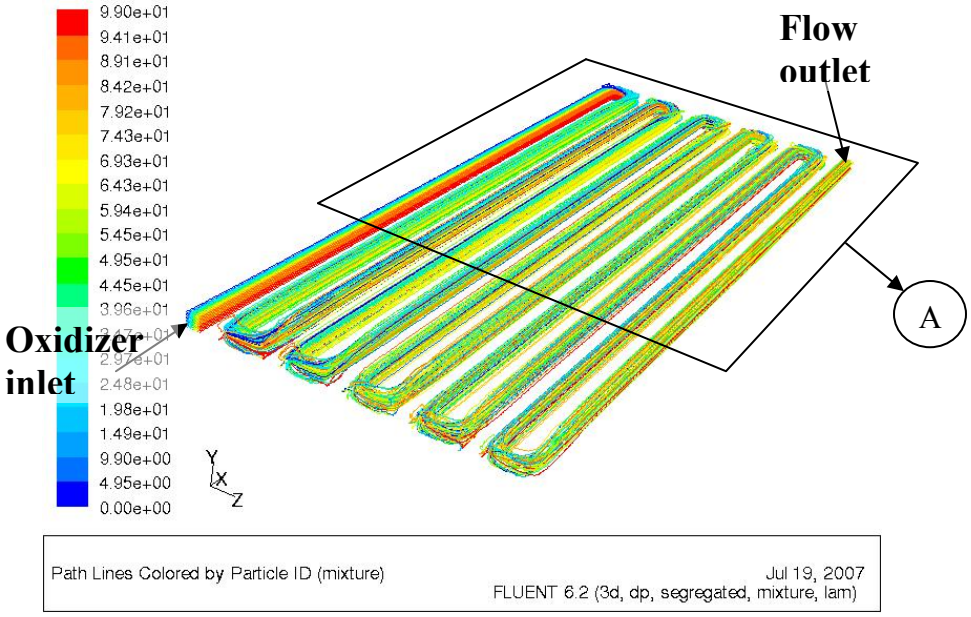

Figure 2.19: Simulation result for serpentine flow channel with L = 50D

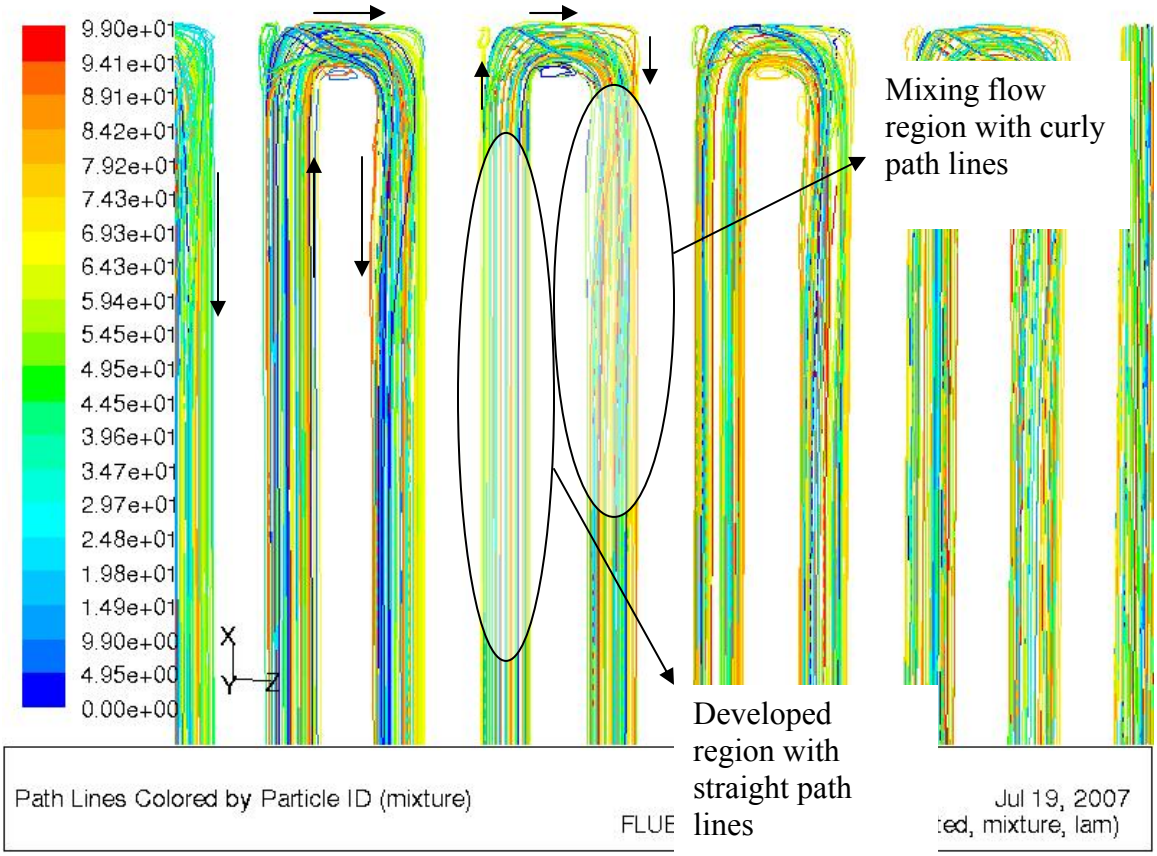

Figure 2.20: Magnification A from Fig. 2.19

2.3.5.2.2 Results for L=20D

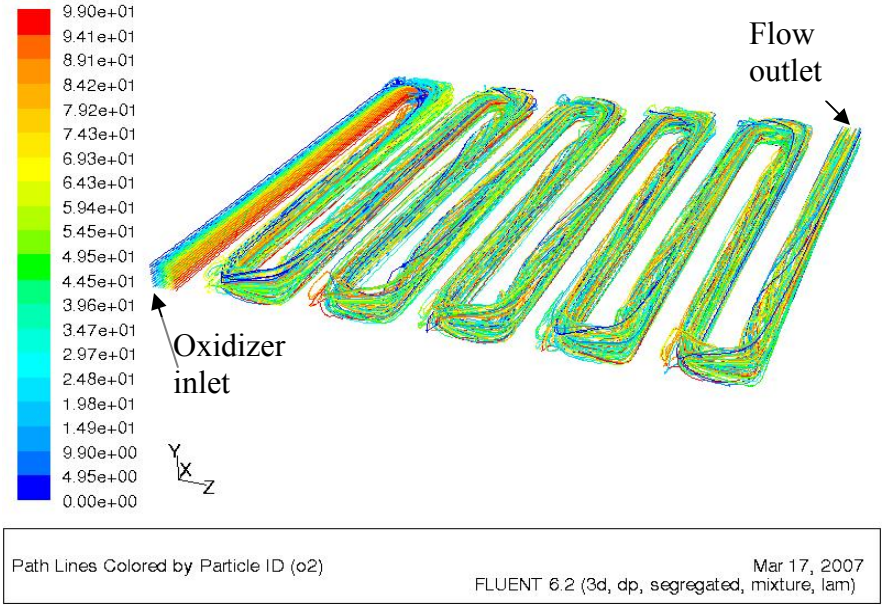

Figure 2.21: Simulation result for serpentine flow channel with L = 20D

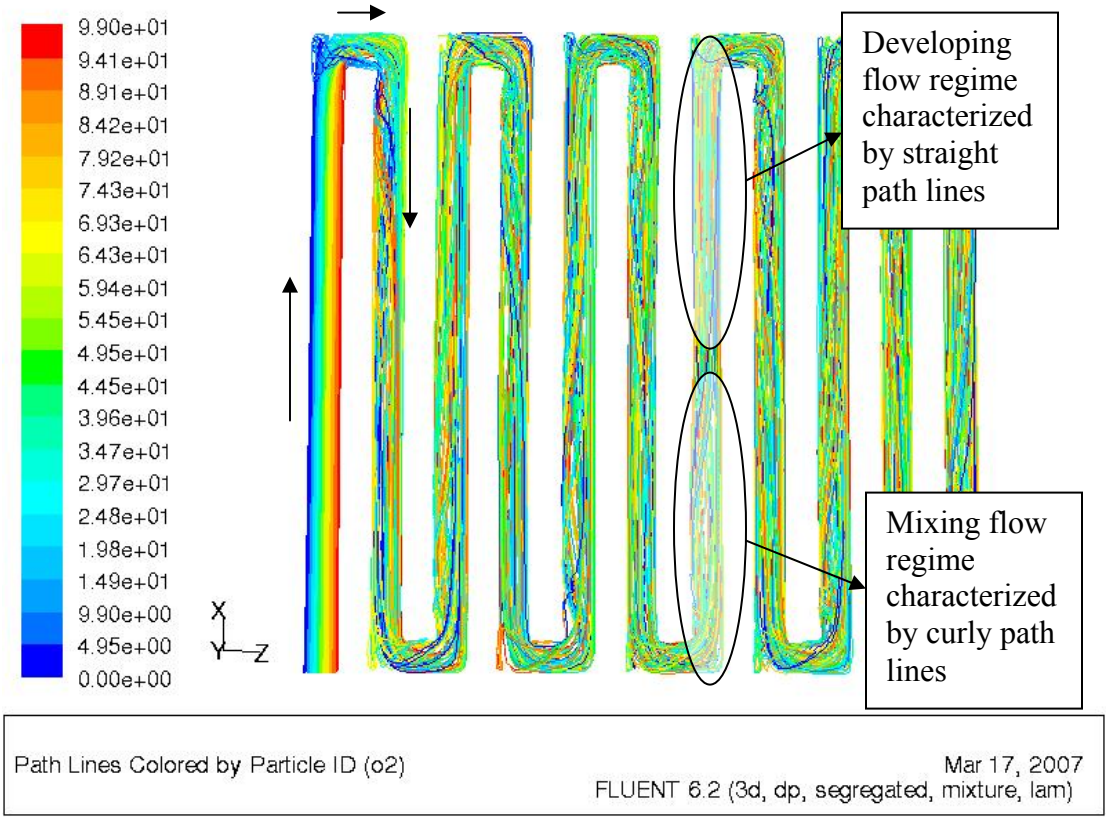

Figure 2.22: Magnified plan of Fig. 2.21

2.3.5.2.3 Results for L=10D (Desired design)

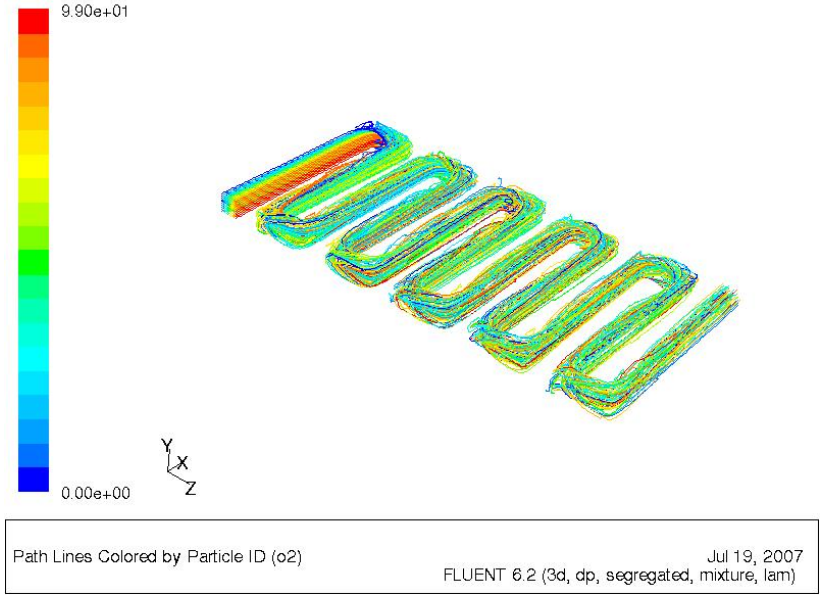

Figure 2.23: Simulation result for serpentine flow channel with L = 10D

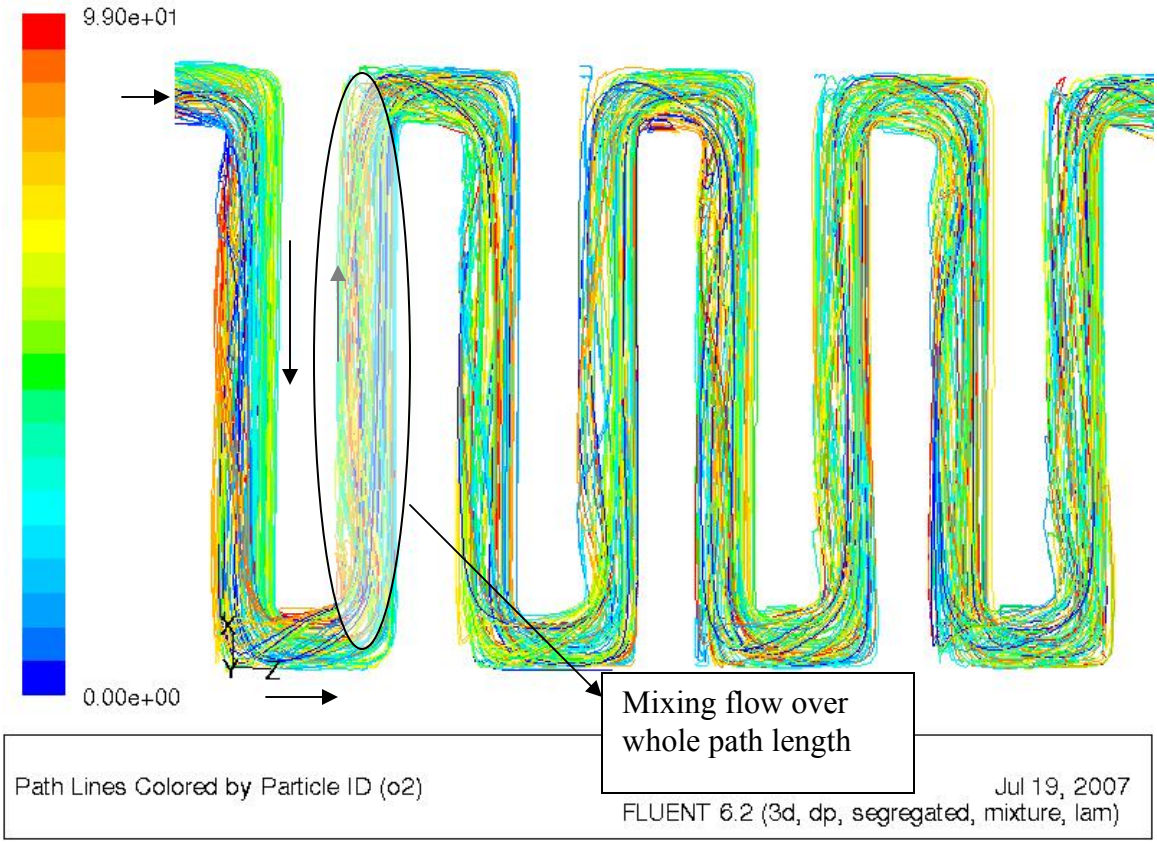

Figure 2.24: Magnified plan of Fig. 2.23

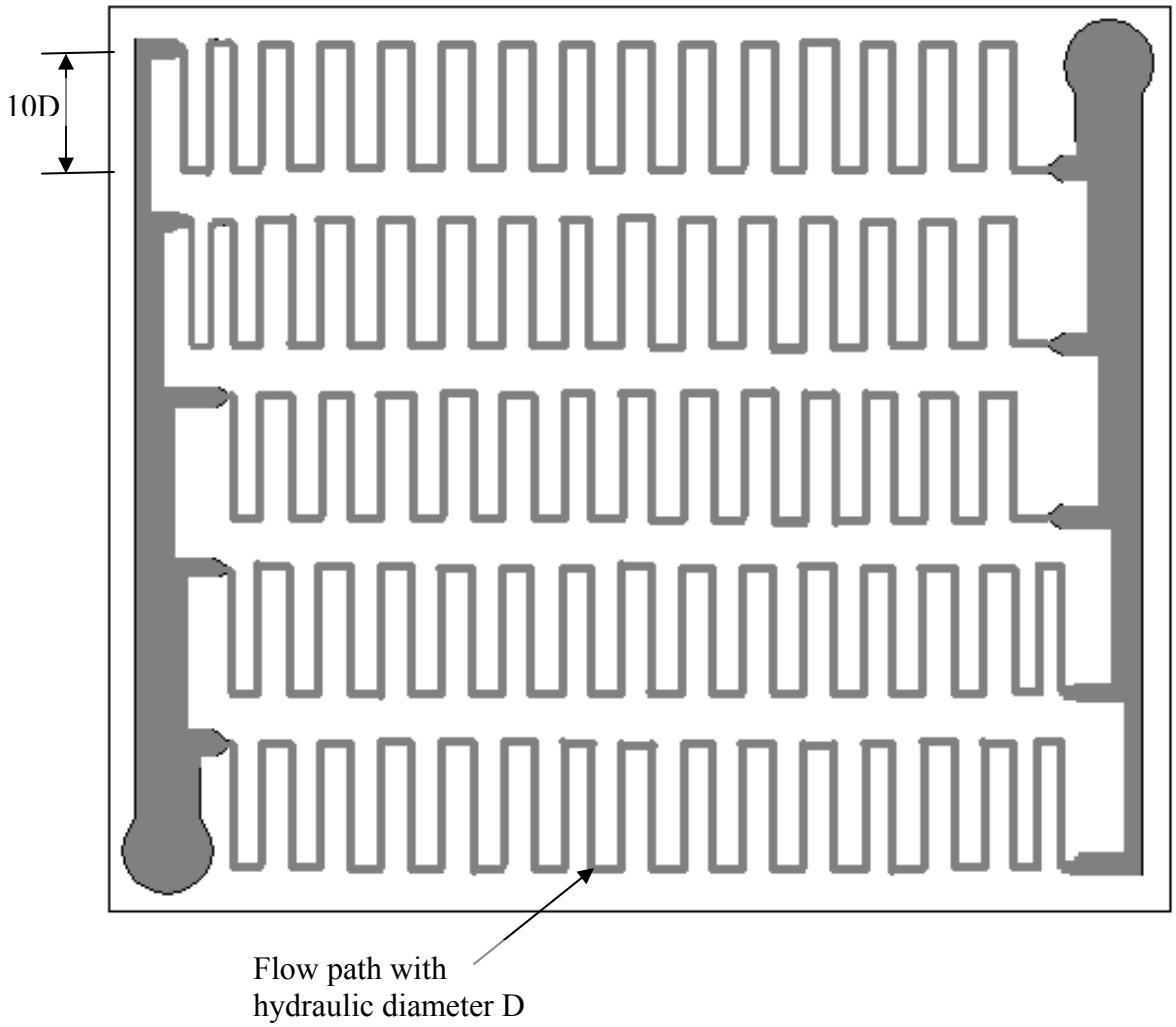

Figure 2.25: Parallel-Serpentine flow field design for large electrode areas. (Final design for best performance)

2.3.6 Flow Channel Experiments

2.3.6.1 Fabrication of Channels

The two pairs of channels were designed and fabricated from aluminum blocks. (See appendix A.4 for details of dimensions.) The first pair was designed using the conventional serpentine flow field, while the second channel was designed using the new parallel-serpentine flow field design developed in this project. Solid models and the fabricated channels are shown in Figs. 2.26 and 2.27. Both channels cover the same area for the purpose of comparison.

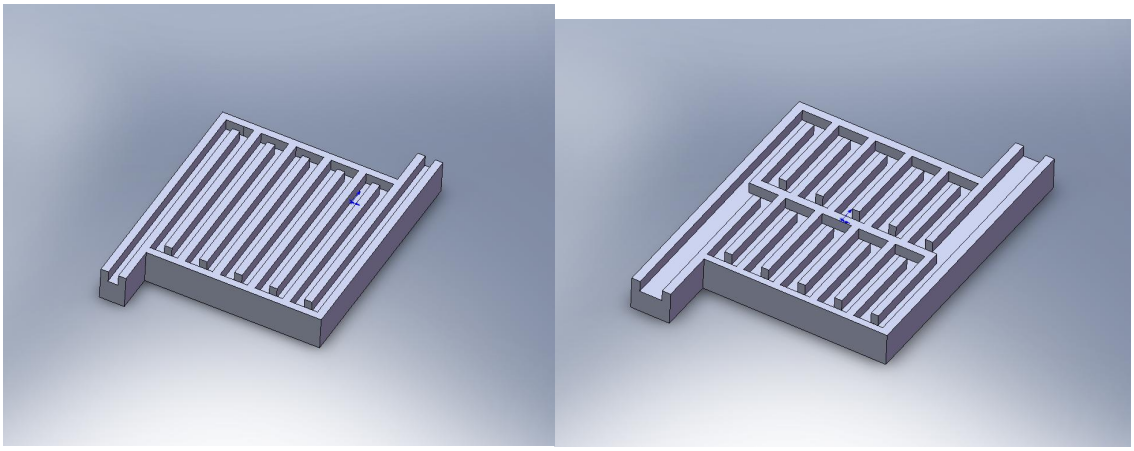

Figure 2.26: CAD models of Aluminum flow channels for experiments

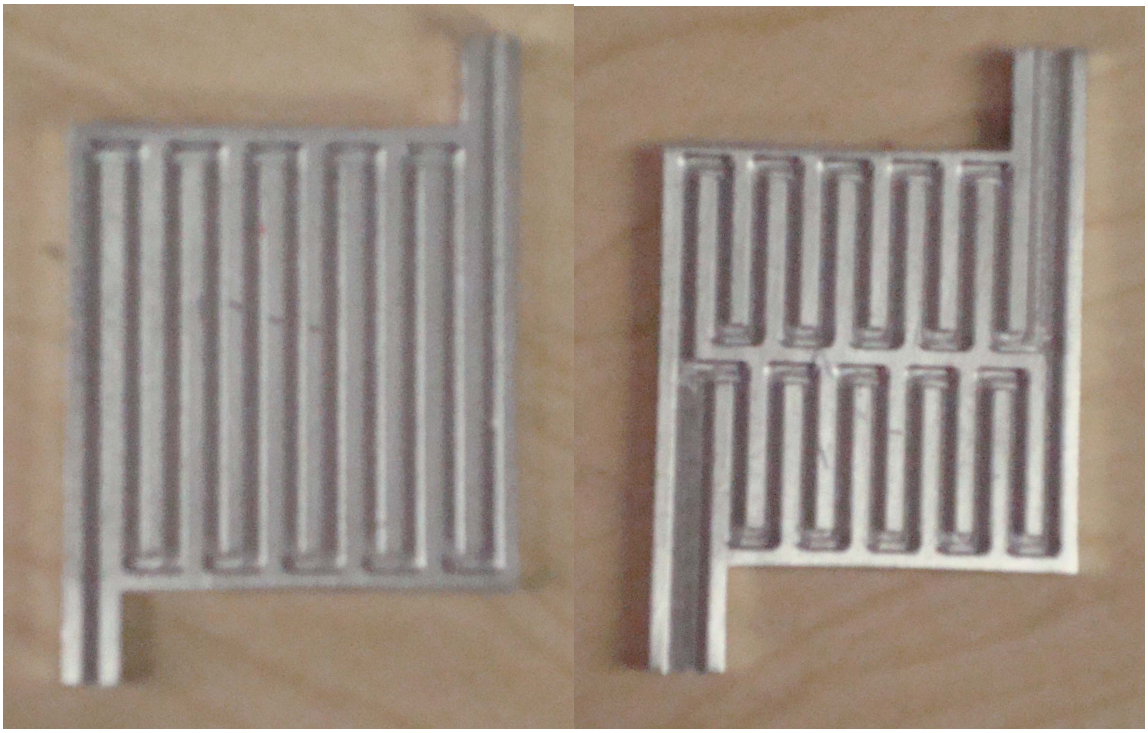

Figure 2.27: Fabricated Aluminum flow channels for experiments

2.3.6.2 Experimental Procedure

The membrane was first moistened with deionized water. Then the channels were assembled along with electrodes and membranes to form simple PEM fuel cells (See Fig. 2.28 & 2.29). The experiment was setup as shown in Fig. 2.31. The hydrogen cylinder was carefully

opened to a low pressure, and then the valve on the hydrogen flow meter was opened slowly till bubbles of hydrogen started forming in the beaker of water containing the hydrogen Teflon pipe outlet. Exactly 5 bubbles escape per minute was used for all the experiments, and at 5 bubbles/min, the reading on the flow meter was negligible. The operational pressure was 1 atm. The flow meter used for oxygen/air was calibrated, so the flow rate of oxygen/air was set to 0.35 liters/min. The same oxidizer flow rate was used for all the experiments in this section. The load cell, whose simple loading circuit is shown in appendix Fig. A.6, was used to load the fuel cells and readings were taken.

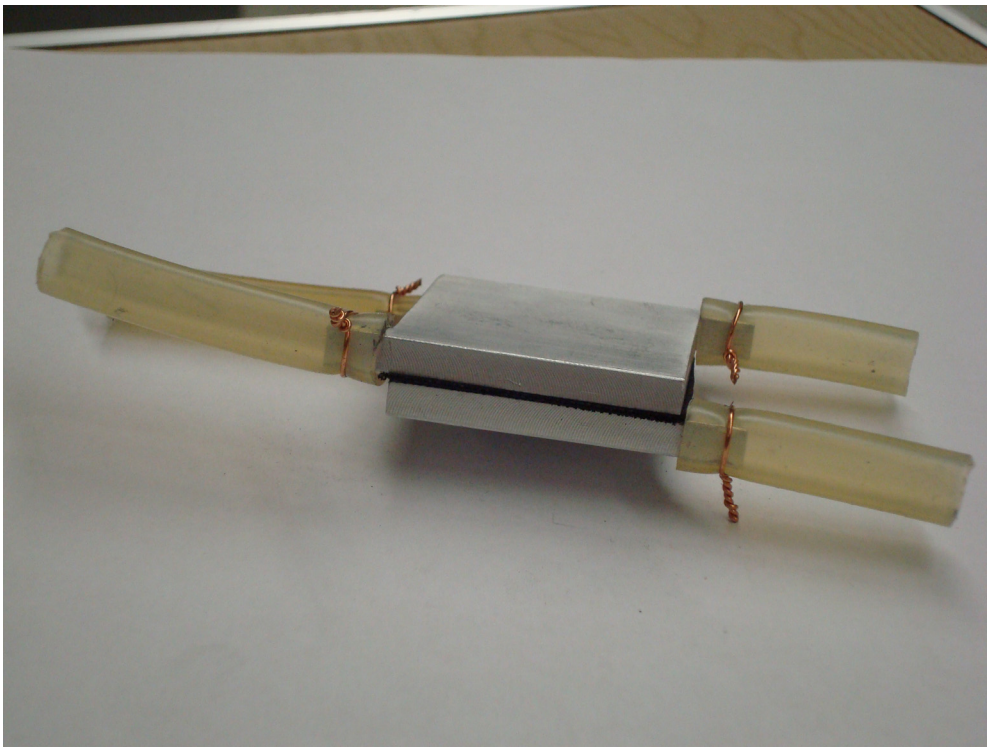

Figure 2.28: PEM FC assembled with fabricated channels

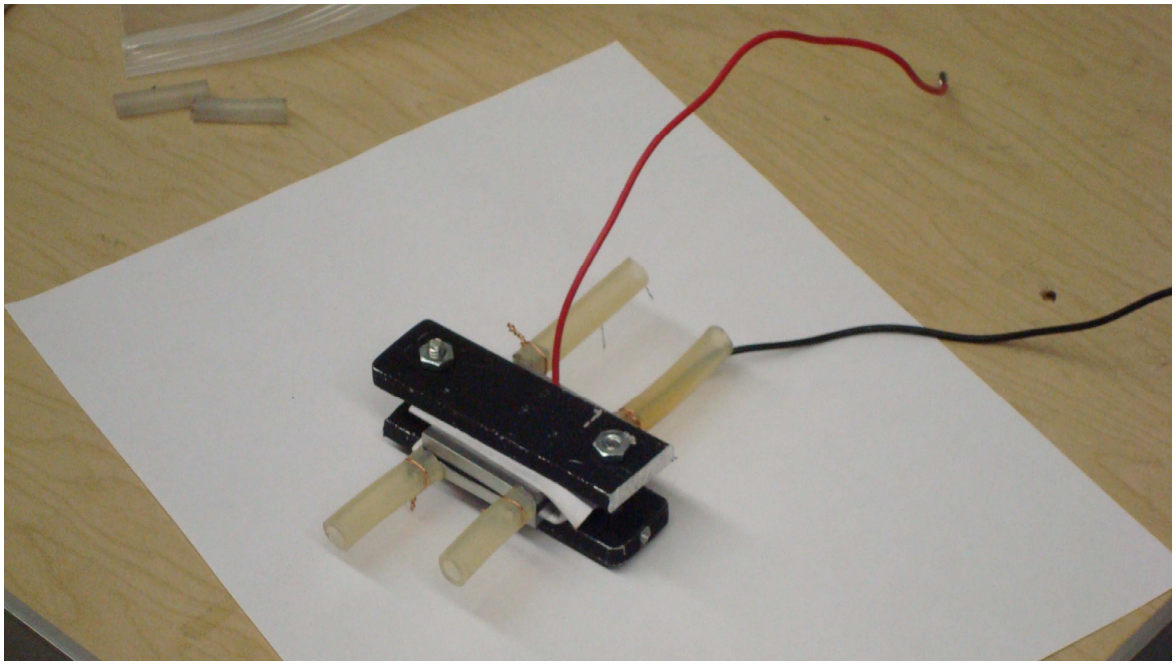

Figure 2.29: Assembled PEM FC with leads

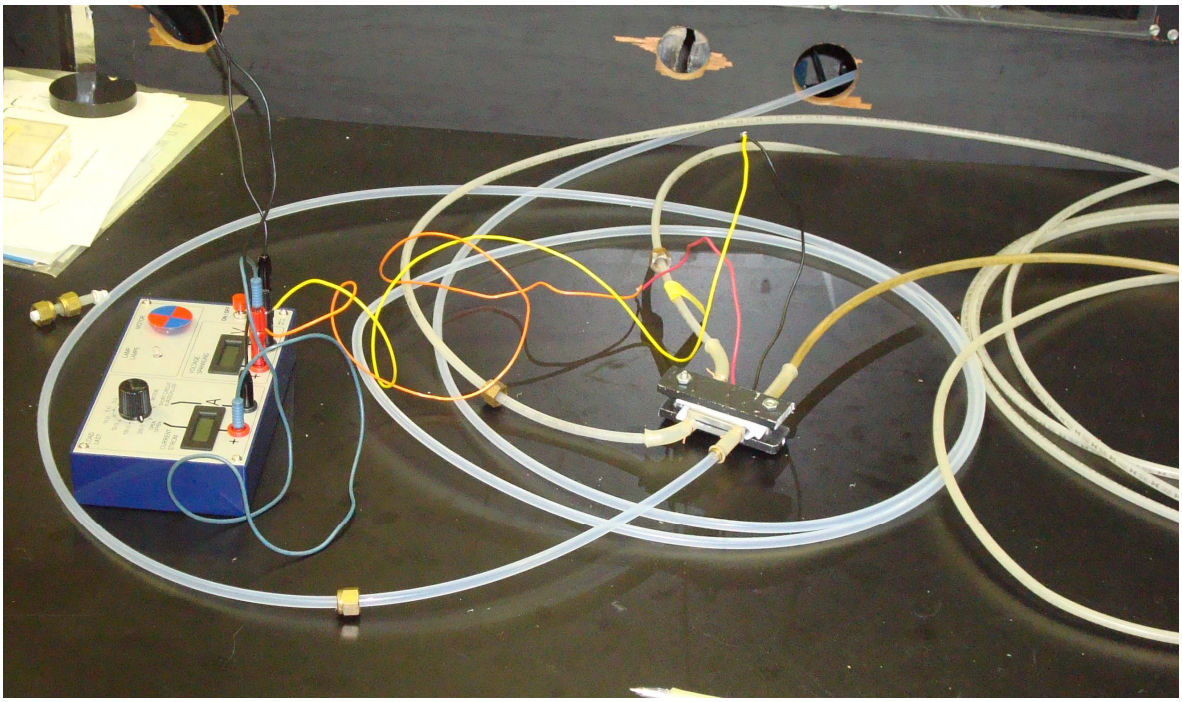

Figure 2.30: Picture of PEM FC experimental setup

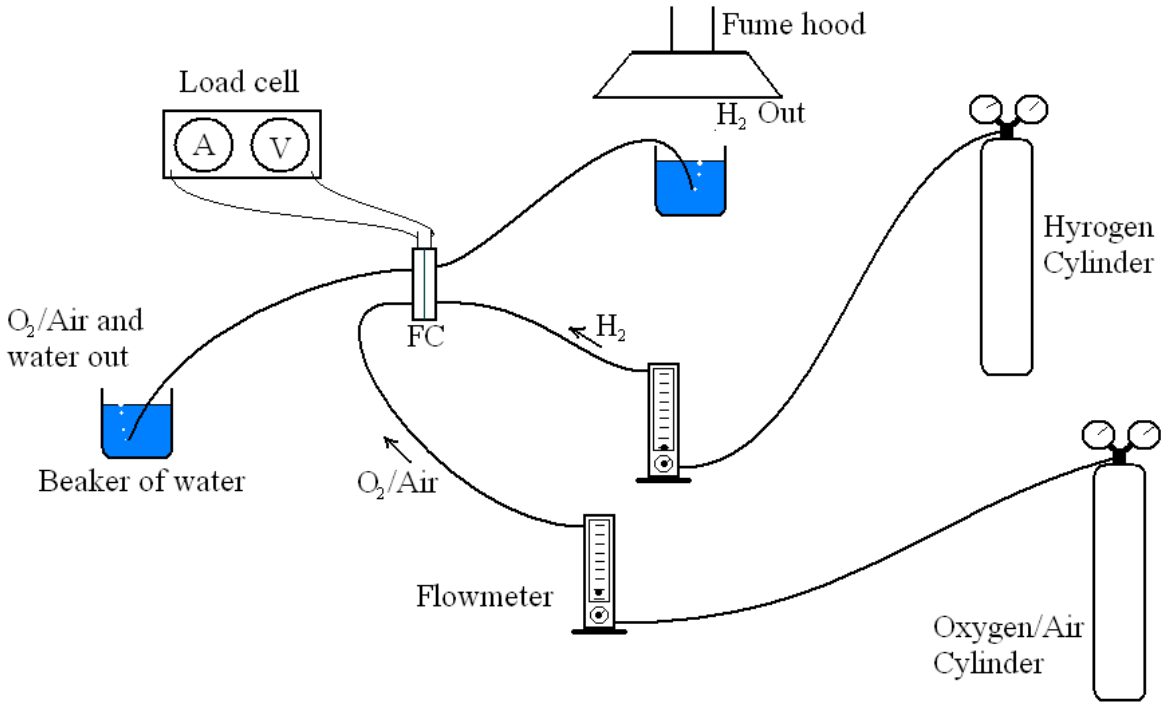

Figure 2.31: Schematic of PEM FC experimental setup

2.3.6.3 Results and Discussions

A plot of the experimental results obtained showed that the parallel-serpentine flow field design has a better performance than the conventional serpentine flow field design. (See Fig. 2.32 below.) Error analysis was done and included in the data tables in the appendix. (See appendix A.5 for data used to obtain plot.) At 0.6 volts, the area of the shaded region represents the increase in power obtained after using the new flow field design. (See Fig. 2.33) The major increase in the power capacity of the fuel cell is due to the increase in the fuel cell reaction because the new channel increases supply of oxidizer to the cathode.

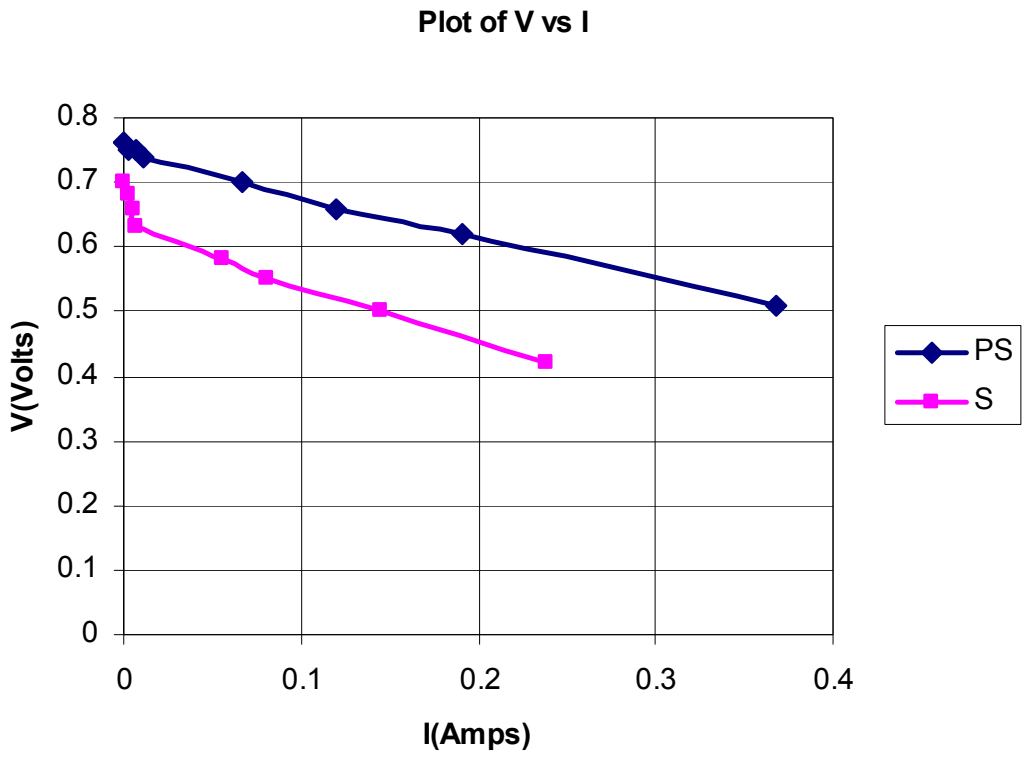

Figure 2.32: Plot of V vs. I for the flow field design experiment

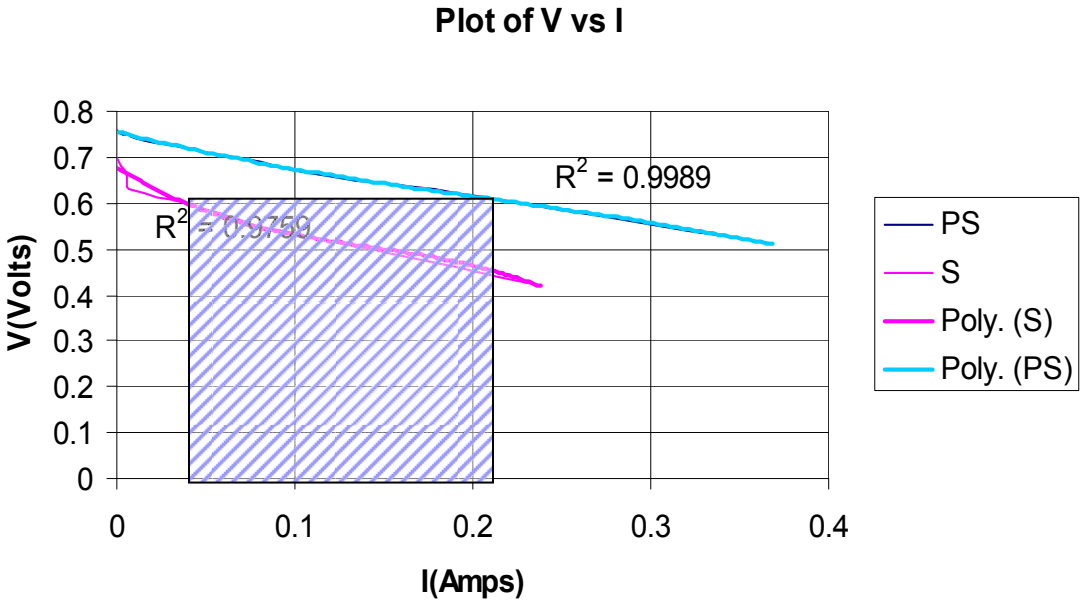

Figure 2.33: Plot of V vs. I with shaded region showing power increase.

2.4 A Study of the Effect of Electrodes Areas on the Efficiency of PEM Fuel Cells

2.4.1 Introduction

In normal fuel cells, the electrochemical half reactions occur at the electrodes. The half reaction at the anode starts slowly and independently by use of catalysts and potential across the electrolyte, but thereafter, it connects to the cathode electrode reaction and the reaction rate goes up and steadies. The reaction layers at the electrodes surfaces are very thin and have not yet been measured practically [5]. The electrochemical reaction occurs on the surface area of the electrodes, so increasing the surface area will increase the reaction rate [5]. For high reaction rate and consequently high current density, electrode areas are increased by increasing porosity. In this section, the effect of the equal electrode areas will be studied. AFC, PEM FC and PAFC are usually fabricated with electrodes, which have equal area and equal thickness. Therefore, this section will be devoted only to AFCs, PEM FCs and PAFCs.

2.4.2 Desired Fuel Cell Reactions

Fuel cells overall reactions (see Table 2.1) are desired to be stoichiometric in order to unleash a high amount of the chemical energy stored in the fuel. Below are the stoichiometric reactions of a fuel cell using hydrogen and oxidizers (oxygen and air). The effects of the equal area electrodes are ignored, and the free energy change, generated voltage, and efficiency are evaluated for each case. The cell voltage and reactions are calculated using eqns. 1 and 3.

(a) H_2-O_2 AFC, PEM FC and PAFC (Reaction conditions: 298K and 1 atm):

Overall Cell Reaction: $H_2 + \frac{1}{2}O_2 \rightarrow H_2O$ (28a)

Solution: $\Delta H = -241845 kJ/kmol$ $\Delta S = -44.16\, kJ/K.kmol$

$$\Delta G = \Delta H - T\Delta S = -228685.32\ kJ/kmol \qquad E = \frac{-\Delta G}{nF} = 1.185\,V$$

$$\eta = \frac{\Delta G}{\Delta H} = 0.94558 = 94.561\%$$

(b) H_2-Air AFC, PEM FC and PAFC (Reaction conditions: 298K and 1 atm):

Overall Cell Reaction: $H_2 + 0.5O_2 + 1.88N_2 \rightarrow H_2O + 1.88N_2$ (28b)

Solution: $\Delta H = -241845 kJ/kmol$ $\Delta S = -44.41 kJ/K.kmol$

$$\Delta G = \Delta H - T\Delta S = -228610.82\ kJ/kmol \qquad E = \frac{-\Delta G}{nF} = 1.185\,V$$

$$\eta = \frac{\Delta G}{\Delta H} = 0.94527 = 94.53\%$$

The reactions indicate that the cell produces the same electrical energy (ΔG), and voltage and have the same efficiencies. But, practically, different results are obtained because of the effect of surface area of the electrode. The effect of the electrodes area does not only make the output of H_2-O_2 and H_2-Air different, it also affects the practical efficiency of the fuel cells.

2.4.3 Undesired Effect of Equal Electrodes Area on Fuel Cell Reactions

The reaction eqns. 28a and 28b are valid only for system where there is actual mixing of the reaction species such as in a combustion chamber. The stoichiometric volume ratio of reactants is usually found as shown below:

$$\begin{aligned} &H_2(g) + \tfrac{1}{2}O_2(g) \rightarrow H_2O(g) \\ &(1mol)H_2 + (\tfrac{1}{2}mol)O_2 \rightarrow (1mol)H_2O \\ &(V)H_2 + (\tfrac{1}{2}V)O_2 \rightarrow (V)H_2O \end{aligned} \qquad (29)$$

In fuel cells, setting the ratio of reactants volumetric flow rates will not ensure a stoichiometric reaction since the cell reactions occurs on the electrodes surface areas. Assuming viscous flow, the velocity of fluid at a surface boundary is very small, and no matter how big the velocity of fluid at the outer region is, the velocity at the surface boundary would still be very small. Setting the ratio of the volumetric flow rates for stoichiometry would also cause uneven pressure across the cell. Since on the electrodes, the reaction layer thickness tends to zero, it is safe to assume that the thickness of the reaction layer at the anode equals that at the cathode. Now, having assumed equal reaction layers at the electrode surface areas, eqn. 29 can be modified as shown below:

$$(1\,Area\,)H_2 + (\tfrac{1}{2}\,Area\,)O_2 \rightarrow (1\,Area\,)H_2O$$

$$(A)H_2 + (\tfrac{1}{2}A)O_2 \rightarrow (A)H_2O \qquad (30)$$

and for H2-air fuel cells

$$(A)H_2 + (0.5A)O_2 + (1.88A)N_2 \rightarrow H_2O + 1.88N_2 \qquad (31)$$

The electrodes are assumed to have the same porosity and thickness, so area, A, represents the cross sectional area of the electrode. The area being considered in this case is similar to the area used for calculating current density. It is the area that is usually specified on electrodes for sell or in the specifications of a new fuel cell e.g. a 25 cm^2 electrode. On the left hand side of eqn. 30, the coefficient of H_2, which is A, represents the area of the anode, while the coefficients of O_2, which is ½A, represents the area cathode. In other words, the active area of the cathode must be half the area of the anode for the cell reaction to be stoichiometric. Similarly, on the left hand side of eqn. 31, the coefficient of H_2, which is A, represents the area of the anode, while the sum of the coefficients of O_2 and N_2, which is 2.38A, represents the area cathode. In other words, the active area of the cathode must be 2.38 times the area of the anode for the cell reaction to be stoichiometric. The analysis used to obtain eqns. 30 and 31 reveals that eqns. 28a and 28b do not

represent the reactions that occur in fuel cells with equal area electrodes. The next section will use the reasoning of this section to analyze the actual performance of equal electrodes area fuel cells

2.4.4 Actual Fuel Cell Reactions

The effects of the equal area electrodes are considered, and the free energy change, generated voltage, and efficiency are evaluated for both the case of O_2 and air.

(a) H_2-O_2 AFC, PEM FC and PAFC (Reaction conditions: 298K and 1 atm):

Overall Cell Reaction: $(3A)H_2 + (3A)O_2 \rightarrow (A)H_2O_2 + (2A)H_2O + (A)O_2$

$$(A)H_2 + (A)O_2 \rightarrow (\tfrac{1}{3}A)H_2O_2 + (\tfrac{2}{3}A)H_2O + (\tfrac{1}{3}A)O_2 \qquad (32)$$

Solution: $\Delta H = -206606.7 kJ/kmol$ $\Delta S = -63.7 kJ/K.kmol$

$\Delta G = \Delta H - T\Delta S = -187624.1 kJ/kmol$ $E = \dfrac{-\Delta G}{nF} = 0.972 V$

$\eta = \dfrac{\Delta G}{\Delta H} = 0.9081 = 90.81\%$

(b) H_2-Air AFC, PEM FC and PAFC (Reaction conditions: 298K and 1 atm):

Overall Reaction: $H_2 + 0.21O_2 + 0.79N_2 \rightarrow 0.42H_2O + 0.58H_2 + 0.79N_2$ (33)

Solution: $\Delta H = -101574.9 kJ/kmol$ $\Delta S = -18.72 kJ/K.kmol$

$\Delta G = \Delta H - T\Delta S = -95996.3 kJ/kmol$ $E = \dfrac{-\Delta G}{nF} = 1.1845 V$

$$\eta = \frac{\Delta G}{\Delta H} = 0.945 = 94.5\%$$

The intermediate reactions between the reactants are connected by the electrode surface areas, so the volume ratio of the products is not considered in the analysis. The hydrogen on the left hand side (see eqn. 33) is left there because it is formed on the cathode side, which is the exhaust side. The first effect of using equal electrodes areas can be seen in eqns. 32 and 33, which are not stoichiometric.

2.4.5 Undesired Effects of Actual Fuel Cell Reactions

The efficiency decrease due to using equal area electrodes for H_2-O_2 FC is 3.75% and for H_2-Air FC is 0.061%. It is not significant, but the values of free energy change and of enthalpy change for the desired reactions are higher due to stoichiometry. Therefore, it is clear that the use of equal electrodes area has more adverse effect on limiting the power conversion capacity of the cells (since only one mole of H_2 was used throughout) than it has on the efficiency of full cells. Practically, the only known PEM fuel cell reaction equation is the stoichiometric reaction, so after manufacturing a fuel cell using equal electrodes area, its performance is measured against the desired stoichiometric equation. Therefore, adopting this measure method, a new term for the energy conversion effectiveness is virtual efficiency defined as

$$\eta_{virtual} = \frac{\Delta G \text{ of actual reaction}}{\Delta \text{H of desired stoichiometric reaction}} \qquad (33)$$

Therefore, $\eta_{virtual}$ for the actual cell reactions considered in section 2.6.5 are given as follows:

For Equal Electrodes Areas:

H_2-O_2 AFC, PEM FC and PAFC: $\eta_{virtual} = 77.58\%$

H_2-Air AFC, PEM FC and PAFC: $\eta_{virtual} = 39.69\%$

The virtual efficiency also stands as the limit of efficiency that can be practically observed in AFC, PEM FC and PAFC designed with electrodes of equal areas and thickness. The virtual efficiencies obtained were compared with average maximum efficiencies of practical fuel cells from different sources (some values found are listed Table 2.3) and it was found that the maximum efficiencies of practical fuel cells using electrodes of equal areas and thickness are lower than their virtual efficiencies.

Table 2.3: Average maximum efficiencies of practical fuel cells from different sources

Fuel cell type	Average maximum efficiency [25]	Average maximum efficiency [26]	Average maximum efficiency [27]	$\eta_{virtual}$
AFC	40%	60%	55%	39.69%-Air 77.58%-O_2
PEM FC	45%	58%	45%	39.69%-Air 77.58%-O_2
PAFC	40%	38%	40%	39.69%-Air 77.58%-O_2

Theoretical analysis similar to that of section 2.4.4 and 2.4.5 was used to obtain the Tables 2.4 and 2.5. It was observed from Tables 2.4 and 2.5 that electrodes area combination that supported less than stoichiometric oxidizer gave lower values of free energy change. Note that for each operational case (which are operations with O2 and air), the same anode area was used to ensure that same amount of fuel cell is supplied to the fuel cell for comparison.

In order to further investigate the effect of the above findings, an actual fuel cell performance experiment was carried out. The experiment is discussed in the next section.

Table 2.4: Free Energy change of H2-O2 PEM FC for various electrodes area ratio

H2-O2 PEM FC					
Anode Area: Cathode Area	ΔH	ΔG	E	η	ηvirtual
1:0.25	-120923	-114305	1.185	0.945274	0.472639
1:0.5	-241845	-228685	1.185	0.945585	0.945585
1:0.75	-206607	-187326	0.971	0.906678	0.77457
1:1	-206607	-187326	0.971	0.906678	0.77457
1:2.38	-206607	-187326	0.971	0.906678	0.77457

Table 2.5: Free Energy change of H2-Air PEM FC for various electrodes area ratio

H2-Air PEM FC					
Anode Area: Cathode Area	ΔH	ΔG	E	η	ηvirtual
0.42:0.25	-60461	-57152	1.185	0.945266	0.236316
0.42:0.42	-101575	-95996	1.185	0.945075	0.396932
0.42:0.6	-145107	-137165	1.185	0.945266	0.56716
0.42:0.8	-193476	-182886	1.185	0.945266	0.756212
0.42:1	-241845	-228611	1.185	0.945279	0.945279

2.4.6 Electrode Area Ratio Experiments

2.4.6.1 Experimental Procedure

PEM Fuel cells with conventional equal electrode areas were setup and ran for operations with O_2 and air. The fuel cells electrodes area ratios were then adjusted for stoichiometry by using polyethylene leather to cover part of the electrode areas (see Fig. 2.34 below). The experiment was setup as shown in Fig. 2.36. The hydrogen cylinder was carefully opened to a low pressure, and then the valve on the hydrogen flow meter was opened slowly until bubbles of hydrogen started forming in the beaker of water containing the hydrogen Teflon pipe outlet.

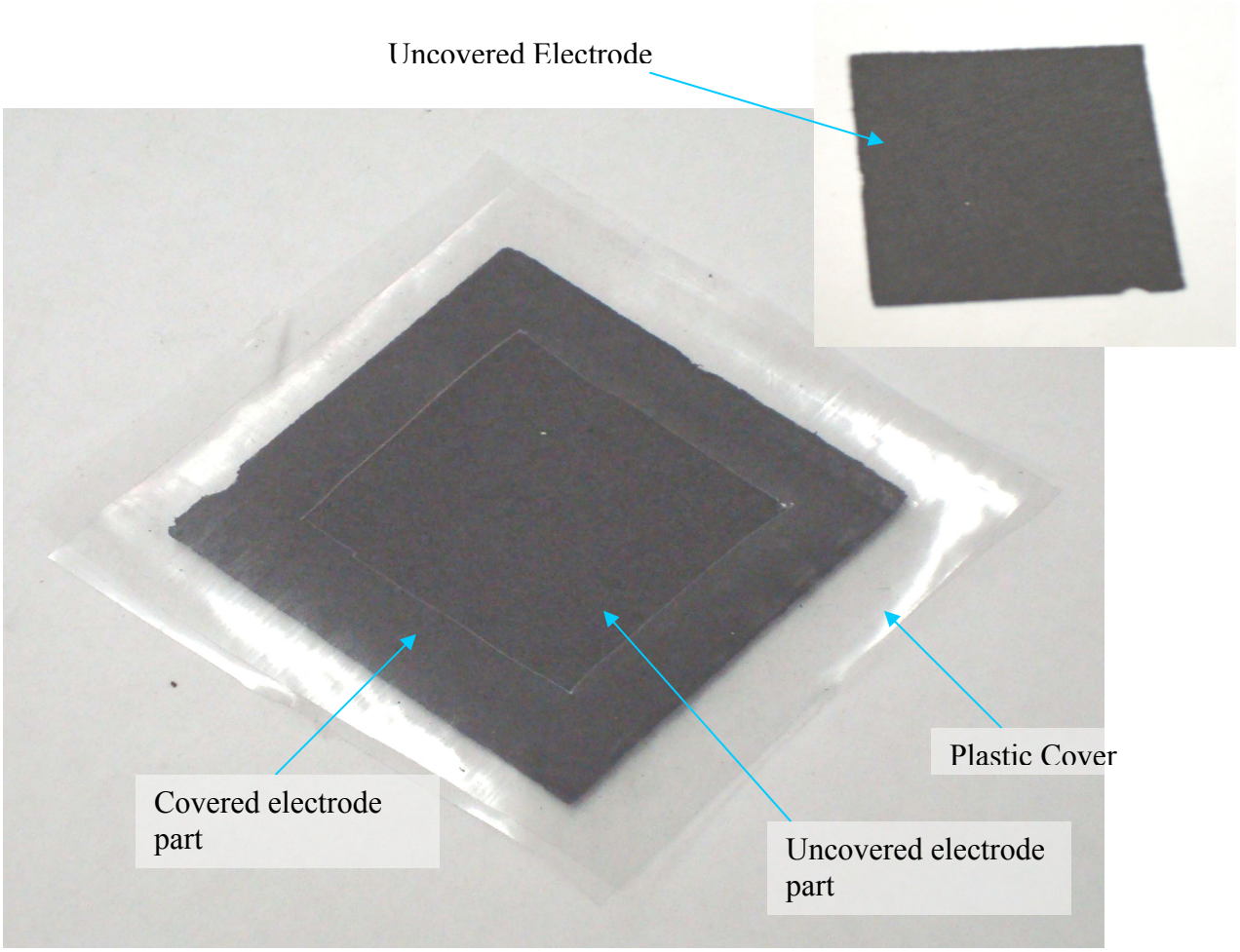

Figure 2.34: Picture of fuel cell electrode partly covered with polyethylene sheet

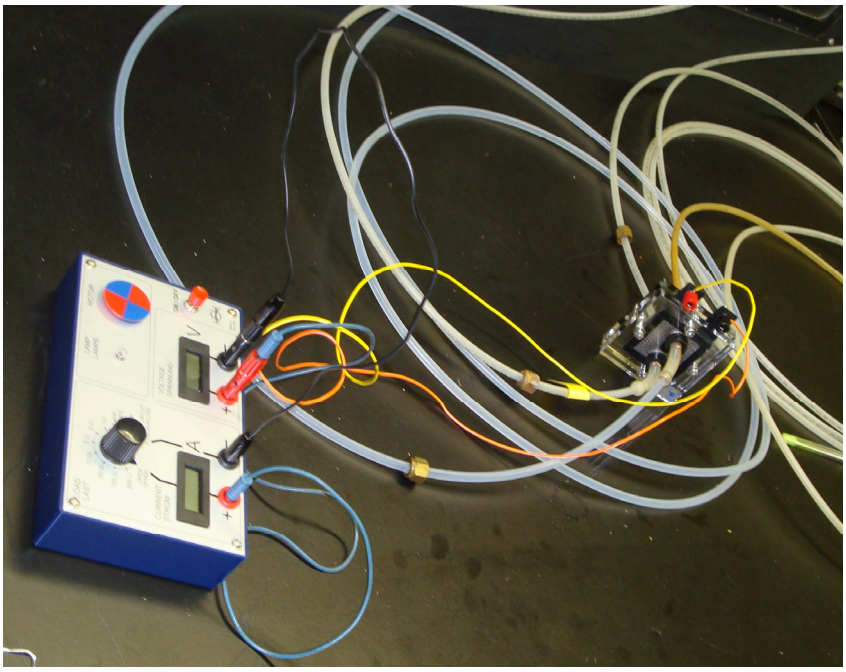

Figure 2.35: Picture of PEM FC experimental setup

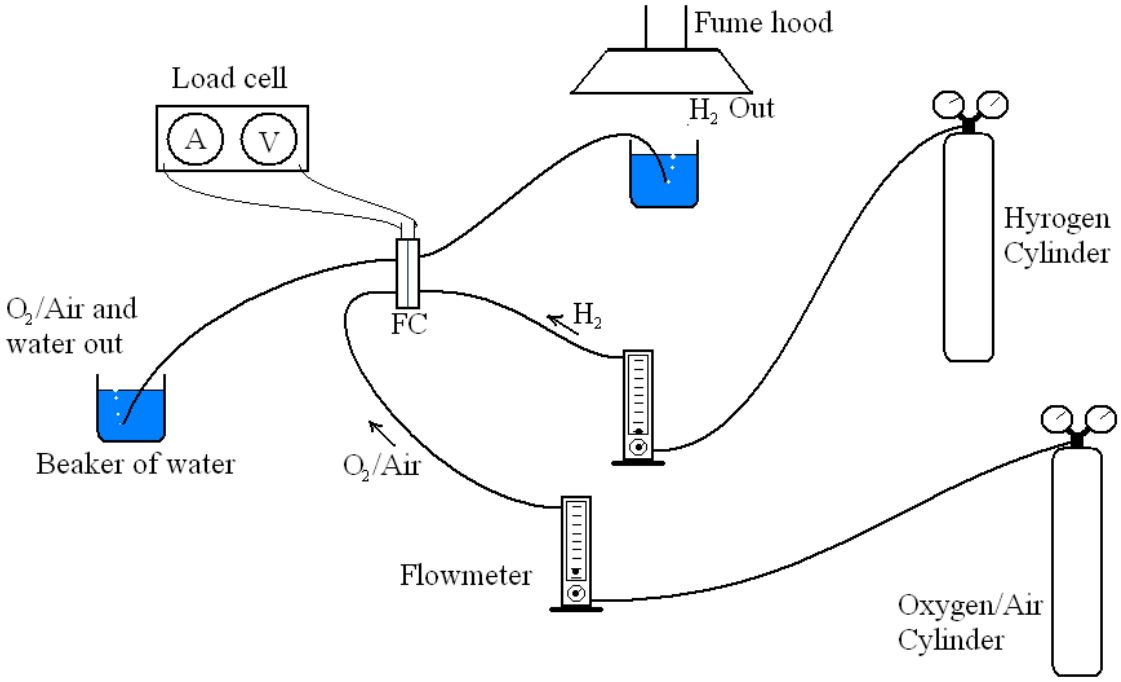

Figure 2.36: Schematic of PEM FC experimental setup

Exactly 5 bubbles escape per minute was used for all the experiments, and at 5 bubbles/min, the reading on the flow meter was negligible. The operational pressure was 1 atm. The flow meter used for oxygen/air was calibrated, so the flow rate of oxygen/air was set to 0.30 liters/min. The same oxidizer flow rate was used for all the experiments in this section. The load cell, whose simple loading circuit is shown in appendix Fig. A.6, was used to load the fuel cells and readings were taken. See Fig. 2.35 for a picture of the experimental setup.

2.4.6.2 **Results**

A plot of the experimental results showed that the performance of the adjusted fuel cells were better than that of the equal electrodes area fuel cells for very low current densities. Data used to obtain plots are given in appendix A.6.

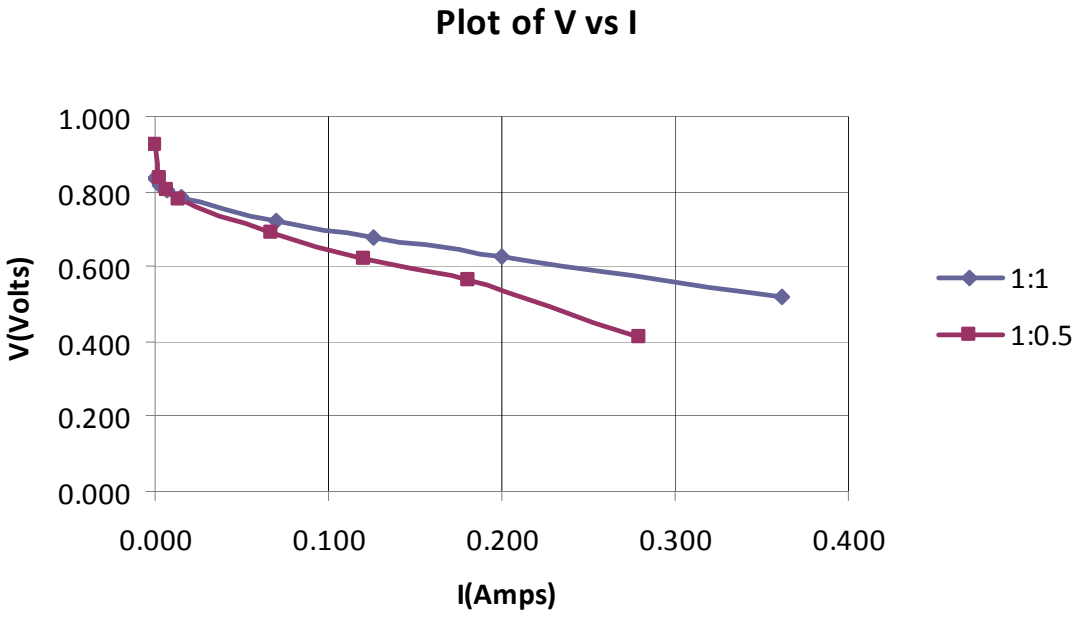

Figure 2.37: Plot of V vs. I for H_2-O_2 PEM FC electrodes area ratio experiment

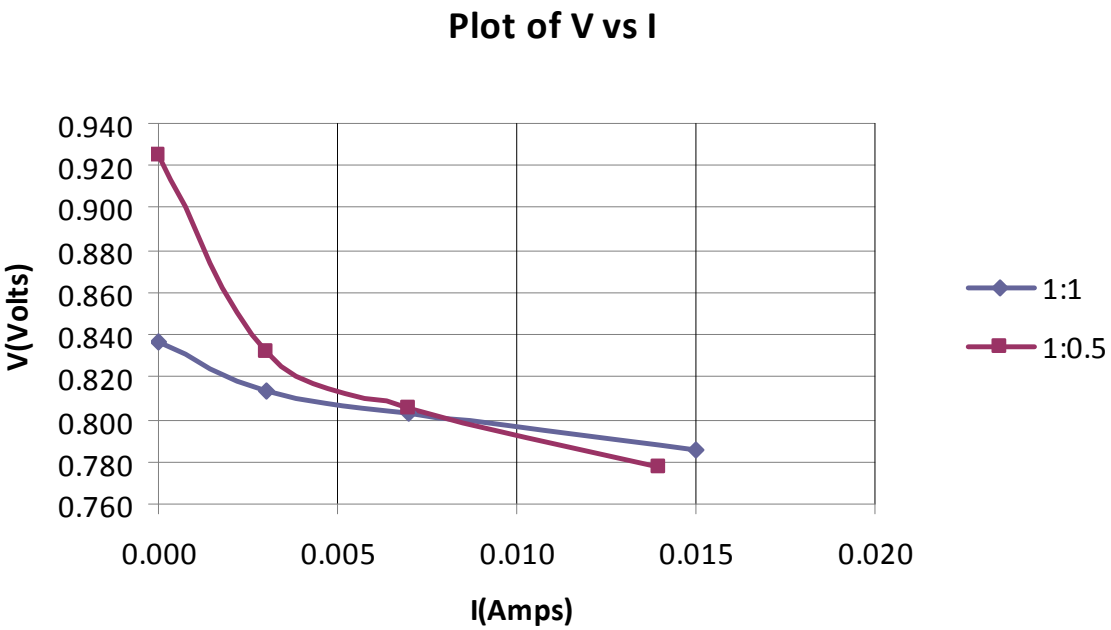

Figure 2.38: Magnified plot of Fig. 2.37

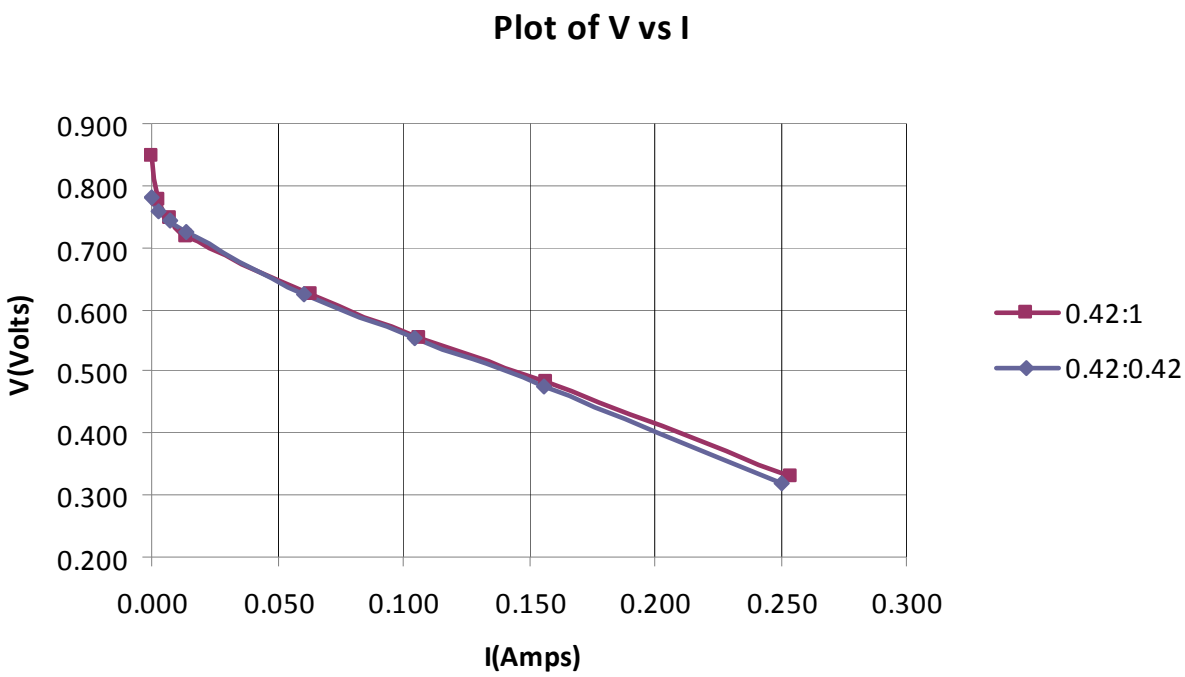

Figure 2.39: Plot of V vs. I for H_2-Air PEM FC electrodes area ratio experiment

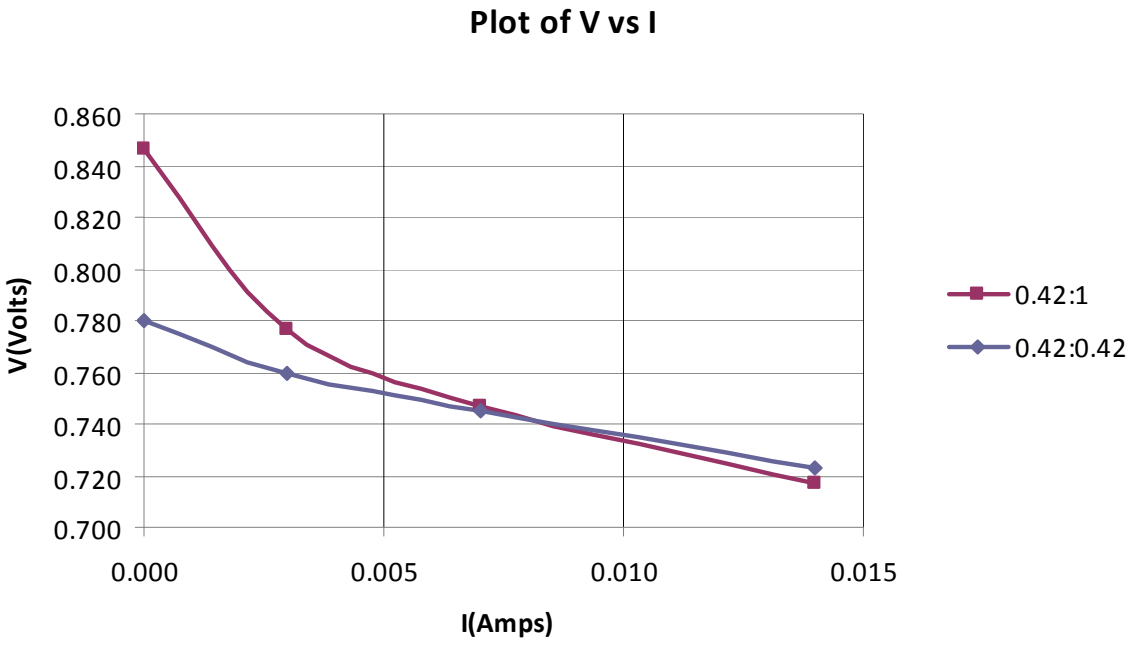

Figure 2.40: Magnified plot of Fig. 2.39

Plots for experiments run with electrode area ratio combinations other than equal and adjustment for stoichiometry were generated and included in the appendix. (See appendix Figs. A.7 & A.8)

2.4.7 Discussion of Results

The analysis showed that the use of equal electrodes area and thickness has the effect of reducing the efficiency of a fuel cell. This is because equal electrodes area and thickness, causes excess or insufficient supply of oxidizer at the cathode. For example, hydrogen protons recombine with electrons to form hydrogen gas due to insufficient supply of oxidizer (see eqn. 33). The hydrogen gas formed at the cathode flows away, burns up and contributes to the waste heat of the fuel cell. The virtual efficiencies obtained for the equal area electrodes in the theoretical analysis were compared to values practically obtained from fuel cells, and it was found that the virtual efficiency are more accurate prediction of fuel cell performance. The efficiency of a fuel cell can be increased by incorporating it in a hybrid with a heat engine. In such hybrids, the heat engine runs on the waste heat of the fuel cell and generates additional useful power. Designing the active electrode area ratio (see Fig. 2.41) to match the stoichiometric reaction equations (eqns. 28a and 28b) has effect on the performance of the fuel cell. AFC and PAFC benefits more from this modification, because their electrolytes are in liquid form and ions can easily move in more than one direction, but PEM FC does not benefit much from such a modification because of its thin membrane whose nano pores mainly allows the diffusion of protons in the direction across the membrane. However, at low current densities, PEM FC does benefit from such change as was shown in the experiments performed (see Figs. 2.37-2.40). Besides operation at stoichiometry, it was observed from additional experiments that electrode area combination for excess oxidizer (more than stoichiometric) caused little decrease or no change in power generated compared to stoichiometric conditions, while electrode area

combination for less oxidizer (less than stoichiometric supply) caused decrease in power generated compared to stoichiometric conditions.

The actual experimental design for the electrode area study was to cut out unwanted electrode area and replace it with non-electrode filling as shown in Fig. 2.41, but due to restriction in the laboratory, the unwanted electrode area was only covered. This implies that the covered electrode part was actively connected to the uncovered area and a small amount of gas may have seeped into the covered area. Though the electrode was only covered, the trends obtained from the experiment were good as shown in the plots.

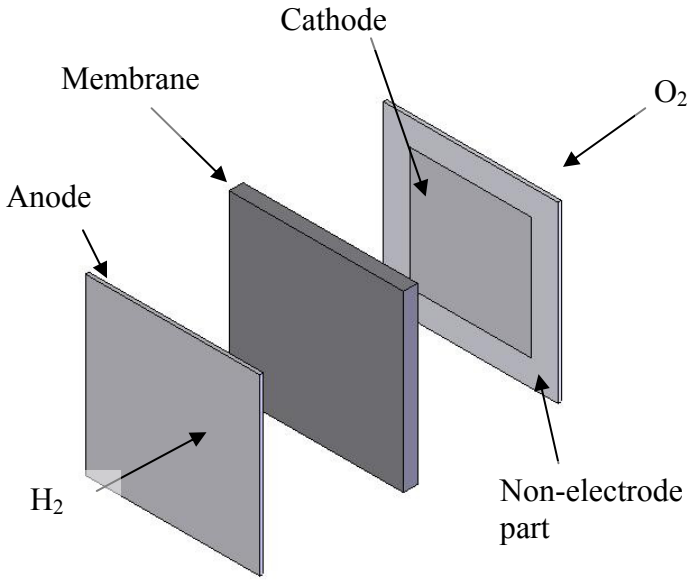

Figure 2.41: Exploded view of a cell with electrodes area ratio adjusted to match eqn. (28a)

2.5 Summary

In summary: CFD was used to study flow channels and a new design was identified, a new expression for the diffusivity of hydrogen protons in PEM was developed, and the effects of

utilizing equal electrode areas in fuel cells were addressed. In the next chapter, CFD will be used to simulate the performance of a high performance flow cytometer.

3. SIMULATION OF A HIGH PERFORMANCE FLOW CYTOMETER

3.1. Introduction to Flow Cytometers

3.1.1 Definition, Applications, and Advantages of Flow Cytometers

Flow cytometry is a method of making rapid measurements on individual cells as they flow in a fluid stream designed to focus the cells to the central line of a pipe or channel [28]. Flow cytometers are devices used to collect data from particles and cells in the size range of 0.5μm to 40μm in diameter [29].

Some advantages of flow cytometers include the following [28]:

a. With flow cytometers, it is possible to make several objective measurements on each individual cell and at a rate of several thousand cells per second. Most cytometers are capable of recording up to 50 parameters from each cell and have speeds of up to 5000 cells per second or more.
b. Some flow cytometers have the ability to electrostatically sort cells into different test-tubes
c. They offers a very high degree of statistical accuracy

Flow cytometry is applied in the following areas [28]:

i. Clinical technology
ii. Cell biology
iii. Cell biochemistry

3.1.2 Brief History of Cytology and Flow Cytometry

Flow cytometry is a method in cytology, so a timeline of developments in cytology is given in Table 3.1. Most of the classical methods (listed in Table 3.1) are excellent for obtaining information about the cell group, but not sufficient for obtaining information about individual cells. Therefore, flow cytometry was born out of the need for both qualitative and quantitative

Table 3.1: Timeline of development in other cytology methods [28, 30]

Method	Year	Brief description	Comments
1. Characterization of morphological features using light absorbing dyes and fluorescent probes	1840s	The categories of stains gives rise to different colors in different sub cellular constituents due to differential binding and hence differential absorption of transmitted light	Method was extensively used by Virchow, 1847 and Waldeyer, 1863
2. Fluorescent antibody probes	1940s	Different molecules or classes of molecules are identified by using different fluorochromes which emit light at different wavelength. It can be combined with the absorption staining method.	Method was used by Coons, Creech, Jones and Kaplan.
3. Immunoperoxidase staining of specific molecules using monoclonal antibodies	1970s	An extension of the staining method	Method was used by Kohler and Milstein

information about cells. Flow cytometry cannot entirely replace existing methods, but flow cytometry can be used to accomplish what other methods cannot accomplish and can be combined with other methods to obtain more information. Flow cytometry was originally developed in the 1930s and has gone through a series of developments. Table 3.2 gives a brief timeline of the development of flow cytometry.

3.1.3 Operational Principle

A flow cytometer consists of three (3) subsystems, namely; (1) Fluidics (2) Optics and (3) Electronics which are further explained below.

Fluidics Subsystem:

The main function of the fluidic subsystem is to use hydrodynamic focusing to draw a stable particle stream to a single file or straight line or curve following the stream central axis.

Table 3.2: Brief timeline of the development of flow cytometry [28, 31]

Year	Major development
1930s	Originally developed from the work of Casperson and Colleagues
1950s	Hemacytometer was used to count cells The Coulter counter was developed (Coulter, 1956) Francis O. Schmitt coined the name term "analytical cytometry" (1950s)
1960s	First Commercial counter was available in market Flow cytometer was used as a fluidic cell sorter by Fulwyler(1965)
1970s	Laser technology was incorporated into cytometers
1980s	Flow cytometry was used to detect single molecules
1990s	Analysis of micro molecules and organelles with cytometer Computer technology was incorporated into flow cytometers Improvement in laser technology resulting in increased precision and higher counting rate

Downstream, the measurements are taken on the cells. The fluidic system works by combining two fluid streams; the cell suspension and the cell-free sheath to form a single cell. The fluidic system aligns the cells by use of the earlier mentioned phenomena, **hydrodynamic focusing**. The flow could be laminar or turbulent and hydrodynamic focusing would occur. However, the flow must be fast enough for the **entrainment of the particles** to occur [31]. Hydrodynamic focusing and particle entrainment are further explained below.

i. Particles Entrainment: Entrainment of particles in a fluid flow occurs when solid particles flow along with the bulk flow of a fluid, rather than falling under gravity to the bottom or rather than moving randomly in the fluid in the case of zero gravity effect. For particles to be entrained by a flowing fluid, there must be a force to push the particles along with the flow. The necessary forces are the lift and drag forces. The lift and drag forces are generated by the strength of the bulk flow, and their resultant must be greater than the weight or inertia of the particles. [31]

ii. Hydrodynamic Focusing: As fluid flows from a larger diameter to a smaller diameter in a tube, velocity increases since constriction is encountered. The acceleration leading to the change in velocity starts where the boundary layer effect sets in. Consider Fig. 3.2, the shaded region of the fluid is squeezed into a very thin layer in the low diameter region by the effect of the high velocity. For a ratio of higher diameter to lower diameter of 5:1, the core of the fluid would be compressed to 1/5 of its original layer thickness. Particles entrained by the fluid flowing through a tapering constriction are constrained to the centerline of the channel by the boundary layer effect. This phenomenon is called hydrodynamic focusing and is the main basis of operation of a flow cytometer. Let's consider a water container being drained at the bottom. Hydrodynamic focusing phenomena can be demonstrated by carefully and slowly pouring a dye into the draining water as shown in Fig. 3.1. A close observation of the drain and region close to the drain (see Fig. 3.2) reveals that the dye is compressed into a very thin layer in the low diameter drainage pipe. Theoretically, for a higher to lower diameter ratio of 5:1, the dye region of the fluid would be compressed to 1/5 of its original thickness. Fig. 3.3 gives a typical set up of the fluidics subsystem of a flow cytometer. The flow chamber is the main part of interest, since its performance will be simulated in this project. There are two main types flow chamber designs: Analytical chambers and flow chambers for cell sorters [31]. The **analytical chambers** are generally designed for laminar flow conditions and are further subdivided into two types: The first type is the microscope-based flow chambers, which characteristically have a thin flat glass cover slip that allows for easy focusing of microscope to the fluid flowing in chamber. The second type is the laser-based flow chambers, which utilizes a flat sided cuvette to minimize unwanted light reflections from the cover. Flow chambers for cell sorters are chambers specially designed for cell sorters. These chambers are usually designed with electrostatic devices incorporated in the chamber. Flow chambers for cell sorters are further classified into two types:

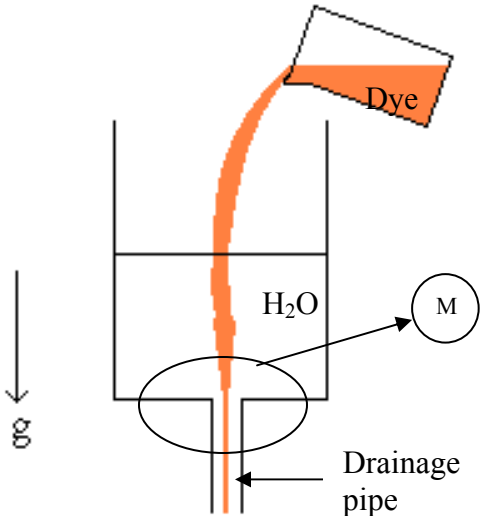

Figure 3.1: Hydrodynamic focusing [31]

The first type is chambers with square channel cuvette and are designed for laminar flow conditions. The second type is chambers designed for turbulent flow conditions.

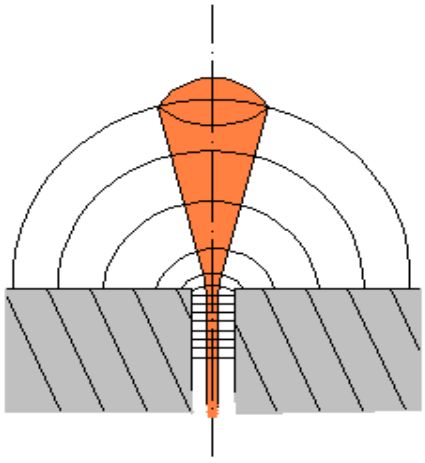

Figure 3.2: Magnification M of Fig. 3.1 showing hydrodynamic focusing phenomena [31]

The **optics and electronics subsystems consist** of the light or laser equipment and electronic devices used for collecting data from the cells or for sorting the cells. Therefore, the whole flow cytometer is a sophisticated device and is sometimes computerized.

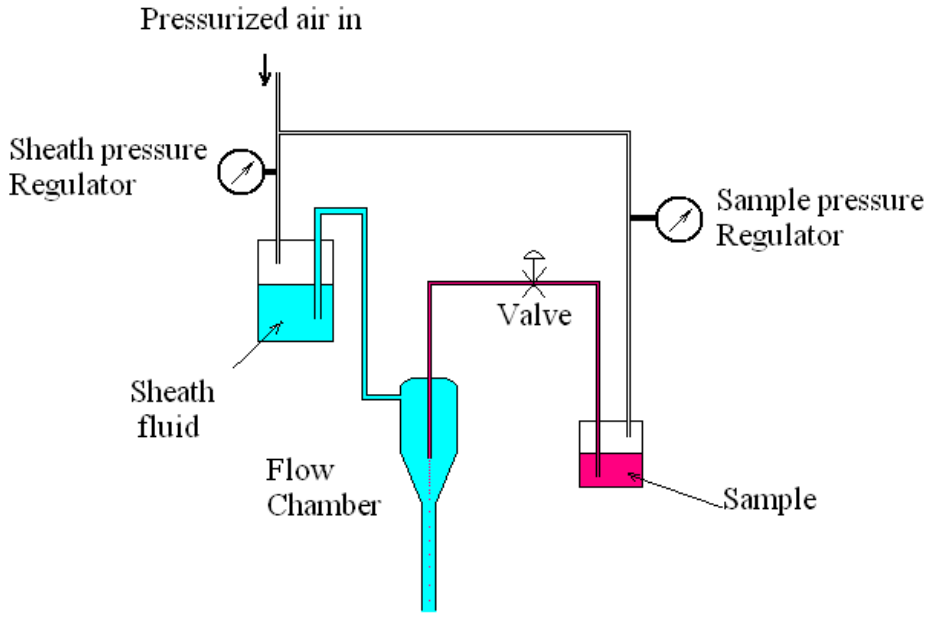

Figure 3.3: Typical set up of the fluidics subsystem of a flow cytometer [31]

3.2. Literature Review

Yang and coworkers [1] designed the high performance flow cytometer that will be simulated in this project. The designed flow chamber is micro-sized and will use low flow rates for obtaining hydrofocusing. The flow chamber was designed to operate on low Re (Re<2300), so the flow should always be laminar. The designed flow chamber has a rectangular cross-section and 30^0 chamfers on the lower sides of the tapering region (see Fig. 3.4). Prototypes of the flow chambers were manufactured with SU-8 polymer, which has excellent thermal stability and resistance to a wide variety of chemicals. A glass slid was used for the top cover. SU-8 is the

recommended material for manufacturing the designed flow chamber, because the complex shaped micro size chamber can easily be manufactured using SU-8 lithography. Four different

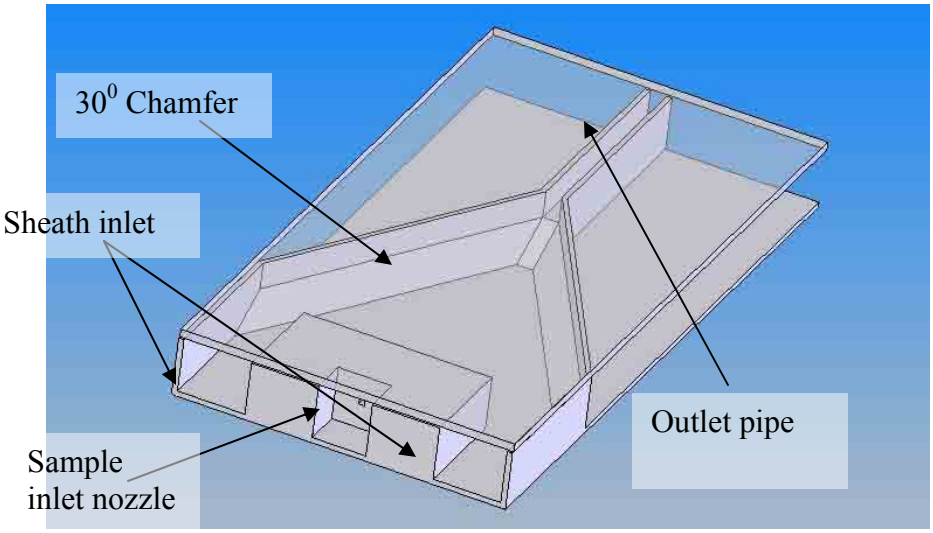

Figure 3.4: Solid model of a high performance flow cytometer [1]

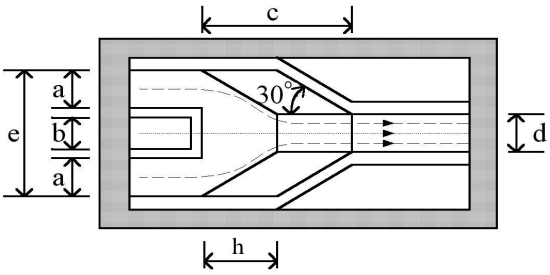

Figure 3.5a: Plan view with dimensions [1]

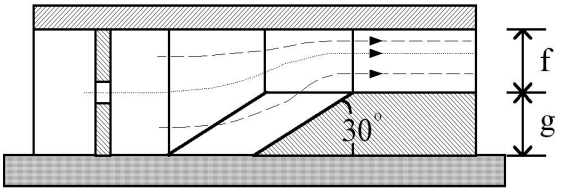

Figure 3.5b: Section with dimensions [1]

Table 3.3: Flow cytometer dimensions with numerical values for dimensions in Fig. 3.5

Shape	Shape 1	Shape 2	Shape 3	Shape 4
Parameters (µm)	d = 100 µm	d = 300 µm	d = 500 µm	d = 1000 µm
a	1154.7 µm	1254.7 µm	1354.7 µm	1604.7 µm
b	1000 µm			
c	5976.5 µm			
e	5810 µm	6009.4 µm	6209.4 µm	6709.4 µm
f	500 µm			
g	500µm			
h	1032 µm		1465 µm	
The injector nozzle is a square shape with side length 100µm; the center of the square is 500µm high.				

shape configurations with exit flow cytometers with hydraulic diameters of 143, 273, 333 and 400 μm were designed and prototype manufactured (see Fig. 3.5 and Table 3.3). Yang and coworkers performed experiments using the manufactured prototypes to assess the performance of the flow cytometer. They used syringe pumps to drive the fluid flow. Fig. 3.6 gives a sketch of the experimental setup.

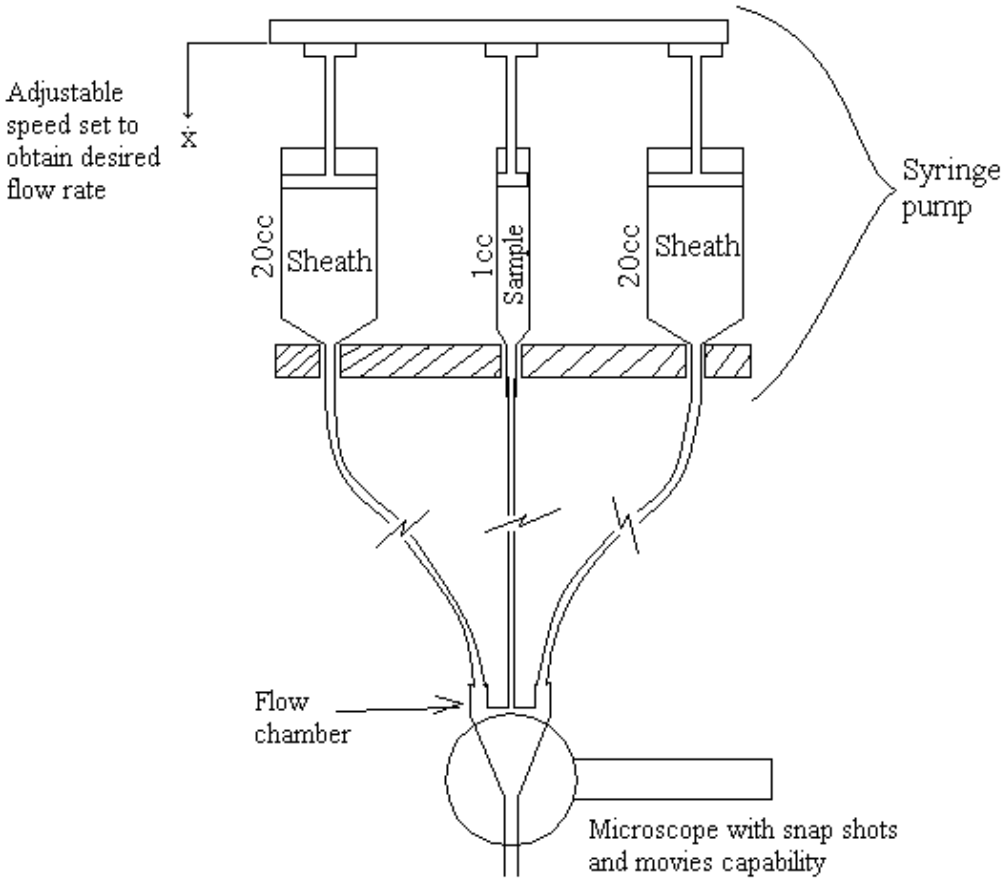

Figure 3.6: Yang's experimental setup (drawn to match [2])

The experiment was first performed using flourecein dyed microspheres suspension as sample, and distilled water as sheath. Hydrofocusing of the sample was obtained. A second experiment was performed using sheep red blood cells as sample and saline water as sheath. Similarly, the

cells were hydro focused even though the movie was blurred. In summary, the experimental result was good, but it had some limitations. For example, the camera could not focus to the dye/cells due to the thickness of the slid glass, and the image taken through the cytometer sides was poor due to poor transparency of SU-8.

This literature review is mainly a review of the experimental method used by Yang to check the performance of the designed flow chamber, because this part of the project is aimed at using CFD to check the performance of the flow cytometer. For a review of flow chambers design work preceding Yang's design, see References 1 and 2.

3.3. Flow Cytometry Simulation

The flow cytometer simulation will involve the modeling of the flow region of the chamber only. The complex flow delivery systems seen in Figs. 3.3, 3.6 wont be modeled, because fluent can be used to directly simulate the delivery of fluid to the flow region of the flow cytometer. Four different sizes (see Table 3.3) of the flow cytometer were modeled using Gambit, which is the preprocessor program of Fluent CFD. One of the modeled flow cytometer and its mesh generated flow region is shown in Fig. 3.7a below. The flow cytometer has a complex flow region, so a hybrid grid was used to generate for the flow region (see Fig. 3.7a). The model was meshed to the smallest possible grid size (see Fig. 3.7b). The smallest possible grid size was found by reducing the grid size until an undesirable negative volume was obtained, and then the previous size was used. The smallest grid size found and used for shape 2 is 0.11mm (see preprocessing script in appendix A9).

The following flow conditions and substances were used to model the flow cytometers:

Flow rate ratio: $\frac{\text{Sample (inner) volumetric flow}}{\text{Sheath volumetric flow}} = 0.025$

Water (Primary fluid or sheath): $\rho = 1000 Kg/m^3$, $\mu = 0.001003$ Kg/m - s

Blood plasma (Secondary fluid or sample): $\rho = 1200 Kg/m^3$, $\mu = 0.0015045 Kg/m-s$

Blood cells (modeled as oblate shaped particles with the properties of a human red blood cell):

Shape factor = 5, $\rho = 1800 Kg/m^3$ and Cells diameter = $7 \mu m$

Since the actual size of the micro flow cytometer was used, fluent was set to a lower convergence criterion. The simulation was performed, and the results were processed and stored (see appendix A.9 for grid generation and simulation procedure). Shapes 1, 2, 3 & 4 were simulated with flow conditions with inlet Re = 0.1, 1, 10, 50, 100, 200, 400, 600, 800, 1000, 1200, 1400 and 1600.

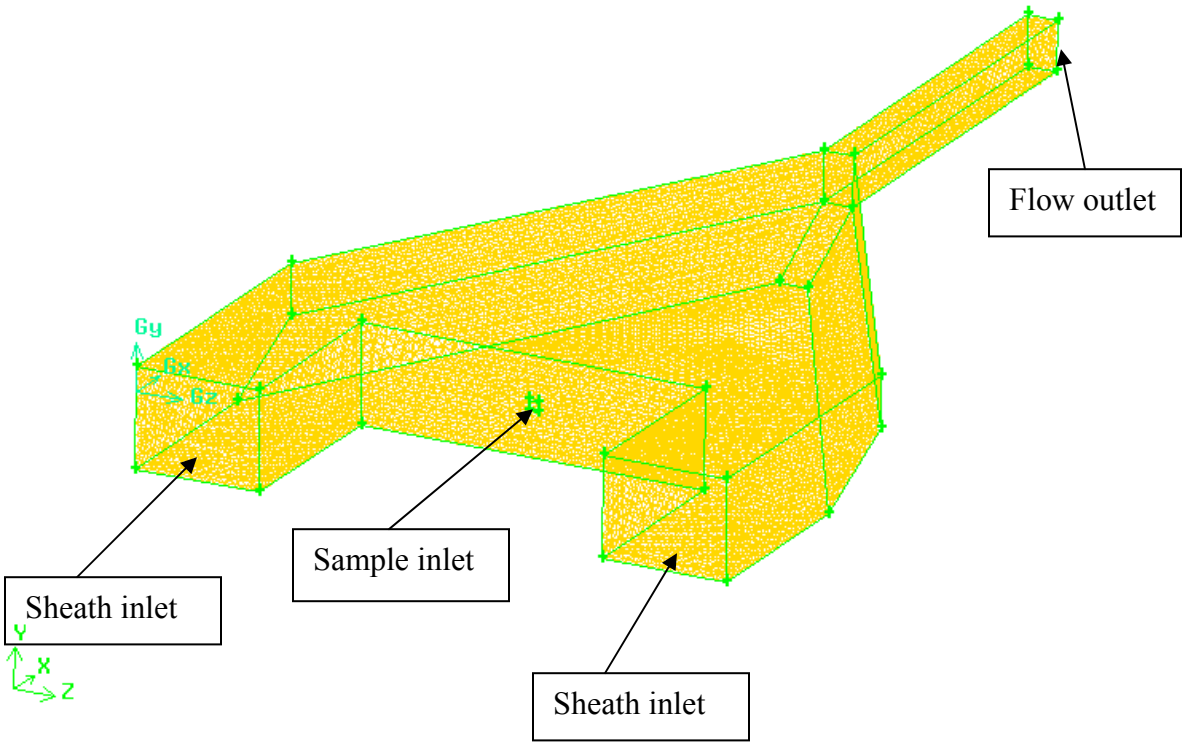

Figure 3.7a: Gambit model showing coordinate system, flow directions and mesh [1]

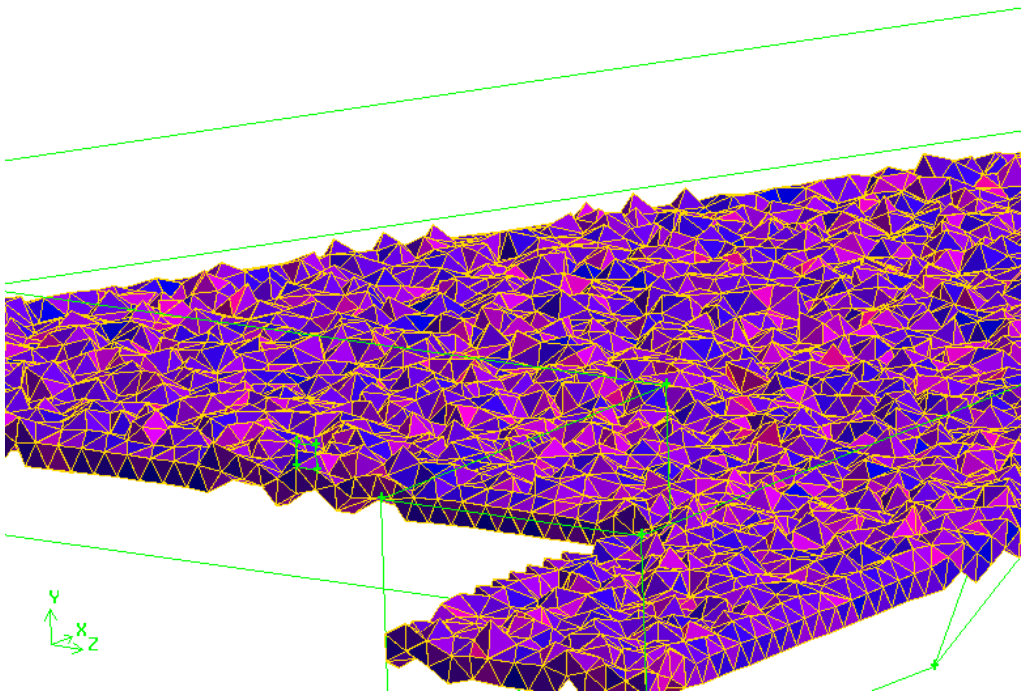

Figure 3.7b: Part section of the hybrid grid generated for the flow cytometer

3.4. Results and Discussion

The simulation results show hydrodynamic focusing of blood cells (see Figs. 3.8-3.11) in the exit pipe. The computer lost track of some blood cells due to the small size, shape factor and or motion, but majority (~96%) of the blood cells were successfully tracked. Hydrodynamic focusing was obtained in 3-D. However, the focusing was different in the different 2-Ds. The focusing obtained in the plan view 2-D was better than the focusing obtained in the side view 2-D (see Fig. 3.8 and Fig. 3.12). The simulation result was checked with Ren Yang's experimental result and both results matched (see Fig. 3.13) under the same flow conditions. A careful observation of all the simulation results revealed that the hydrodynamic focusing of blood cells increases with increase in the sheath flow rate and bigger exit pipe diameter requires higher

sheath flow rates for hydrodynamic focusing of blood cells. The blood cells were not entrained by the fluid flow at low flow rates(see Fig. 3.14), rather the cells moved in random motion.

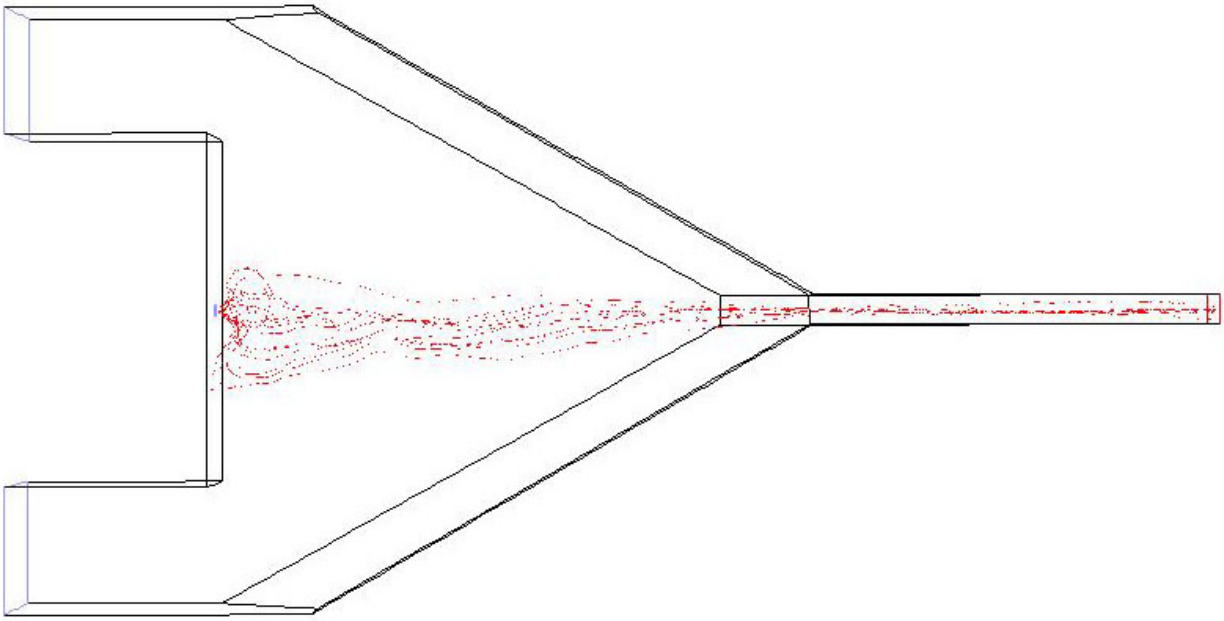

Figure 3.8: Plan view of simulation result using shape 2 and sheath flow rate = 3.6e-6 kg/s

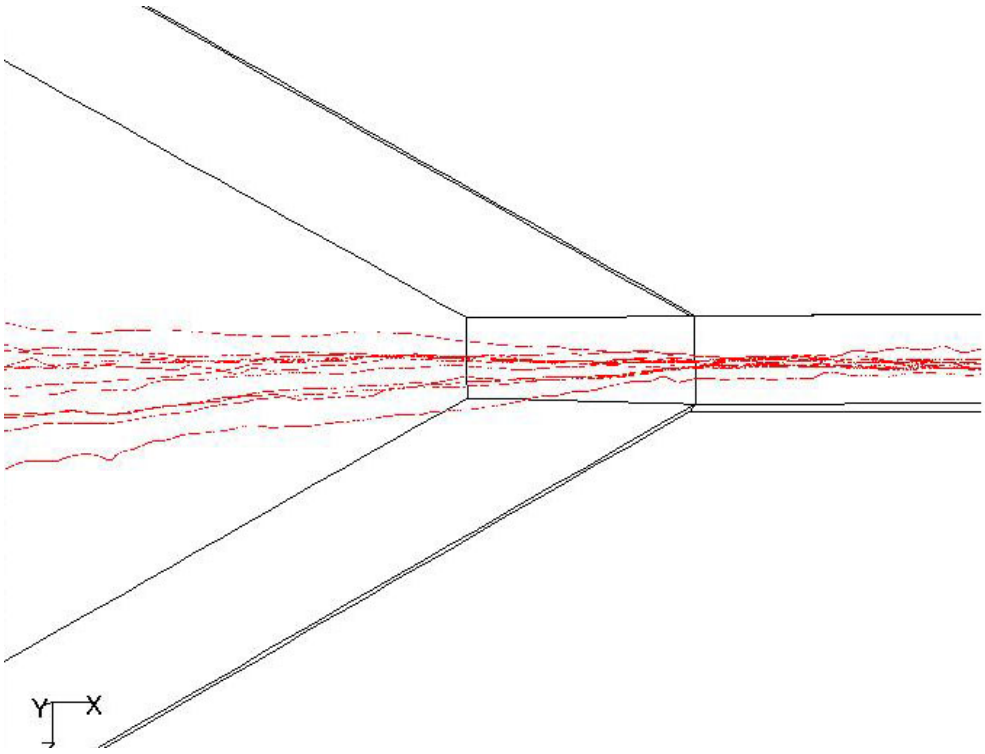

Figure 3.9: Magnified plan view of region close to sample inlet of Fig. 3.8

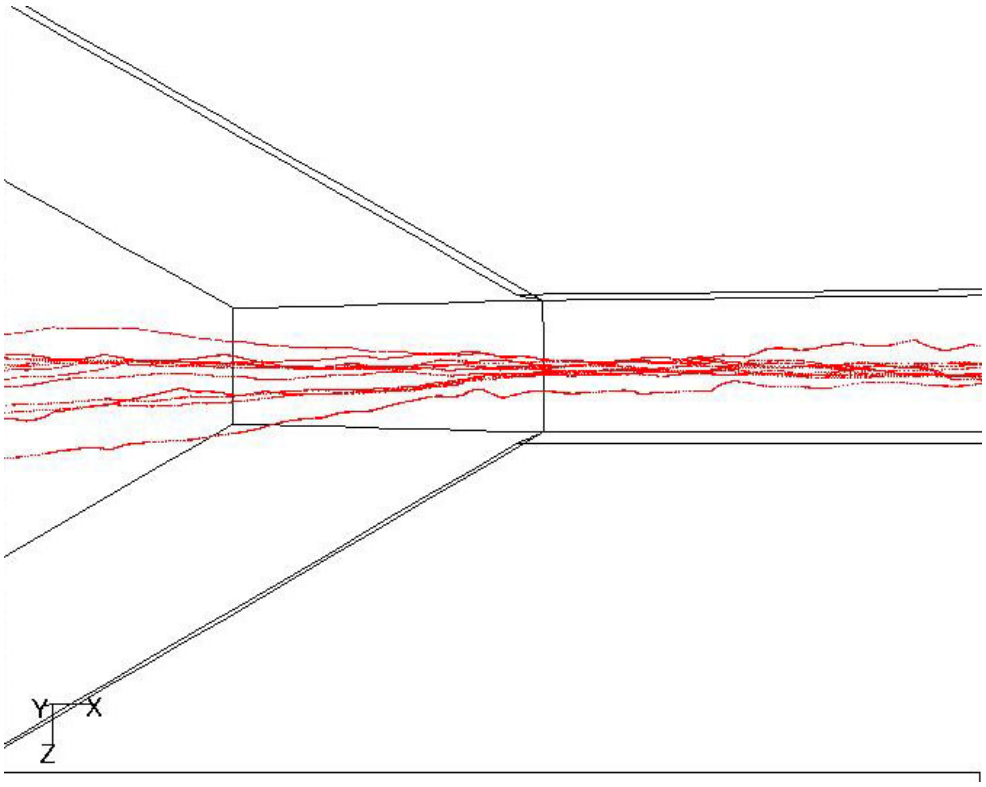

Figure 3.10: Magnified plan view of taper end region of Fig. 3.8

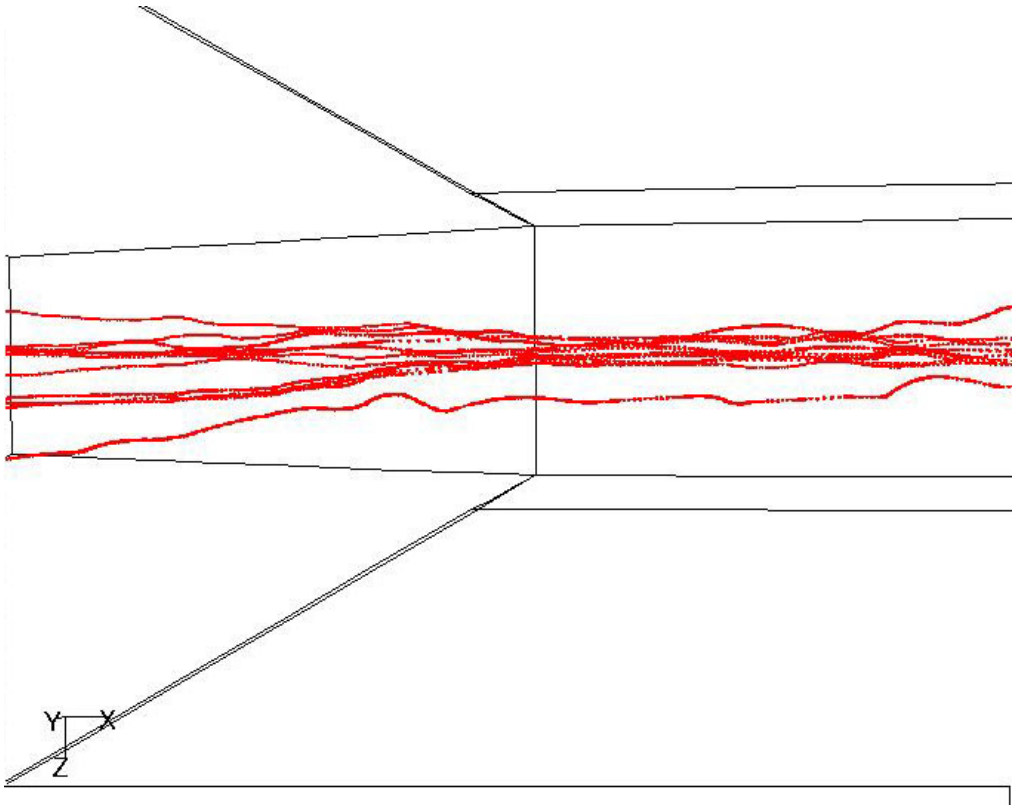

Figure 3.11: Magnified plan view of taper end region of Fig. 3.10

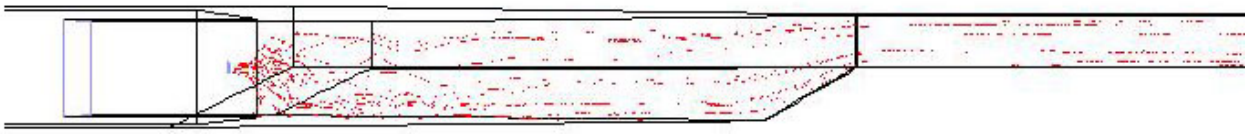

Figure 3.12: Side view of simulation result using shape 2 and sheath flow rate = 3.6e-6 kg/s

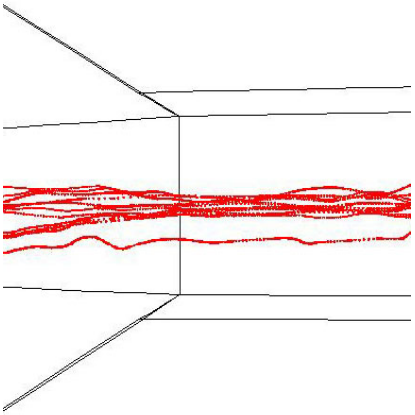

Figure 3.13a: Simulation Result

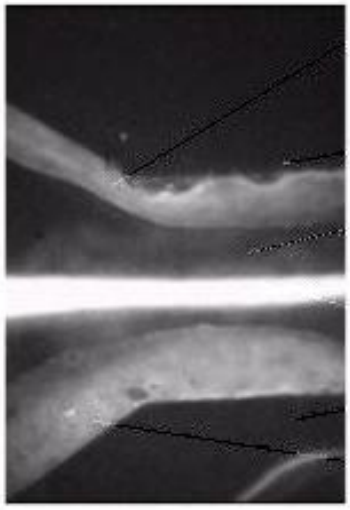

Figure 3.13b: Experimental Result

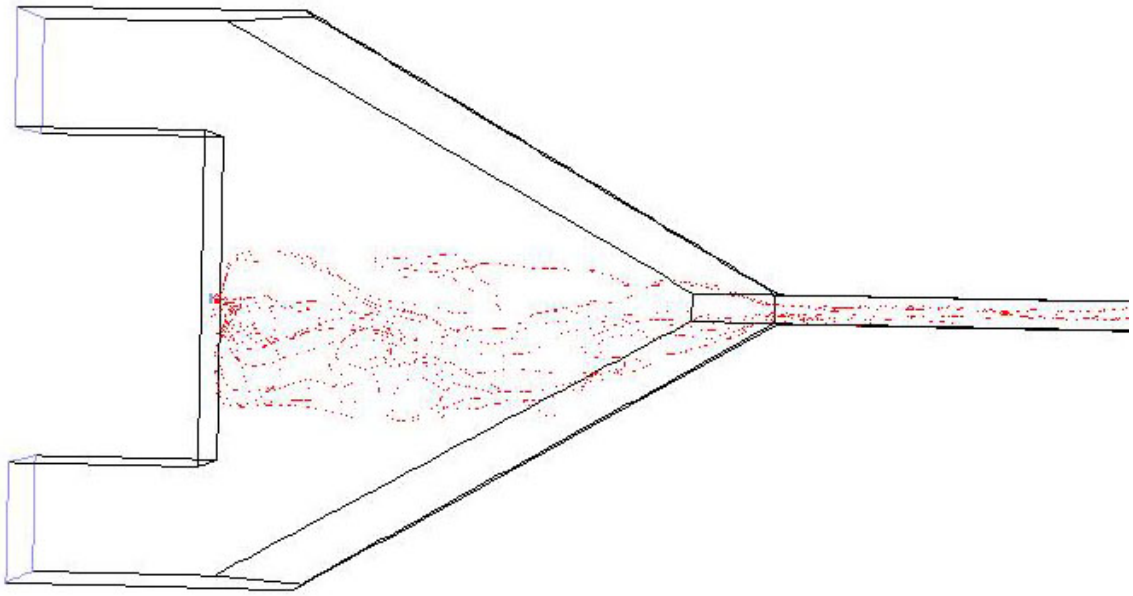

Figure 3.14 Plan view of simulation result using shape 2 and sheath flow rate = 3.6e-8 kg/s

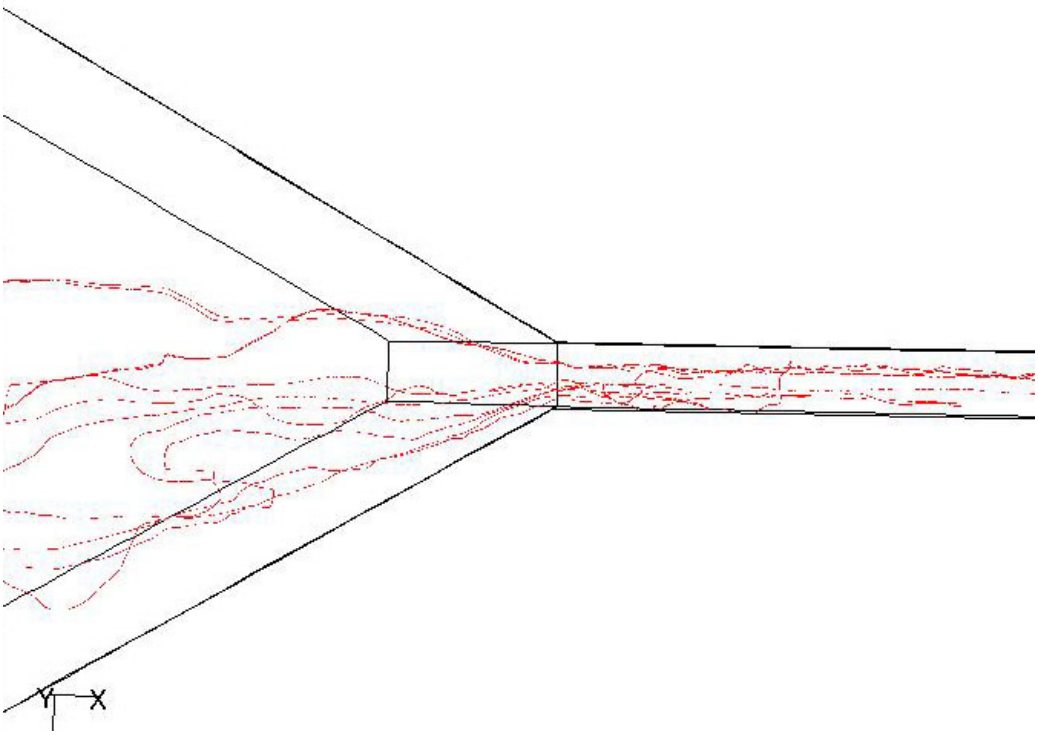

Figure 3.15: Magnified plan view of taper end region of Fig. 3.14

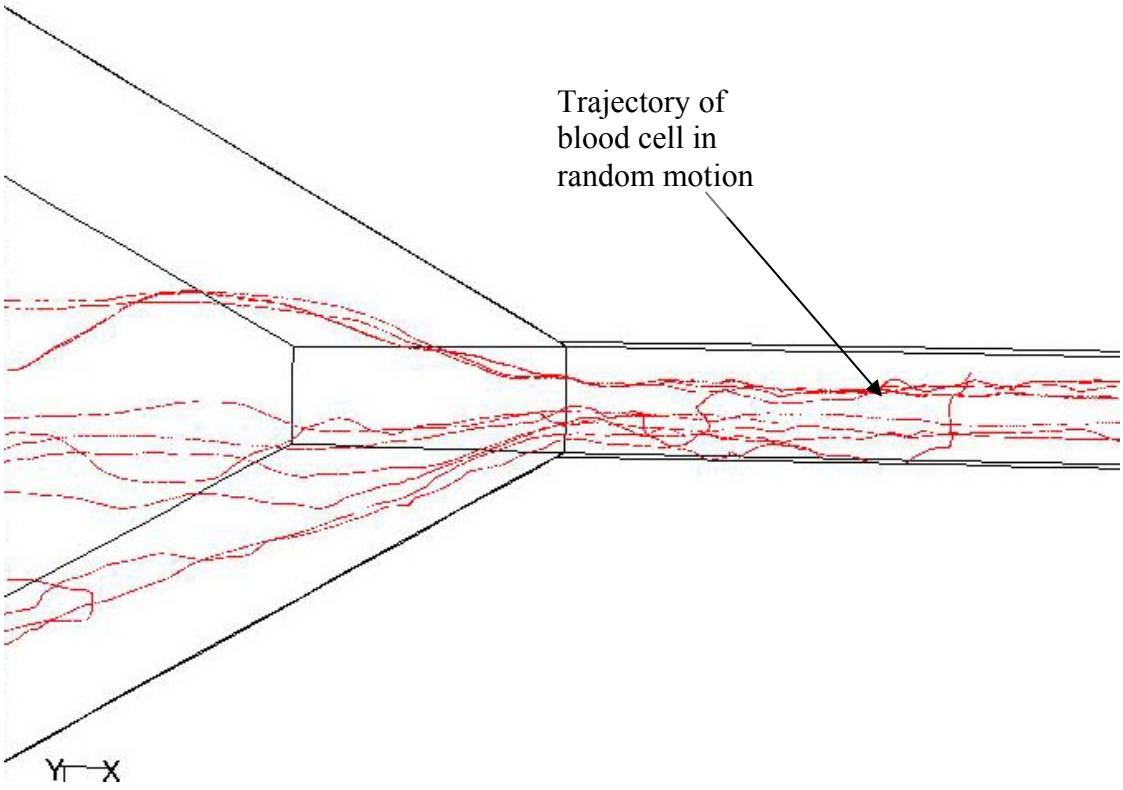

Figure 3.16: A further magnification of plan view of taper end region of Fig. 3.14

3.5 Optimization of Flow Cytometer Design

3.5.1 Introduction

Ren Yang used four different shape configurations without any comment about their differences in performance. Thus, a careful study of the performance of the four shapes using CFD revealed that shape 1's outlet diameter is too small, so it causes reverse flow, flow reflection and poor focusing. Shape 2 performed best, but shapes 3, 4 gave poor hydrodynamic focusing and will require high flow rates to achieve hydrodynamic focusing. The high flow rate is undesirable because it will cause the cells in the exit pipe to flow faster making it harder for optical analysis or sorting. Therefore shape 2 was selected to be modified to obtain the best streamlined flow into the exit pipe without any flow reflection, so that the best focusing of blood cells can be obtained.

3.5.2 Design

Shape 2 of Yang's design was selected because the exit pipe has diameter close to 250μm, which is typically the minimum exit channel to help prevent blockages and unwanted reflections from the wall [31]. The goal is still to design a flow cytometer that operates under laminar flow conditions and provide the best hydrodynamic focusing of blood cells. Analysis of simulation results in section 3.4 was mainly focused on tracking the blood cells; however, the sheath flow properties and flow chamber boundaries will now be considered in order to optimize the flow chamber design. Fig. 3.17 shows the boundary layer property of the sheath flow due to the shape of the flow chamber. The traced out region boundary layer is the desired positions of the walls, but there is a region with unwanted eddies (see Fig. 3.18). The boundary layer with the eddies causes the blood cells to spread out before re-converging and causes the final focusing of blood cells to be poor. The region was eliminated by flipping part of the boundary layer close to the sample inlet. The sample inlet nozzle was shifted forward (see Fig. 3.19).

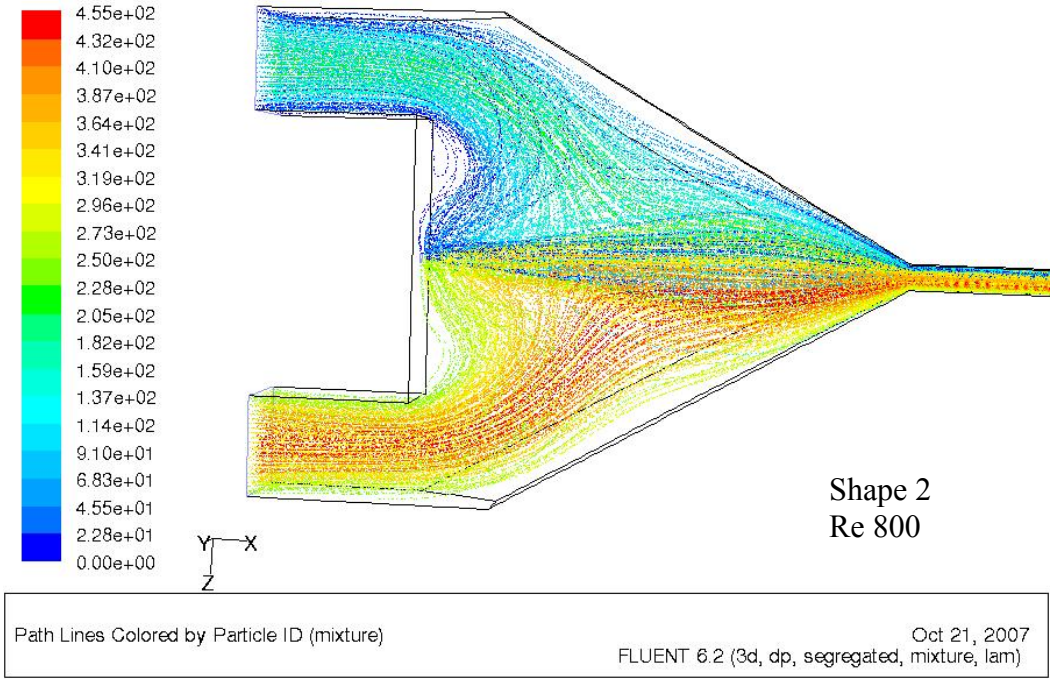

Figure 3.17: Path lines of sheath flow showing boundary layer.

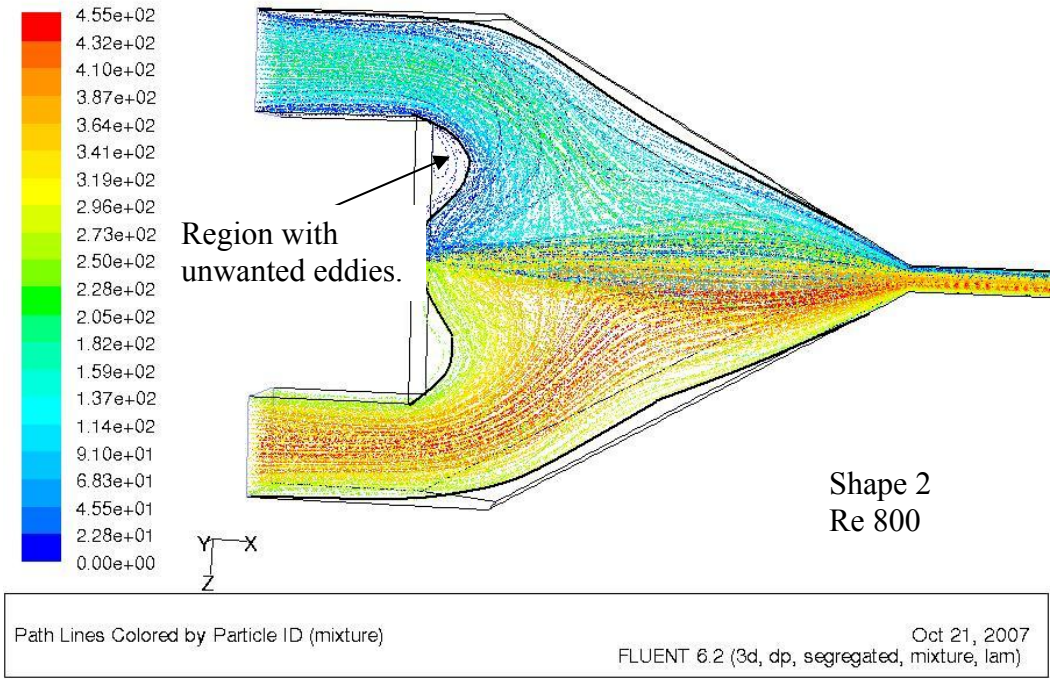

Figure 3.18: Traces of boundary layer

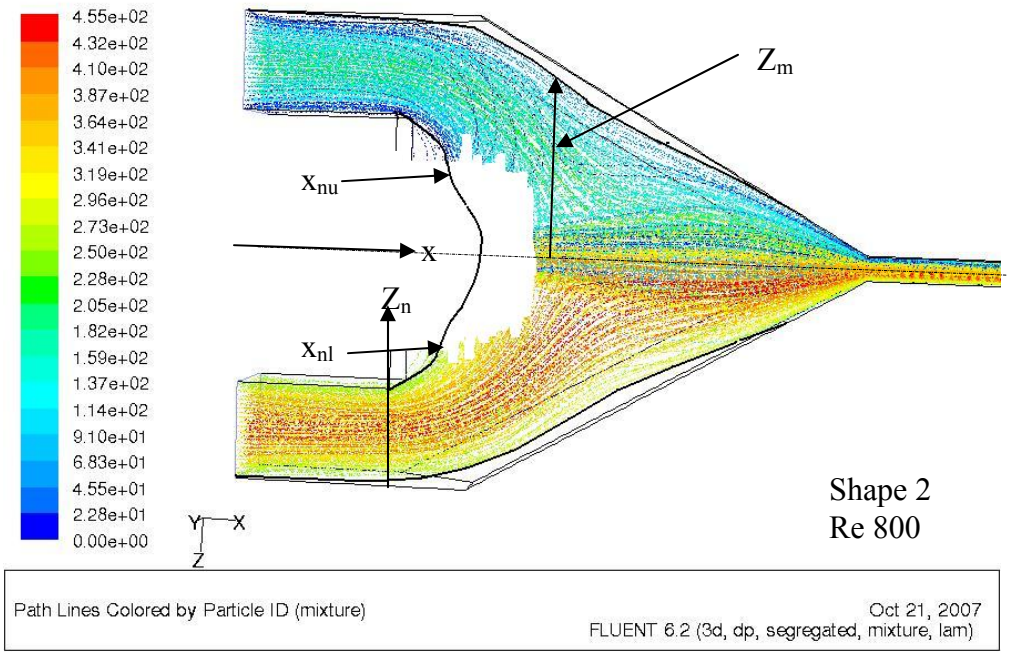

Figure 3.19: Optimized flow chamber profiles of the flow cytometer

The best profiles found are given below (see appendix A.10 for curve fitting of optimized profile):

$$Z_m = (-3.824866\times10^{-5})x^6 - (3.038344\times10^{-4})x^5 + 0.01677096x^4 - 0.1419146x^3 + 0.3720673x^2 - 0.357108947x + 2.83644746 \quad (35)$$

$$x_{nl} = 3.7646Z_n^{\,6} - 49.2326Z_n^{\,5} + 263.4674Z_n^{\,4} - 737.6720Z_n^{\,3} + 1138.3524Z_n^{\,2} - 916.2827Z_n + 302.0540$$

$$x_{nu} = 3.7646Z_n^{\,6} - 86.5068Z_n^{\,5} + 823.4563Z_n^{\,4} - 4155.9469Z_n^{\,3} + 11728.2076Z_n^{\,2} - 17546.5365Z_n + 10876.0779$$

where $x_n = \begin{cases} x_{nl} & \text{for } 1.433271 \le Z_n \le 3.0047 \\ x_{nu} & \text{for } 3.0047 \le Z_n \le 4.5761 \end{cases}$ (36)

Z and x are in mm. (In appendix A.10 Fig. A.9 is for curve fit of symmetric Z_m and Figs. A.10 and A.11 for curve fits of x_{nl} and x_{nu} respectively.) A model of the optimized design was created and simulation was run to check the improvement in performance of the flow cytometer (see Fig.

3.20). The optimized design was obtained by tracing out the boundary layer and pushing the sample inlet side in. Changes were made till the optimum design was obtained. The optimization process used is summarized in Fig. 3.21. A variation of the flow rates within the laminar flow regime of $10 \leq Re \leq 1400$ produced negligible change to the optimum design, hence a rigid optimum design was obtained with profiles given in Fig. 3.19 and Table 3.3.

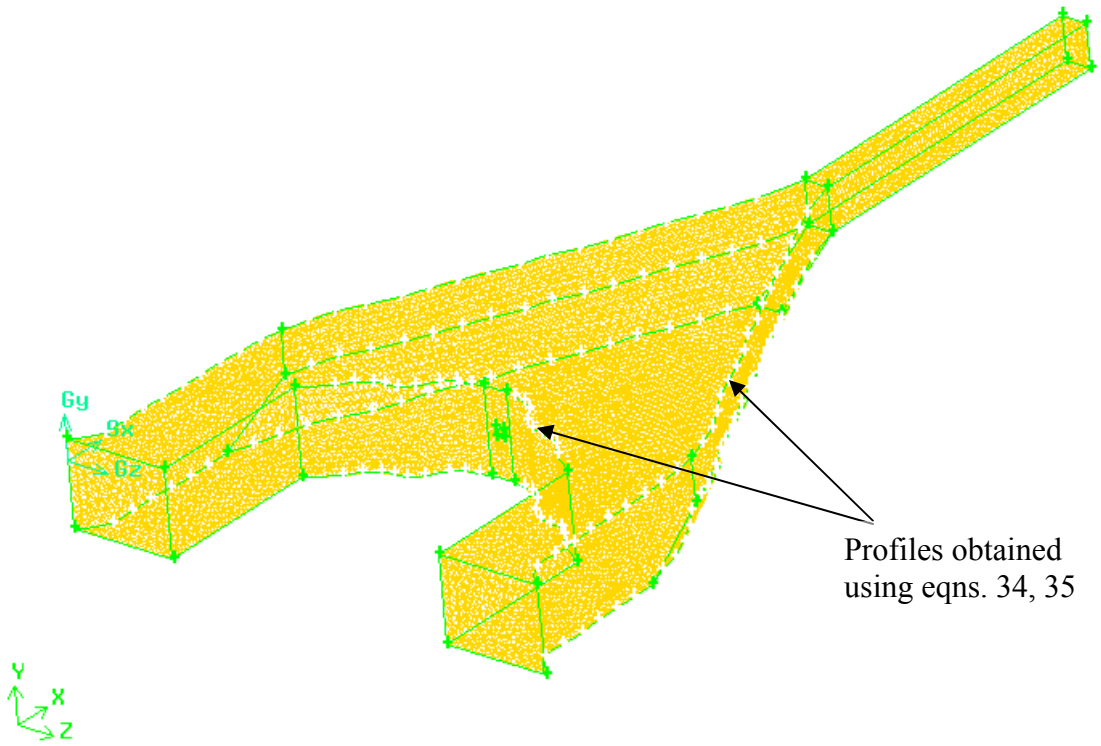

Figure 3.20: Gambit model of optimized flow cytometer

All the dimensions of shape 2 remains the same except the straight edges around the tapering region are replaced with the optimized profiles. The two-optimization methods used are the geometric optimization and topological optimization. Geometric optimization is useful when it is desirable to change the prototype's shape during the design process [32]. The change, which is preferably referred to as modification, is usually done to ensure that the design meets performs

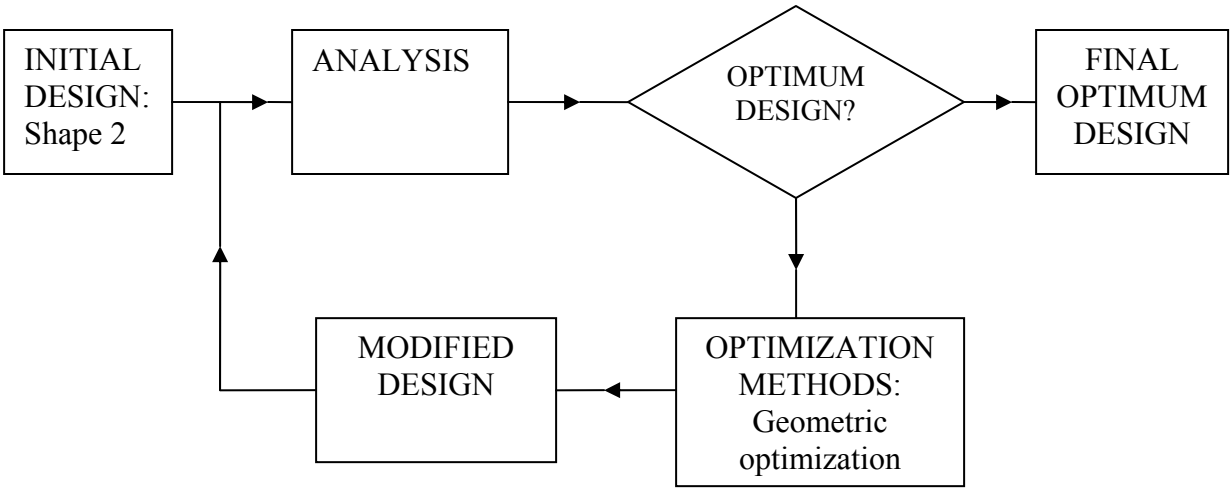

Figure 3.21: Optimum design flow chart used to optimize the design of the flow cytometer [32]

as desired under a set of constraints. In this project, the shape of the profile was changed and simulation was used to check its performance against the original design.

3.5.3 Simulation Results and Discussions

Simulation results of the optimized design showed the hydrofocusing of blood cells. (See Figs. 3.22 through 3.25.) The results are similar to what was obtained for the original design, but what are the differences between the two designs? The answer will be found by a direct comparison of both results place close to each other. (See Figs. 3.26 through 3.28)

Some direct comparisons:

Comparing the simulation results of the optimized design with the results of the original design (see Figs. 3.25-3.27) shows that the optimized design performed better, because it focused the blood cells better and has a wider range of operational flow rate (see appendix A.11).

Range of sheath flow rate for hydrodynamic focusing of cells:

Original design: 3.6×10^{-7} – 0.000144 kg/s

Optimized design: 3.6×10^{-7} – 0.000288kg/s

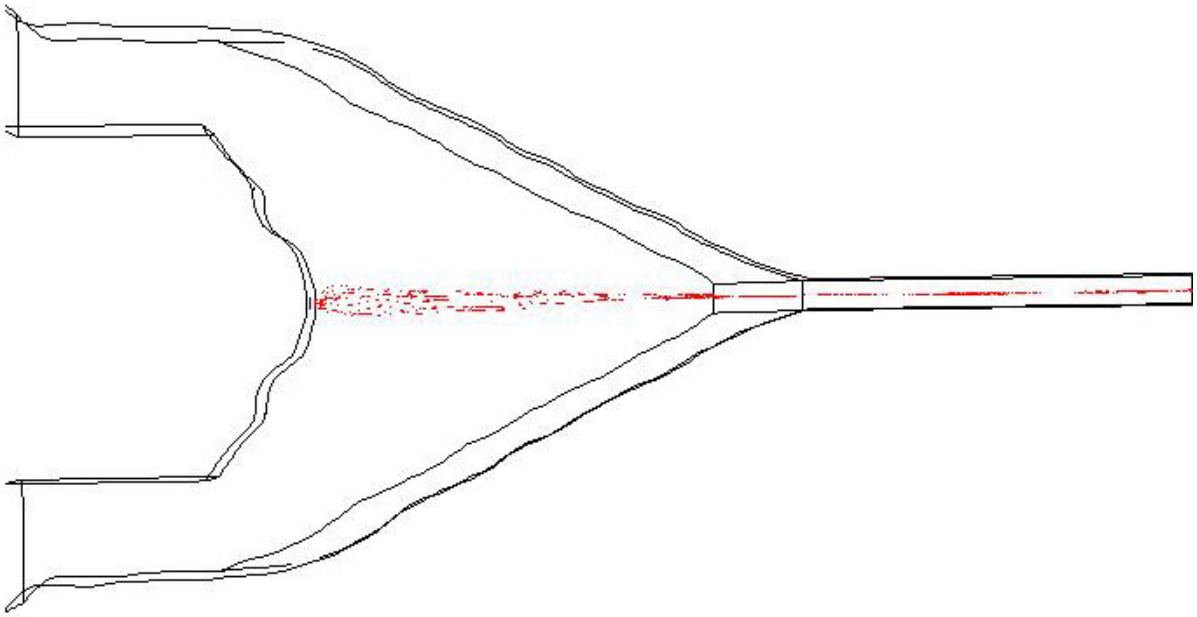

Figure 3.22: Trajectories of blood cells in optimized flow chamber (sheath flow = 3.6e-6 kg/s)

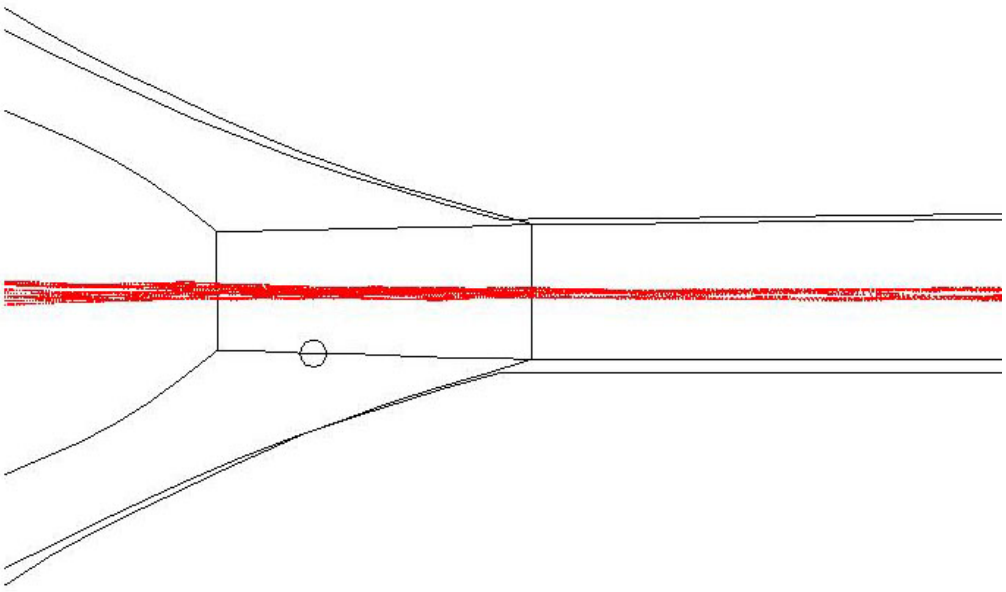

Figure 3.23: Magnified view of Fig. 3.22

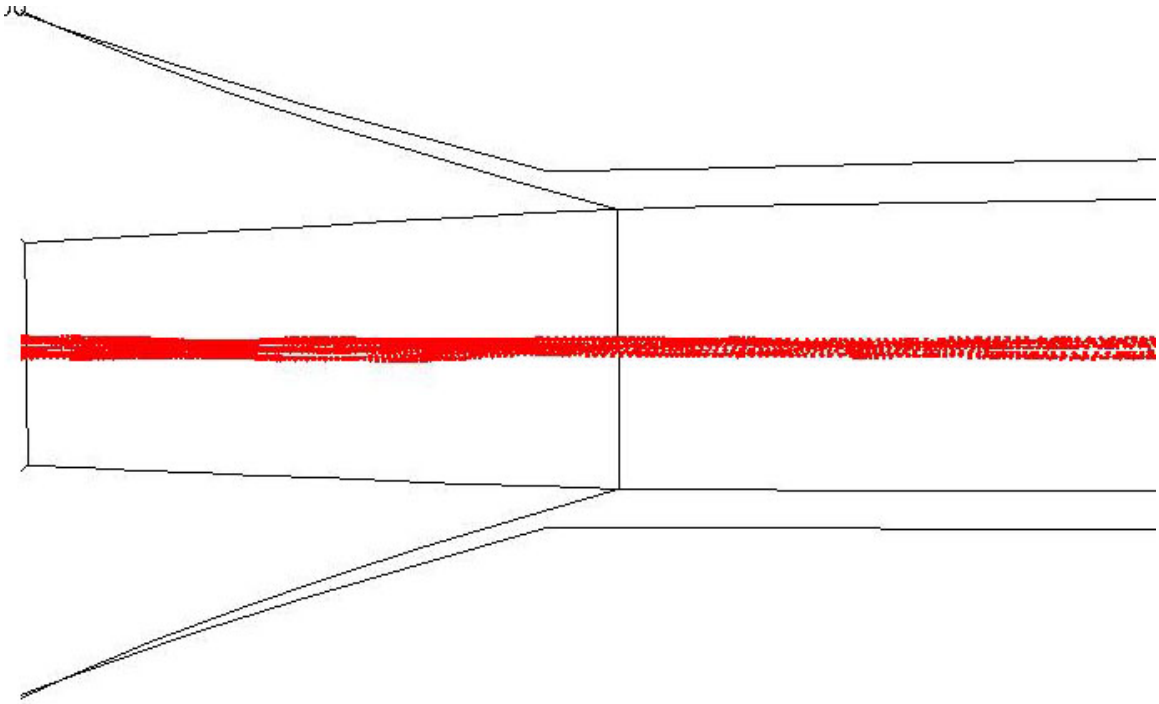

Figure 3.24: A further Magnification of fig 3.22

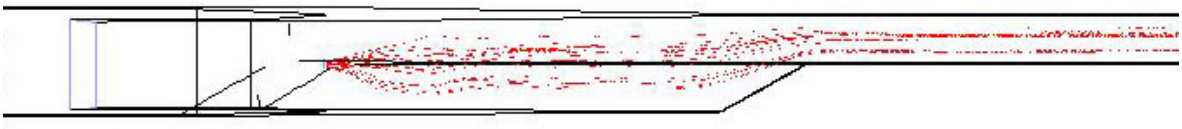

Figure 3.25: A side view of Fig. 3.22

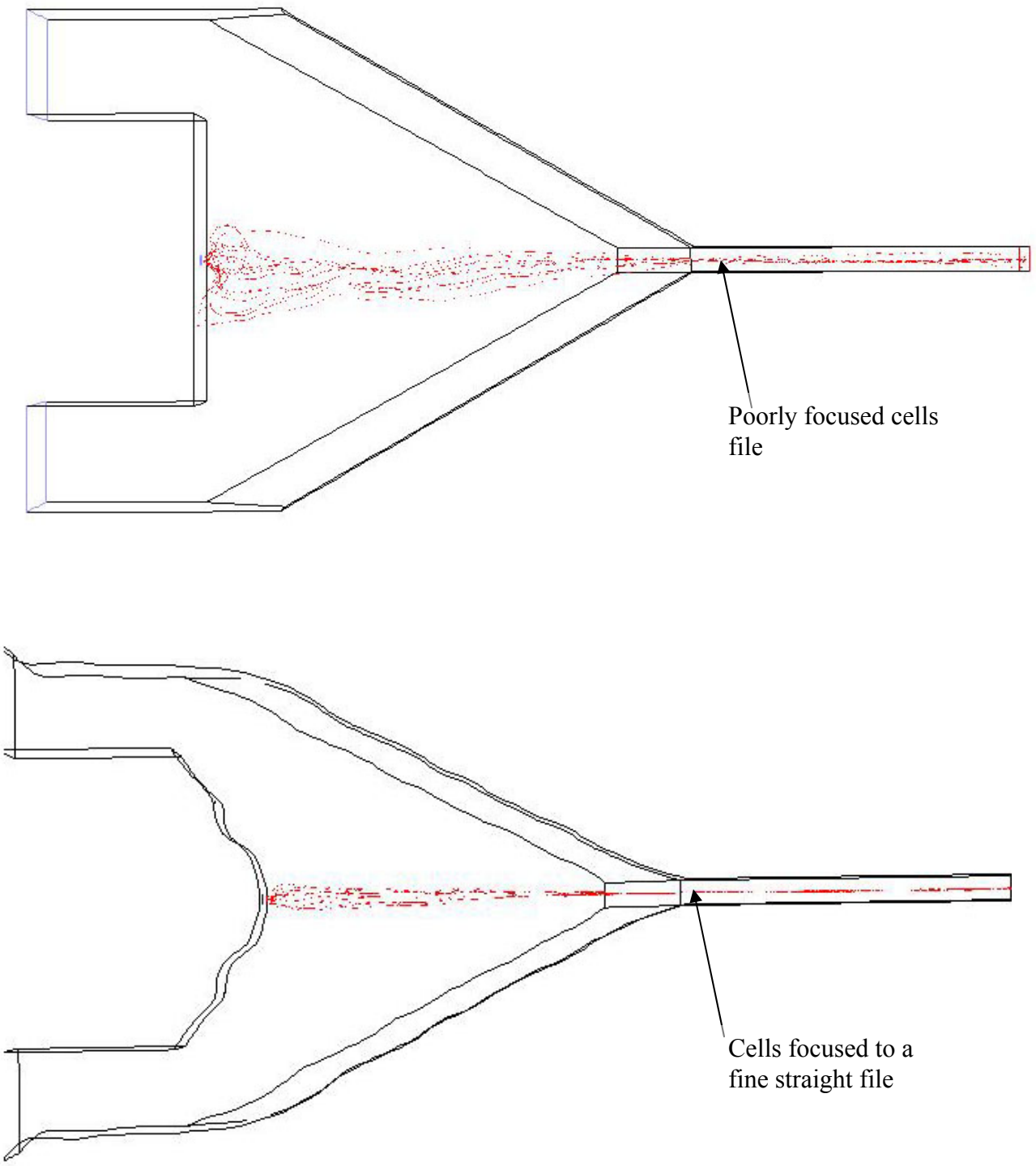

Figure 3.26: A side by side comparison of simulation results (sheath flow = 3.6e-6 kg/s)

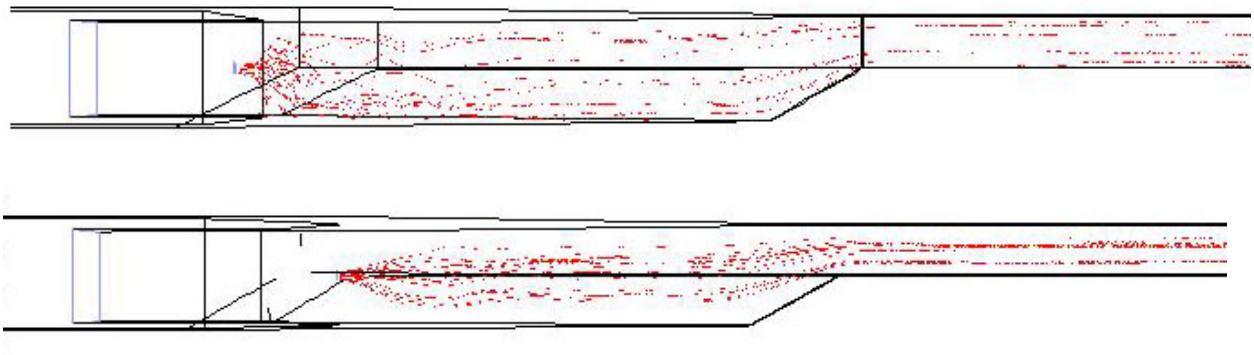

Figure 3.27: A side view of Fig. 3.26

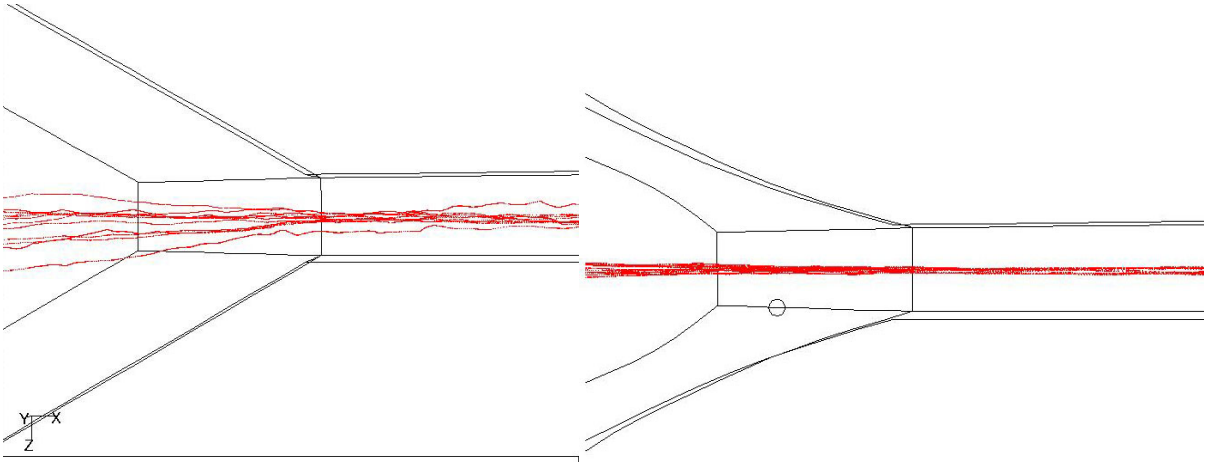

Figure 3.28: A magnified view of Fig. 3.26

In order to quantify the difference the two designs, a new quantity for measuring the effectiveness of the hydrodynamic focusing was defined as

$$f_{cyt} = \frac{d_{cell}}{d_{file}} \qquad 37$$

where d_{cell} = diameter (or average) diameter of cells, and d_{file} distance between two imaginary walls enveloping the the cell file in the flow cytometer exit pipe. (See Fig. 3.29)

For shape 2, the best value of f is gotten when $d_{file} = d_{cell}$ and this implies that

$$f_{cyt}\Big|_{Best} = \frac{d_{cell}}{d_{file}} = \frac{d_{cell}}{d_{cell}} = 1$$

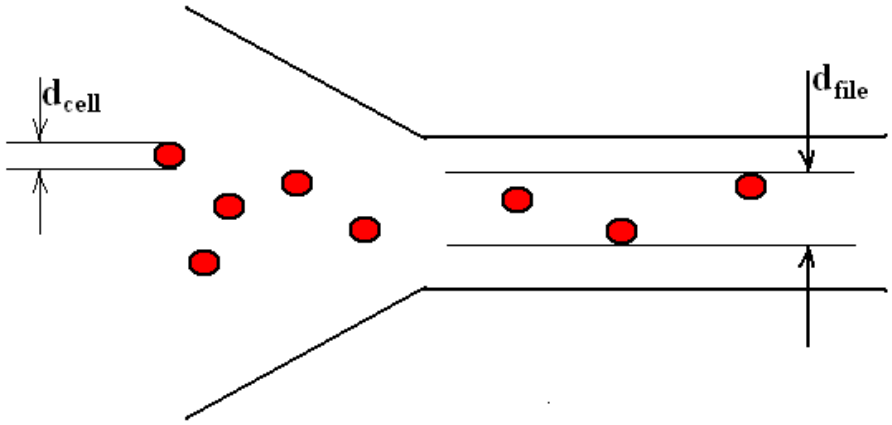

Figure 3.29: Measurements used to find f_{cyt}

and the worst value of f_{cyt} is obtained when $d_{file} = d$, where d is the distance between the exit pipe walls given in Table 3.3. Therefore, for shape 2 and using red blood cells as simulated

$$f_{cyt}\Big|_{Worst} = \frac{d_{cell}}{d} = \frac{7}{300} = 0.023$$

The values of f_{cyt} for both original design and optimized design of shape 2 were found and are listed in Table 3.4 below. It was observed that for sheath flow rate of 0.0000036 kg/s the optimize shape f_{cyt} improved by 323%. The average increase in f_{cyt} obtained by using the optimized design was 100%. The f_{cyt} of the flow cytometer was obtained by considering the whole exit pipe. However, it was observed that there very high focusing at some local position along the exit pipe for both designs. The optimized design performed better when the results were inspected visually and when the focusing effect was quantified.

Table 3.4: f_{cyt} calculated for both designs at different flow rates

Shape 2 (Original design)		
Sheath flow (kg/s)	dfile	f
0.00000036	195.349	0.036
0.0000036	181.395	0.039
0.000018	178.571	0.039
0.000036	97.674	0.072
0.000072	144.828	0.048
0.000144	77.586	0.090
0.000216	124.138	0.056
0.000288	189.474	0.037
0.00036	168.421	0.042
0.000432	165.517	0.042
0.000504	93.103	0.075
0.000576	237.931	0.029

Shape 2 (Optimized design)			
Sheath flow (kg/s)	dfile	f	% Δf
0.00000036	72.857	0.096	168.1259
0.0000036	42.857	0.163	323.2558
0.000018	43.902	0.159	306.746
0.000036	42.857	0.163	127.907
0.000072	90.000	0.078	60.91954
0.000144	105.000	0.067	-26.1084
0.000216	100.000	0.070	24.13793
0.000288	57.143	0.123	231.5789
0.00036	164.286	0.043	2.517162
0.000432	190.244	0.037	-12.9973
0.000504	182.927	0.038	-49.1034
0.000576	160.976	0.043	47.80564
		Average % Δf	100.3987

3.6 Summary

CFD was successfully used to simulate the performance of a flow cytometer. The analysis of the result is very flexible compared to using the microscope to observe an experiment, because the computer simulation can be used to view the flow region at any point and from any angle. An optimized design was developed. The optimized design focuses blood cells better and has a wider operational sheath flow range compared to the original design.

The conclusions drawn from this chapter and the preceding chapters will be discussed in the next chapter.

4. SUMMARY AND CONCLUSIONS

The results of this work are summarized as follows:

(i.) A new fuel cell flow field was designed (see Fig. 2.25) which has high mixing effect on the gas flow through the channel, so the performance of the fuel cell is enhanced. The stepped delivery path was designed to ensure that the pressures along all the sub-turpentine channels are equal, so that condensed water is easily flushed out of the channel. Shimpilee and coworkers [19] experimental study of the effect of the channel path length, and their work revealed that channels with small path lengths performs better than channels with long path lengths, but they did not explain the basis behind the effect, neither did they specify how short the path lengths should be. However, their finding is consistent with the new design, or in other words does not contradict the new design. The new flow field design was developed after carefully studying the performance characteristics of a PEM FC flow channel, and the design includes a specification of the best path length.

(ii.) Maharudrayya and coworkers [22] found that the high pressure drop across the serpentine flow field was due to the channel sharp turns, so they attempted to reduce the pressure drop by making the turns radial. Contrary to their work, it was found in this research that the sharp turns are indeed useful. The sharp turns causes mixing flow to develop in the flow and the mixing flow mixes the gas flow and allows Oxygen to easily reach the electrodes and as such prevent the condensation of water by eliminating local concentration of water vapor. Therefore, the high pressure drop across the serpentine flow field is useful, and experiment showed that the new design actually performed better. Specifically, for a fixed operational voltage of 0.6 volts, the current increase observed was 340%. Similarly, for a fixed operational current of 0.1 Amps, the voltage increase observed was 24%. (see Fig.

2.33) Please note that the increases observed and listed above are not efficiencies, and are due to increased chemical activity due to the improved design.

(iii.) A new model for the transport of protons in PEM based on mass conservation was developed. At zero current, the new model predicts diffusivity of protons as zero, which is true because there is no loss of electrons by hydrogen and membrane is impervious to hydrogen gas. Therefore, the new model is more preferable. In addition, Arrhenius equation was not used because any change in the rate of reaction will automatically show up in the flow rate of the electrons generated by the reaction. The mass flow rate equation provided in eqn. 11 is preferable because most of the time, the diffusivity coefficient is used to find mass flow rate. Then, having the mass flow rate equation makes the diffusivity coefficient equation unnecessary, if knowledge of mass flow rate is the main interest. In eqn. 11, $M_H > M_e$, so the mass flow rate of the electrons is negligibly low, so it is subtle to treat the current as a function of mass flow rate. In fact, the mass flow rate of the hydrogen can be estimated as the mass flow rate of protons, which is given by

$$\dot{m}_H = \frac{I \cdot \left(M_{H^+} + M_e\right)}{q_e} \approx \left(\frac{I \cdot \left(M_{H^+}\right)}{q_e} = \dot{m}_{H^+} \right)$$

An experiment performed to measure the mass flow rate or diffusivity of protons will create room for error, since the typical PEM fuel cell setup will be difficult to use for such an experiment.

(iv.) Analysis of fuel cell reactions equations showed that the use of equal electrodes area and thickness has the effect of reducing the efficiency of a fuel cell. This is true because equal electrodes area and thickness, causes excess or insufficient supply of oxidizer at the cathode. For example, hydrogen protons recombine with electrons to form hydrogen gas due to insufficient supply of oxidizer (see eqn. 33). The hydrogen gas formed at the cathode

flows away, burns up and contributes to the waste heat of the fuel cell. The virtual efficiencies obtained for the equal area electrodes in the theoretical analysis were compared to values practically obtained from fuel cells, and it was found that the virtual efficiency holds as the limit of efficiency that can be reached. The efficiency of a fuel cell can be increased by incorporating it in a hybrid with a thermal engine. In such hybrids, the thermal engine runs on the waste heat of the fuel cell and generates additional useful power. Designing the active electrode area ratio (see Fig. 2.41) to match the stoichiometric reaction equations (eqns. 28a and 28b) has effect on the performance of the fuel cell. AFC and PAFC benefits more from this modification, because their electrolytes are in liquid form and ions can easily move in more than one direction, but PEM FC cell does not benefit from such a modification because of the thin membrane whose nano pores mainly allows the diffusion of protons in the direction across the membrane. Experiments revealed that the electrode area ratio affects the efficiency of PEM fuel cells and adjustment of the area ratio can be used to obtain higher efficiencies in PEM fuel cells operating at low current densities, i.e. low electrical load.

(v.) A Computational Fluid Dynamics (CFD) program was used to simulate the performance of a high performance flow cytometer, which was designed by Ren Yang and coworkers. The red blood cells were modeled as oblate shaped particles with a shape factor of 5. The simulation was performed by injecting red blood cells and plasma through the sample inlet, while water was pumped in through the sheath flow inlet. It was observed from the simulation results that the hydrodynamic focusing of blood cells increases with increase in the sheath flow rate and later gets distorted at higher flow rates, and it was also observed that bigger cytometer exit pipe diameter requires higher sheath flow rates for hydrodynamic focusing of blood cells. The flow rate range that will entrain the blood cells was obtained

from the simulation result. Plots of the tracks of blood cells, and animation of the performance of the flow cytometer were obtained from the simulation result. The simulation results were compared to experimental results and were used to optimize the flow cytometer design. Simulations carried out with the optimized model showed improved performance of the flow cytometer. To be quantitative, the optimized design increased the focusing effect of the flow cytometer design by 300% for sheath flow rate of 0.000018 kg/s.

REFERENCES

1. Yang, Daniel and Wanjun Wang. *Microfabrication and test of a three-dimensional focusing unit for flow cytometry application.* Sensors and Actuators, A 118(2005).

2. Yang, R. *Ultra-violet Lithography of Thick Photoresist for the Applications in BIOMEMS and Micro-optics.* Diss. Louisiana State University, 2006.

3. R. S. Yeo, and J. McBreen, *J. Electrochemical Society*, 126 ~10(1979): p.1682-1687.

4. Cook, B. *An introduction to fuel cells and hydrogen technology*. 2001. August 8, 2007 < www.fuelcellstore.com/products/heliocentris/INTRO.pdf>.

5. Blomen and Micheal Mugerwa. *Fuel Cell Systems*. New York: Plenum, 1993

6. Garrison, Earnest. *Fuel Cell Basics.* August 8, 2007 < http://www.iit.edu/~smart/garrear/fuelcells.htm>.

7. G Hoogers, *Fuel Cell Technology Handbook.* New York: CRC Press 2003: p.4.10-4.15.

8. R. W. Baker, *Membrane Technology and Applications*. New York: McGraw-Hill, 2000: p. 15-81, 373-402.

9. A. Eisenberg and H. L. Yeager, Perfluorinated Ionomer Membranes. Washington DC: American Chemical Society 1982

10. P. Colomban, *Proton Conductors: Solids, Membranes and Gels: Materials and Devices*. Cambridge: Cambridge University Press 1992

11. X. Din and E. E. Michaelis, *AIChE Journal*, 44 ~1(1998): p. 35-47.

12. DuPont, *Nafion PFSA Membranes Product Information*, <http://www.dupont.com/fuelcells/pdf/dfc101.pdf> (11/7/2006).

13. DuPont, *Nafion PFSA Membranes Product Information*, <http://www.dupont.com/fuelcells/pdf/dfc201.pdf> (11/7/2006).

14. Rolf Sander, *Compilation of Henry's Law Constants for Inorganic and Organic Species of Potential Importance in Environmental Chemistry*, http://www.mpch-mainz.mpg.de/~sander/res/henry-pdf.zip (11/7/2006).

15. The International Association for the Properties of Water and Steam, *Guideline on the Henry's Constant and Vapor-Liquid Distribution Constant for Gases in H_2O and D_2O at High Temperatures.* IAPWS 2004, Kyoto, Japan <http://www.iapws.org/relguide/HenGuide.pdf> 12/30/2007.

16. C. L. Young, Ed., *IUPAC Solubility Data Seires, Vol. 5/6, Hydrogen and Deuterium*. Pergamon Press, Oxford, England, 1981.

17. Nguyen, Berning and Ned Djilali. *Computational model of a PEM fuel cell with serpentine gas flow channels.* JPS 130 (2004): p. 149-157.

18. Williams, Kunz and James M. Fenton. *Influence of convection through gas-diffusion layers on limiting current in PEM FCs using a serpentine flow field*. JES 150(10) (2004): p. A1617-A1627.

19. Glandt, Shimpalee, Lee and John W. Van Zee. Modeling the effect of flow field design. August 8, 2007 <www.che.sc.edu/centers/PEMFC/vanzee_hp/MODELING THE EFFECT OF FLOW FIELD DESIGN ON.pdf >.

20. Cha, O'Hayre, Lee, Saito and Fritz B. Prinz. *Geometric scale effect of flow channels on performance of fuel cells.* JES 151(11) (2004): p. A1856-A1864.

21. Karvonen, Hottinen, Saarinen, and Olli Himanen. *Modeling of flow field in polymer electrolyte membrane fuel cell.* JPS 161 (2006) 876-884.

22. Maharudrayya, Jayanti and A. P. Deshpanda. *Pressure losses in laminar flow through serpentine channels in fuel cell stacks.* JPS 138 (2004): p. 1-13.

23. Potter and David C. Wiggert. *Mechanics of Fluids.* Pacific Grove: Brooks/Cole, 2002.

24. G Hoogers, *Fuel Cell Technology Handbook.* New York: CRC Press 2003: p. 1.4.

25. US DOE, *Comparison of Fuel Cell Technologies* <http://www1.eere.energy.gov/hydrogenandfuelcells/fuelcells/pdfs/fc_comparison_chart.pdf> 08/21/2007.

26. Blomen and Micheal Mugerwa. *Fuel Cell Systems*. New York: Plenum, 1993 pg 70.

27. G Hoogers, *Fuel Cell Technology Handbook.* New York: CRC Press 2003: p. 1.4.

28. Watson, J. *Introduction to Flow Cytometry*, New York: Camridge University Press, 1991: p. 1-17.

29. *Flow Cytometry of Microrganisms,* <http://pcfcij.dbs.aber.ac.uk/thesis/tchap1.html> 08/21/2007.

30. *History of Flow Cytometry,* <http://www.unc.edu/~mcgibbon/History_of_FC.html> 08/21/2007.

31. Ormerod, M. G. *Flow Cytometry: A practical Approach*, New York: Oxford University Press, 1990: p. 1-8.

32. S. Hernández and A. Fontán. *Practical Applications of Design Optimization.* WIT Press, 2002.

33. Chung, T. J. *Computational Fluid Dynamics.* Cambridge: Cambridge University Press, 2002.

APPENDIX A.1: K_{HENRY} FROM REFERENCE 14

Units conversion and simplification details of K_{Henry}

$$K_{Henry} = K_{Henry}^{\theta} \times \exp\left(\frac{-\Delta_{so\ln} H}{R}\left(\frac{1}{T} - \frac{1}{T^{\theta}}\right)\right)$$

$$\frac{-d\ln(K_{Henry})}{d(1/T)} = \frac{\Delta_{so\ln} H}{R} = 500\,\mathrm{K}$$

$$K_{Henry}^{\theta} = 7.8\times10^{-4}\left[\frac{\mathrm{mol}/dm^3}{atm}\right] = 7.8\times10^{-1}\left[\frac{\mathrm{mol}/m^3}{atm}\right]$$

$$K_{Henry} = 7.8\times10^{-1}\times\exp\left(-500\left(\frac{1}{T} - \frac{1}{298}\right)\right) = 4.176155\times\exp\left(-\frac{500}{T}\right)$$

APPENDIX A.2: FUEL CELL CURRENT AND TEMPERATURE RELATION

Theoretical fuel cell equations variation with temperature used to derive part of Appendix A.3 below

$$\Delta G = \Delta H - T\Delta S = 0.0002T^2 + 9.3169T + 5.574T(Ln(T)) - 242217.8 \quad \text{[KJ]}$$

$$E = \frac{-\Delta G}{nF} = \frac{0.0002T^2 + 9.3169T + 5.574T(Ln(T)) - 242217.8}{2*96485}$$

$$I = \frac{1}{R}E = C\frac{1}{R}\cdot\frac{0.0002T^2 + 9.3169T + 5.574T(Ln(T)) - 242217.8}{2*96485}$$

APPENDIX A.3: DATA TABLES AND PLOTS OF DIFFUSIVITY

Table A.1: D, T values for $V^{\theta} = 1.0199,\ i^{\theta} = 0.03981 \Rightarrow R = V/i = 25.6192\,\Omega m^2 = \text{constant}$

T	E	i	Dnew	Dyeo
298	1.019868	0.03981	6.61E-11	6.62E-11
300	1.019453	0.039794	6.53E-11	7.01E-11
305	1.018414	0.039753	6.35E-11	8.09E-11
310	1.017373	0.039713	6.18E-11	9.28E-11
315	1.01633	0.039672	6.01E-11	1.06E-10
320	1.015285	0.039631	5.86E-11	1.21E-10
325	1.014238	0.03959	5.72E-11	1.37E-10
330	1.013189	0.039549	5.58E-11	1.54E-10
335	1.012138	0.039508	5.45E-11	1.74E-10
340	1.011085	0.039467	5.32E-11	1.95E-10
345	1.010031	0.039426	5.21E-11	2.17E-10
350	1.008974	0.039385	5.09E-11	2.42E-10
355	1.007916	0.039343	4.99E-11	2.69E-10
360	1.006856	0.039302	4.89E-11	2.98E-10
365	1.005794	0.039261	4.79E-11	3.29E-10
370	1.004731	0.039219	4.70E-11	3.62E-10
375	1.003665	0.039177	4.61E-11	3.98E-10
380	1.002598	0.039136	4.52E-11	4.36E-10
385	1.00153	0.039094	4.44E-11	4.76E-10
390	1.000459	0.039052	4.36E-11	5.19E-10
395	0.999388	0.03901	4.29E-11	5.65E-10
398	0.998744	0.038985	4.25E-11	5.94E-10

Table A.2: D, T values for $V^{\theta} = 0.96, i^{\theta} = 17 \Rightarrow R = V/i = 0.05647\,\Omega m^2 = \text{constant}$

T	E	i	Dnew	Dyeo
298	0.96	17	2.82E-08	6.62E-11
300	0.959609	16.99308	2.79E-08	7.01E-11
305	0.958632	16.97577	2.71E-08	8.09E-11
310	0.957652	16.95841	2.64E-08	9.28E-11
315	0.95667	16.94103	2.57E-08	1.06E-10
320	0.955686	16.92361	2.50E-08	1.21E-10
325	0.954701	16.90616	2.44E-08	1.37E-10
330	0.953713	16.88867	2.38E-08	1.54E-10
335	0.952724	16.87116	2.33E-08	1.74E-10
340	0.951733	16.85361	2.27E-08	1.95E-10

Table A.2 continued

T	E	i	Dnew	Dyeo
345	0.95074	16.83603	2.22E-08	2.17E-10
350	0.949746	16.81842	2.18E-08	2.42E-10
355	0.94875	16.80078	2.13E-08	2.69E-10
360	0.947752	16.78311	2.09E-08	2.98E-10
365	0.946753	16.76541	2.05E-08	3.29E-10
370	0.945751	16.74768	2.01E-08	3.62E-10
375	0.944749	16.72992	1.97E-08	3.98E-10
380	0.943744	16.71214	1.93E-08	4.36E-10
385	0.942738	16.69433	1.90E-08	4.76E-10
390	0.941731	16.67649	1.86E-08	5.19E-10
395	0.940722	16.65862	1.83E-08	5.65E-10
398	0.940116	16.64789	1.81E-08	5.94E-10

Table A.3: D, T values for $V^{\theta}=0.7, \mathrm{i}^{\theta}=3000 \Rightarrow R=V/i=2.333\times10^{-4}\ \Omega\mathrm{m}^2=\text{constant}$

T	E	i	Dnew	Dyeo
298	0.7	3000	4.98E-06	6.62E-11
300	0.699715	2998.78	4.92E-06	7.01E-11
305	0.699002	2995.723	4.78E-06	8.09E-11
310	0.698288	2992.661	4.66E-06	9.28E-11
315	0.697572	2989.593	4.53E-06	1.06E-10
320	0.696854	2986.519	4.42E-06	1.21E-10
325	0.696136	2983.439	4.31E-06	1.37E-10
330	0.695416	2980.354	4.20E-06	1.54E-10
335	0.694695	2977.263	4.11E-06	1.74E-10
340	0.693972	2974.166	4.01E-06	1.95E-10
345	0.693248	2971.064	3.92E-06	2.17E-10
350	0.692523	2967.956	3.84E-06	2.42E-10
355	0.691797	2964.843	3.76E-06	2.69E-10
360	0.691069	2961.725	3.68E-06	2.98E-10
365	0.69034	2958.602	3.61E-06	3.29E-10
370	0.68961	2955.473	3.54E-06	3.62E-10
375	0.688879	2952.34	3.47E-06	3.98E-10
380	0.688147	2949.201	3.41E-06	4.36E-10
385	0.687413	2946.058	3.35E-06	4.76E-10
390	0.686679	2942.909	3.29E-06	5.19E-10
395	0.685943	2939.756	3.23E-06	5.65E-10
398	0.685501	2937.862	3.20E-06	5.94E-10

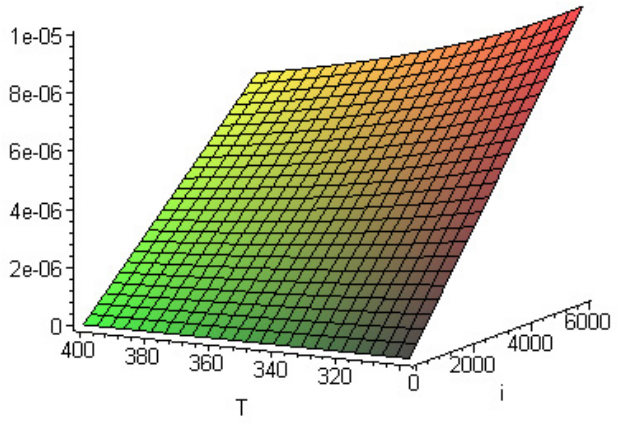

Figure A.1: 3D plot of protons diffusivity in PEM using eqn. 26 (view I)

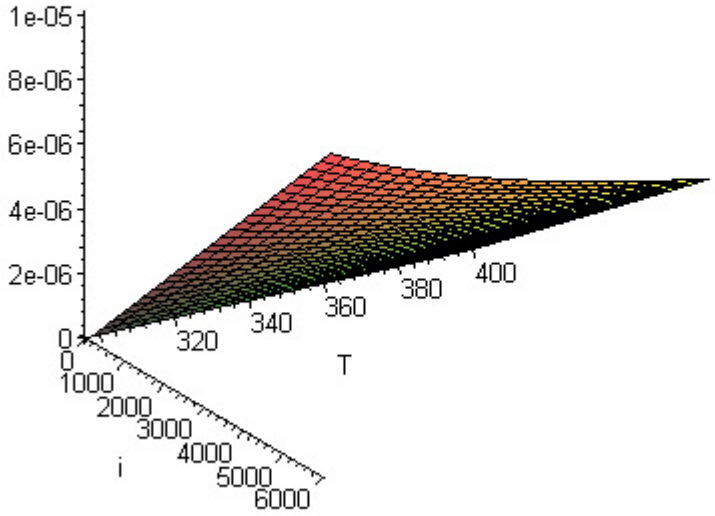

Figure A.2: 3D plot of protons diffusivity in PEM using eqn. 26 (view II)

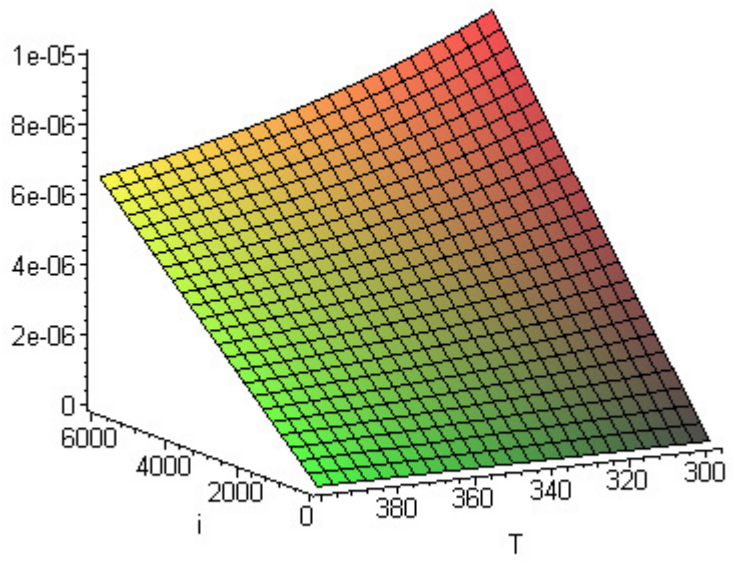

Figure A.3: 3D plot of protons diffusivity in PEM using eqn. 26 (view III)

APPENDIX A.4: DETAILS OF FABRICATED FUEL CELL CHANNELS

See next two pages for printout of solid works drawing details of the fabricated channels used for the flow channel experiments. (Figs. A.4 and A.5)

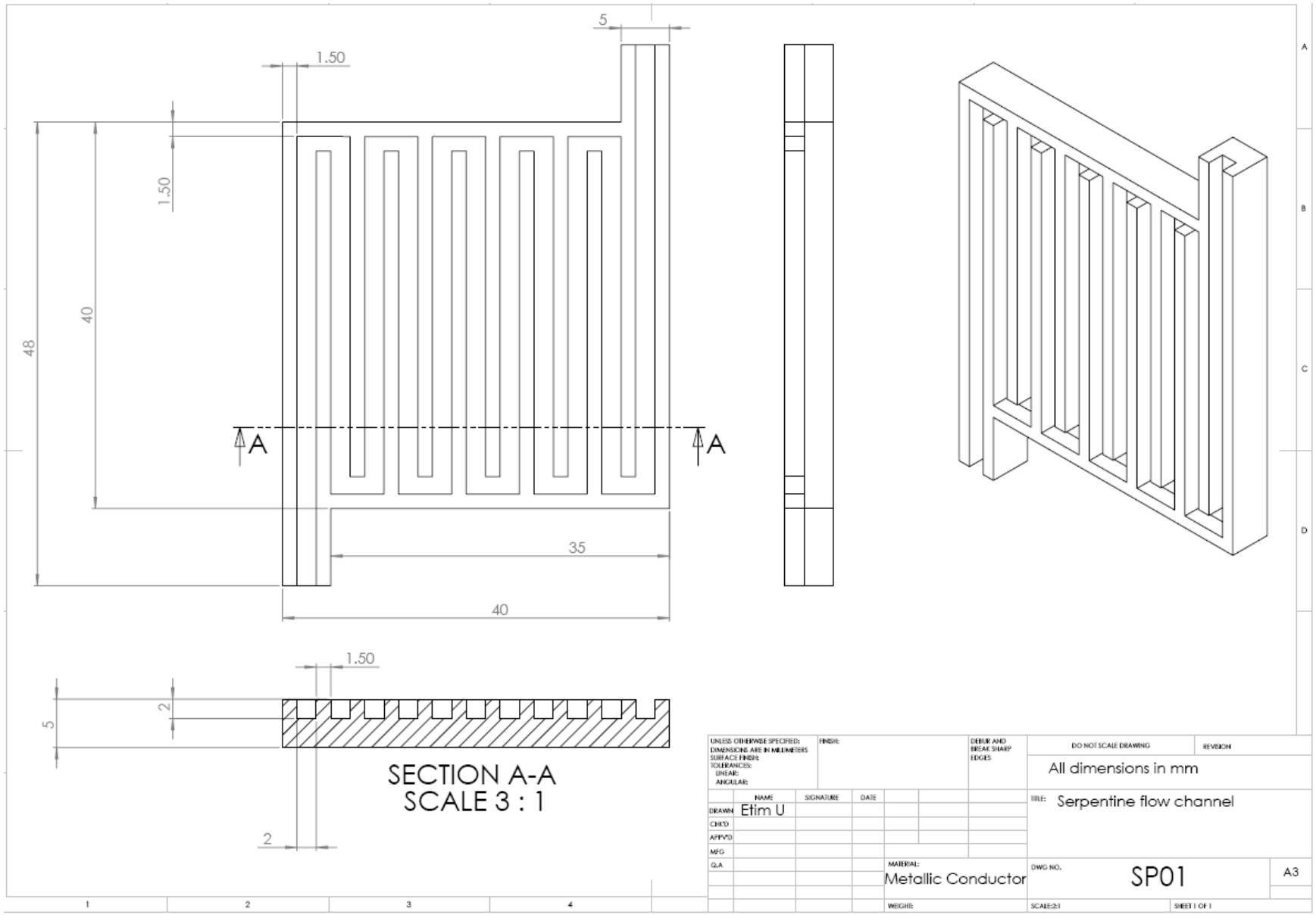

Figure A.4: Drawing details of fabricated serpentine flow channel

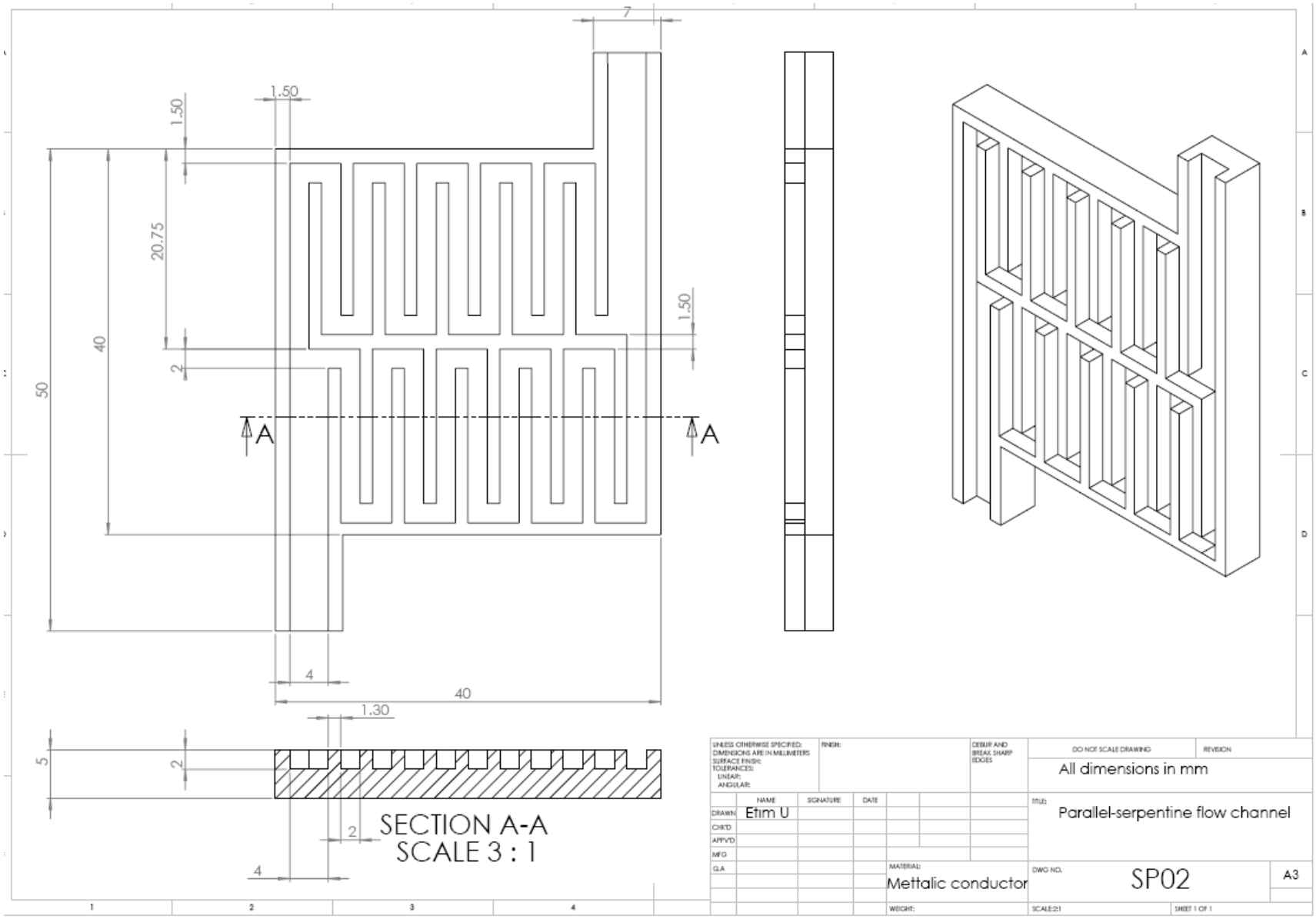

Figure A.5: Drawing details of fabricated parallel serpentine flow channel

APPENDIX A.5: FLOW CHANNEL EXPERIMENT DATA

Table A.4: Flow channel experimental readings

Parallel-Serpentine (New) design		
I(Amps)	V(Volts)	err(Volts)
0.000	0.760	0.0061
0.003	0.750	0.0060
0.007	0.750	0.0060
0.011	0.740	0.0059
0.067	0.700	0.0056
0.120	0.660	0.0053
0.191	0.620	0.0050
0.368	0.510	0.0041

Serpentine design		
I(Amps)	V(Volts)	err(Volts)
0.000	0.700	0.0056
0.003	0.680	0.0054
0.006	0.660	0.0053
0.007	0.630	0.0050
0.056	0.580	0.0046
0.081	0.550	0.0044
0.145	0.500	0.0040
0.238	0.420	0.0034

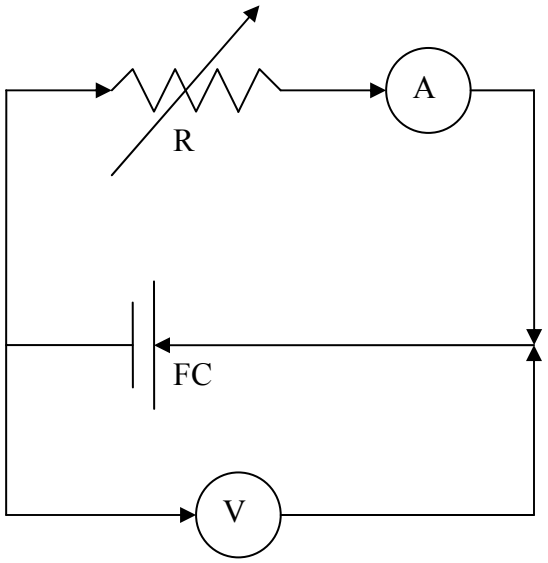

Figure A.6: Experimental setup

APPENDIX A.6: ELECTRODE AREA EXPERIMENT DATA

Table A.5: H2-O2 PEM FC electrode-area-ratio experiment readings

H2-O2		
Aa:Ac	1:1	
I(Amps)	V(Volts)	err(Volts)
0.000	0.837	0.0088
0.003	0.813	0.0087
0.007	0.803	0.0086
0.015	0.786	0.0098
0.070	0.720	0.0058
0.126	0.680	0.0055
0.200	0.627	0.0068
0.361	0.519	0.0126

H2-O2		
Aa:Ac	1:0.5	
I(Amps)	V(Volts)	err(Volts)
0.000	0.925	0.0377
0.003	0.833	0.0117
0.007	0.805	0.0183
0.014	0.778	0.0155
0.067	0.693	0.0213
0.120	0.623	0.0324
0.181	0.565	0.0425
0.280	0.410	0.0463

Table A.6: H2-Air PEM FC electrode-area-ratio experiment readings

H2-Air		
Aa:Ac	0.42:0.42	
I(Amps)	V(Volts)	err(Volts)
0.000	0.780	0.0118
0.003	0.760	0.0117
0.007	0.745	0.0078
0.014	0.723	0.0082
0.061	0.623	0.0076
0.105	0.553	0.0073
0.156	0.477	0.0069
0.250	0.320	0.0026

H2-Air		
Aa:Ac	0.42:1	
I(Amps)	V	Err(Volts)
0.000	0.847	0.0089
0.003	0.777	0.0085
0.007	0.747	0.0083
0.014	0.717	0.0081
0.063	0.623	0.0076
0.106	0.553	0.0073
0.157	0.483	0.0069
0.254	0.330	0.0103

APPENDIX A.7: ADDITIONAL ELECTRODE AREA EXPERIMENTS DATA

Table A.7: H2-O2 PEM FC electrode-area-ratio experiment readings

H2-O2		
Aa:Ac	1:0.75	
I(Amps)	V(Volts)	err(Volts)
0.000	0.857	0.0134
0.003	0.833	0.0088
0.007	0.818	0.0123
0.015	0.793	0.0086
0.070	0.723	0.0082
0.127	0.667	0.0079
0.200	0.610	0.0049
0.370	0.490	0.0039

H2-O2		
Aa:Ac	1:0.25	
I(Amps)	V(Volts)	err(Volts)
0.000	0.783	0.0165
0.003	0.760	0.0117
0.007	0.747	0.0164
0.014	0.723	0.0129
0.061	0.627	0.0161
0.105	0.550	0.0179
0.150	0.460	0.0177
0.238	0.310	0.0202

Table A.8:H2-Air PEM FC electrode-area-ratio experiment readings

H2-Air		
Aa:Ac	0.42:0.6	
I(Amps)	V(Volts)	err(Volts)
0.000	0.803	0.0132
0.003	0.773	0.0085
0.007	0.763	0.0084
0.015	0.740	0.0116
0.062	0.645	0.0072
0.109	0.573	0.0074
0.163	0.500	0.0040
0.265	0.347	0.0064

H2-Air		
Aa:Ac	0.42:0.25	
I(Amps)	V(Volts)	err(Volts
0	0.746667	0.016402
0.003	0.73	0.020835
0.006	0.713333	0.021585
0.013	0.69	0.020748
0.056	0.576667	0.025585
0.095	0.493333	0.030804
0.14	0.406667	0.035269
0.2	0.25	0.017436

APPENDIX A.8: PLOTS OF ELECTRODE AREA EXPERIMENTS RESULTS

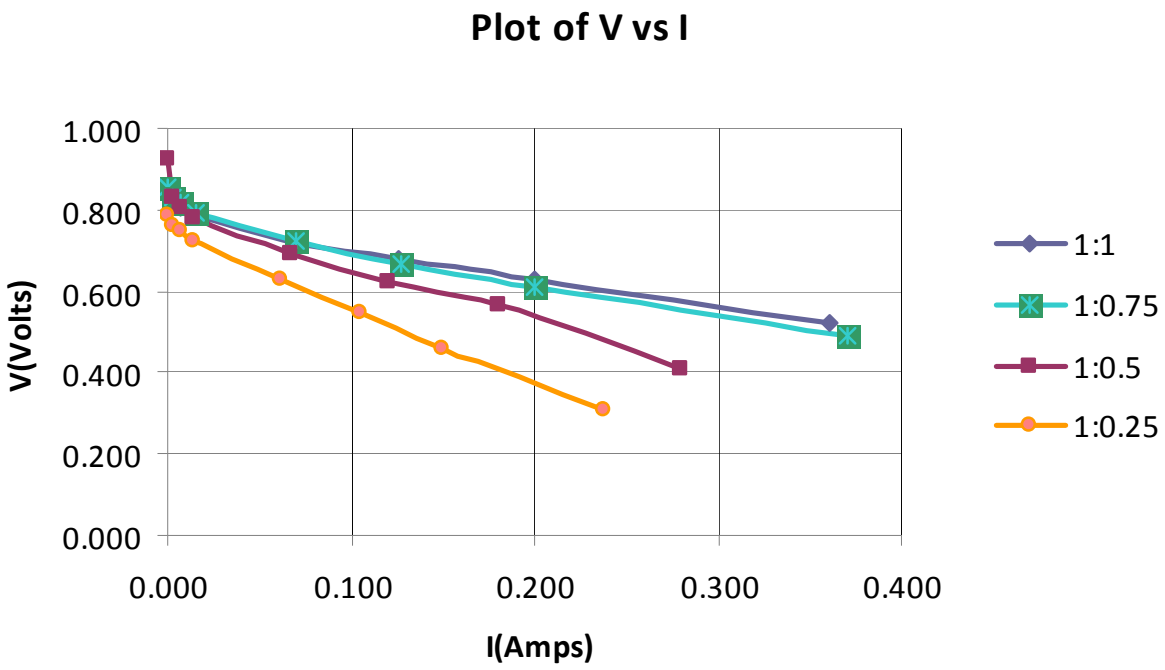

Figure A.7a: Plot of V vs. I for H2-O2 PEM FC for various electrode area ratios

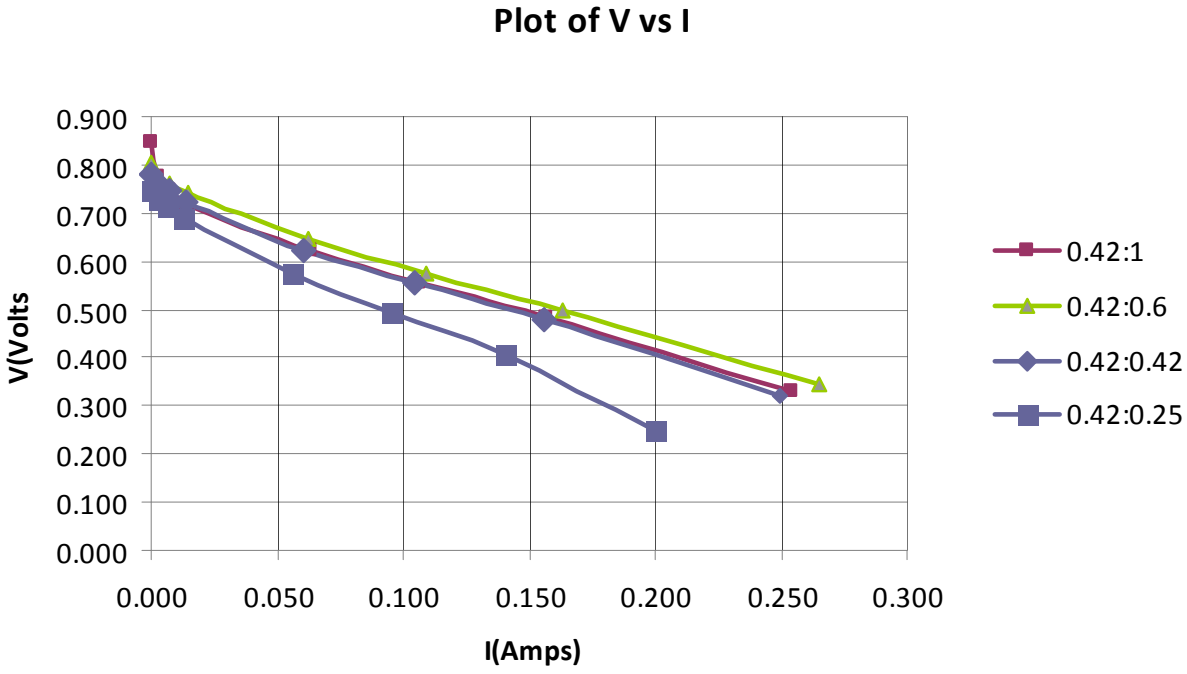

Figure A.8a: Plot of V vs. I for H2-Air PEM FC for various electrode area ratios

APPENDIX A.9: GRID GENERATION SCRIPTS AND PROCEDURES

The information in this section provides additional simulation information for the flow cytometry simulation. It is referred to in section 3.3. In addition, the information in this section is to ease the repeatability of the flow cytometry part of this work, because of the high degree of complexity involved in modeling and simulating the micro-size flow cell, multiphase flow of blood plasma and water, and blood cells injection. Knowledge of flow cytometry, section A.12, Gambit and Fluent CFD code will help comprehend this section. However, it is required that the whole of this work be repeatable and this section clarifies the obstacles an investigator may face. 'Shape 2m.jou' is the file name of the delimited ANSI text containing the texts for generating the model and grid for the original flow cytometer design. And 'Shape 2.jou' is the name of the delimited ANSI text containing the texts for generating the model and grid for the optimized flow cytometer design. Each text line of 'Shape 2m.jou' and 'Shape 2.jou' is a command that can by typed directly into the command input window of Gambit or the whole files can be run by making Gambit read and run the program files. Details of grid generation procedure is given on page 112.

Shape 2m.jou

```
vertex create "1" coordinates 0 -0.75 4.7547
vertex create "2" coordinates 0 -0.75 1.2547
vertex create "3" coordinates 2 -0.75 1.2547
vertex create "4" coordinates 2 0.25 1.2547
vertex create "5" coordinates 2 0.25 4.7547
vertex create "6" coordinates 0 0.25 4.7547
vertex create "7" coordinates 0 0.25 1.2547
vertex create "8a" coordinates 2 -0.2 2.9547
vertex create "8b" coordinates 2 -0.2 3.0547
vertex create "8c" coordinates 2 -0.3 3.0547
vertex create "8d" coordinates 2 -0.3 2.9547
vertex create "9" coordinates 2 -0.75 4.7547
vertex create "10" coordinates 0 -0.75 0
vertex create "11" coordinates 0 0.25 0
vertex create "12" coordinates 0 0.25 6.0094
vertex create "13" coordinates 0 -0.75 6.0094
vertex create "14" coordinates 2 -0.75 6.0094
vertex create "15a" coordinates 3.032 0.25 6.0094
vertex create "15b" coordinates 3.032 -0.25 6.0094
vertex create "16" coordinates 7.9765 0.25 3.1547
vertex create "17" coordinates 7.9765 -0.25 3.1547
vertex create "18" coordinates 7.1105 -0.75 3.1547
vertex create "19" coordinates 7.1105 -0.75 2.8547
vertex create "20" coordinates 7.9765 -0.25 2.8547
vertex create "21" coordinates 7.9765 0.25 2.8547
vertex create "22a" coordinates 3.032 0.25 0
vertex create "22b" coordinates 3.032 -0.25 0
vertex create "23" coordinates 2 -0.75 0
vertex create "24" coordinates 11.9765 0.25 2.8547
vertex create "25" coordinates 11.9765 -0.25 2.8547
vertex create "26" coordinates 11.9765 -0.25 3.1547
vertex create "27" coordinates 11.9765 0.25 3.1547
vertex create "28" coordinates 0 -0.75 2.5047
vertex create "29" coordinates 0 -0.75 3.5047
vertex create "30" coordinates 0 0.25 3.5047
vertex create "31" coordinates 0.75 0.25 3.5047
vertex create "32" coordinates 0.75 0.25 2.5047
vertex create "33" coordinates 0.75 -0.75 2.5047
vertex create "34" coordinates 0.75 -0.75 3.5047
vertex create "36" coordinates 0 0.25 2.5047
edge create "10-2" straight "10" "2"
edge create "2-28" straight "2" "28"
edge create "28-29" straight "28" "29"
edge create "29-1" straight "29" "1"
edge create "1-13" straight "1" "13"
edge create "13-12" straight "13" "12"
edge create "12-6" straight "12" "6"
edge create "6-30" straight "6" "30"
edge create "30-36" straight "30" "36"
edge create "36-7" straight "36" "7"
edge create "7-11" straight "7" "11"
edge create "11-10" straight "11" "10"
edge create "7-2" straight "7" "2"
edge create "36-28" straight "28" "36"
edge create "30-29" straight "30" "29"
edge create "6-1" straight "6" "1"
edge create "10-23" straight "10" "23"
edge create "11-22a" straight "11" "22a"
edge create "2-3" straight "2" "3"
edge create "7-4" straight "7" "4"
edge create "36-32" straight "36" "32"
edge create "28-33" straight "28" "33"
```

```
edge create "29-34" straight "29" "34"
edge create "30-31" straight "30" "31"
edge create "6-5" straight "5" "6"
edge create "1-9" straight "1" "9"
edge create "12-15a" straight "12" "15a"
edge create "13-14" straight "13" "14"
edge create "22a-b" straight "22a" "22b"
edge create "22b-23" straight "22b" "23"
edge create "23-19" straight "19" "23"
edge create "19-20" straight "20" "19"
edge create "20-21" straight "20" "21"
edge create "22a-21" straight "21" "22a"
edge create "22b-20" straight "20" "22b"
edge create "21-24" straight "21" "24"
edge create "20-25" straight "20" "25"
edge create "24-25" straight "24" "25"
edge create "27-24" straight "24" "27"
edge create "25-26" straight "25" "26"
edge create "26-27" straight "26" "27"
edge create "27-16" straight "16" "27"
edge create "16-17" straight "16" "17"
edge create "16-15a" straight "15a" "16"
edge create "17-15b" straight "15b" "17"
edge create "15a-15b" straight "15a" "15b"
edge create "14-15b" straight "14" "15b"
edge create "14-18" straight "14" "18"
edge create "17-18" straight "17" "18"
edge create "18-19" straight "18" "19"
edge create "17-20" straight "17" "20"
edge create "16-21" straight "16" "21"
edge create "5-4" straight "4" "5"
edge create "4-3" straight "3" "4"
edge create "5-9" straight "5" "9"
edge create "3-9" straight "3" "9"
edge create "31-32" straight "31" "32"
edge create "33-34" straight "33" "34"
edge create "33-32" straight "32" "33"
edge create "31-34" straight "31" "34"
edge create "26-17" straight "26" "17"
edge create "8a-b" straight "8a" "8b"
edge create "8b-c" straight "8b" "8c"
edge create "8c-d" straight "8c" "8d"
edge create "8d-a" straight "8a" "8d"
face create "out" wireframe "24-25" "27-24" "25-26" "26-27" real
face create "L1" wireframe "20-25" "25-26" "26-17" "17-20" real
face create "R1" wireframe "20-21" "21-24" "20-25" "24-25" real
face create "T1" wireframe "21-24" "27-24" "27-16" "16-21" real
face create "RR1" wireframe "26-27" "27-16" "26-17" "16-17" real
face create "LL1" wireframe "17-20" "19-20" "17-18" "18-19" real
face create "R2" wireframe "22a-b" "20-21" "22a-21" "22b-20" real
face create "RR2" wireframe "22b-23" "22b-20" "23-19" "19-20" real
face create "L2" wireframe "16-17" "16-15a" "17-15b" "15a-15b" real
face create "LL2" wireframe "17-15b" "14-15b" "14-18" "17-18" real
face create "R3" wireframe "11-10" "10-23" "11-22a" "22a-b" "22b-23" real
face create "L3" wireframe "13-12" "12-15a" "13-14" "15a-15b" "14-15b" real
face create "T2" wireframe "11-22a" "22a-21" "16-21" "7-11" "7-4" "5-4" "6-5" \
  "12-6" "12-15a" "16-15a" real
face create "LL3" wireframe "18-19" "23-19" "10-23" "10-2" "2-3" "3-9" "1-9" \
  "1-13" "13-14" "14-18" real
face create "IN1" wireframe "10-2" "7-11" "11-10" "7-2" real
face create "Solid1" wireframe "7-2" "2-3" "7-4" "4-3" real
face create "Solid2" wireframe "5-4" "4-3" "5-9" "3-9" real
face create "Solid3" wireframe "6-5" "1-9" "5-9" "6-1" real
face create "IN2" wireframe "1-13" "13-12" "12-6" "6-1" real
volume create "MixedVolume" stitch "out" "L1" "R1" "T1" "RR1" "LL1" "R2" \
```

```
  "RR2" "L2" "LL2" "R3" "L3" "T2" "LL3" "IN1" "Solid1" "Solid2" "Solid3" \
  "IN2" real
volume create "Sampleinlet" wireframe "30-36" "36-28" "30-29" "36-32" "28-33" \
  "29-34" "30-31" "31-32" "33-34" "33-32" "31-34" "28-29"
edge delete "2-28" "29-1" "6-30" "36-7" lowertopology
volume delete "Sampleinlet" lowertopology
face create "Sample inlet" wireframe "8a-b" "8b-c" "8c-d" "8d-a" real
face split "Solid2" connected face "Sample inlet"
volume mesh "MixedVolume" tetrahedral size 0.11
volume smooth "MixedVolume" fixed lwlaplacian
physics create ctype "FLUID" volume "MixedVolume"
physics create btype "WALL" face "L1" "R1" "T1" "RR1" "LL1" "R2" "RR2" "L2" \
  "LL2" "R3" "L3" "T2" "LL3" "Solid1" "Solid2" "Solid3"
physics create "sample inlet" btype "MASS_FLOW_INLET" face "face.21"
physics create "sheath1" btype "MASS_FLOW_INLET" face "IN1"
physics create "sheath2" btype "MASS_FLOW_INLET" face "IN2"
physics create "outlet" btype "OUTFLOW" face "out"
save
export fluent5 "Model 2.msh"
save
```

Shape 2.jou

```
vertex create "1" coordinates 0 -0.75 4.7547
vertex create "2" coordinates 0 -0.75 1.2547
vertex create "3" coordinates 2 -0.75 1.2547
vertex create "4" coordinates 2 0.25 1.2547
vertex create "5" coordinates 2 0.25 4.7547
vertex create "6" coordinates 0 0.25 4.7547
vertex create "7" coordinates 0 0.25 1.2547
vertex create "8a" coordinates 3 -0.2 2.9547
vertex create "8b" coordinates 3 -0.2 3.0547
vertex create "8c" coordinates 3 -0.3 3.0547
vertex create "8d" coordinates 3 -0.3 2.9547
vertex create "9" coordinates 2 -0.75 4.7547
vertex create "10" coordinates 0 -0.75 0
vertex create "11" coordinates 0 0.25 0
vertex create "12" coordinates 0 0.25 6.0094
vertex create "13" coordinates 0 -0.75 6.0094
vertex create "16" coordinates 7.9765 0.25 3.1547
vertex create "17" coordinates 7.9765 -0.25 3.1547
vertex create "18" coordinates 7.1105 -0.75 3.1547
vertex create "19" coordinates 7.1105 -0.75 2.8547
vertex create "20" coordinates 7.9765 -0.25 2.8547
vertex create "21" coordinates 7.9765 0.25 2.8547
vertex create "24" coordinates 11.9765 0.25 2.8547
vertex create "25" coordinates 11.9765 -0.25 2.8547
vertex create "26" coordinates 11.9765 -0.25 3.1547
vertex create "27" coordinates 11.9765 0.25 3.1547
vertex create "101a" coordinates 0.28571 0.25 0.24756
vertex create "102a" coordinates 0.57143 0.25 0.26184
vertex create "103a" coordinates 0.85714 0.25 0.24756
vertex create "104a" coordinates 1.14286 0.25 0.27613
vertex create "105a" coordinates 1.42857 0.25 0.29041
vertex create "106a" coordinates 1.71429 0.25 0.29041
vertex create "107a" coordinates 2 0.25 0.29041
vertex create "108a" coordinates 2.28571 0.25 0.31899
vertex create "109a" coordinates 2.57143 0.25 0.33327
vertex create "22a" coordinates 2.85714 0.25 0.39041
vertex create "111a" coordinates 3.14286 0.25 0.47613
vertex create "112a" coordinates 3.42857 0.25 0.59041
vertex create "113a" coordinates 3.71429 0.25 0.76184
vertex create "114a" coordinates 4 0.25 0.96184
vertex create "115a" coordinates 4.28571 0.25 1.09041
vertex create "116a" coordinates 4.57143 0.25 1.21899
vertex create "117a" coordinates 4.85714 0.25 1.36184
vertex create "118a" coordinates 5.14286 0.25 1.54756
vertex create "119a" coordinates 5.42857 0.25 1.66184
vertex create "120a" coordinates 5.71429 0.25 1.83327
vertex create "121a" coordinates 6 0.25 1.97613
vertex create "122a" coordinates 6.28571 0.25 2.11899
vertex create "123a" coordinates 6.57143 0.25 2.23327
vertex create "124a" coordinates 6.85714 0.25 2.4047
vertex create "125a" coordinates 7.14286 0.25 2.54756
vertex create "126a" coordinates 7.42857 0.25 2.67613
vertex create "22b" coordinates 2.85714 -0.25 0.39041
vertex create "111b" coordinates 3.14286 -0.25 0.47613
vertex create "112b" coordinates 3.42857 -0.25 0.59041
vertex create "113b" coordinates 3.71429 -0.25 0.76184
vertex create "114b" coordinates 4 -0.25 0.96184
vertex create "115b" coordinates 4.28571 -0.25 1.09041
vertex create "116b" coordinates 4.57143 -0.25 1.21899
vertex create "117b" coordinates 4.85714 -0.25 1.36184
vertex create "118b" coordinates 5.14286 -0.25 1.54756
vertex create "119b" coordinates 5.42857 -0.25 1.66184
```

```
vertex create "120b" coordinates 5.71429 -0.25 1.83327
vertex create "121b" coordinates 6 -0.25 1.97613
vertex create "122b" coordinates 6.28571 -0.25 2.11899
vertex create "123b" coordinates 6.57143 -0.25 2.23327
vertex create "124b" coordinates 6.85714 -0.25 2.4047
vertex create "125b" coordinates 7.14286 -0.25 2.54756
vertex create "126b" coordinates 7.42857 -0.25 2.67613
vertex create "101c" coordinates 0.28571 -0.75 0.24756
vertex create "102c" coordinates 0.57143 -0.75 0.26184
vertex create "103c" coordinates 0.85714 -0.75 0.24756
vertex create "104c" coordinates 1.14286 -0.75 0.27613
vertex create "105c" coordinates 1.42857 -0.75 0.29041
vertex create "106c" coordinates 1.71429 -0.75 0.29041
vertex create "23" coordinates 2 -0.75 0.29041
vertex create "108c" coordinates 2.28571 -0.75 0.39041
vertex create "109c" coordinates 2.57143 -0.75 0.47613
vertex create "110c" coordinates 2.85714 -0.75 0.59041
vertex create "111c" coordinates 3.14286 -0.75 0.76184
vertex create "112c" coordinates 3.42857 -0.75 0.96184
vertex create "113c" coordinates 3.71429 -0.75 1.09041
vertex create "114c" coordinates 4 -0.75 1.21899
vertex create "115c" coordinates 4.28571 -0.75 1.36184
vertex create "116c" coordinates 4.57143 -0.75 1.54756
vertex create "117c" coordinates 4.85714 -0.75 1.66184
vertex create "118c" coordinates 5.14286 -0.75 1.83327
vertex create "119c" coordinates 5.42857 -0.75 1.97613
vertex create "120c" coordinates 5.71429 -0.75 2.11899
vertex create "121c" coordinates 6 -0.75 2.23327
vertex create "122c" coordinates 6.28571 -0.75 2.4047
vertex create "123c" coordinates 6.57143 -0.75 2.54756
vertex create "124c" coordinates 6.85714 -0.75 2.67613
vertex create "201a" coordinates 0.28571 0.25 5.76184
vertex create "202a" coordinates 0.57143 0.25 5.74756
vertex create "203a" coordinates 0.85714 0.25 5.76184
vertex create "204a" coordinates 1.14286 0.25 5.73327
vertex create "205a" coordinates 1.42857 0.25 5.71899
vertex create "206a" coordinates 1.71429 0.25 5.71899
vertex create "207a" coordinates 2 0.25 5.71899
vertex create "208a" coordinates 2.28571 0.25 5.69041
vertex create "209a" coordinates 2.57143 0.25 5.67613
vertex create "15a" coordinates 2.85714 0.25 5.61899
vertex create "211a" coordinates 3.14286 0.25 5.53327
vertex create "212a" coordinates 3.42857 0.25 5.41899
vertex create "213a" coordinates 3.71429 0.25 5.24756
vertex create "214a" coordinates 4 0.25 5.04756
vertex create "215a" coordinates 4.28571 0.25 4.91899
vertex create "216a" coordinates 4.57143 0.25 4.79041
vertex create "217a" coordinates 4.85714 0.25 4.64756
vertex create "218a" coordinates 5.14286 0.25 4.46184
vertex create "219a" coordinates 5.42857 0.25 4.34756
vertex create "220a" coordinates 5.71429 0.25 4.17613
vertex create "221a" coordinates 6 0.25 4.03327
vertex create "222a" coordinates 6.28571 0.25 3.89041
vertex create "223a" coordinates 6.57143 0.25 3.77613
vertex create "224a" coordinates 6.85714 0.25 3.6047
vertex create "225a" coordinates 7.14286 0.25 3.46184
vertex create "226a" coordinates 7.42857 0.25 3.33327
vertex create "15b" coordinates 2.857142857 -0.25 5.618985714
vertex create "211b" coordinates 3.142857143 -0.25 5.533271429
vertex create "212b" coordinates 3.428571429 -0.25 5.418985714
vertex create "213b" coordinates 3.714285714 -0.25 5.247557143
vertex create "214b" coordinates 4 -0.25 5.047557143
vertex create "215b" coordinates 4.285714286 -0.25 4.918985714
vertex create "216b" coordinates 4.571428571 -0.25 4.790414286
vertex create "217b" coordinates 4.857142857 -0.25 4.647557143
```

```
vertex create "218b" coordinates 5.142857143 -0.25 4.461842857
vertex create "219b" coordinates 5.428571429 -0.25 4.347557143
vertex create "220b" coordinates 5.714285714 -0.25 4.176128571
vertex create "221b" coordinates 6 -0.25 4.033271429
vertex create "222b" coordinates 6.285714286 -0.25 3.890414286
vertex create "223b" coordinates 6.571428571 -0.25 3.776128571
vertex create "224b" coordinates 6.857142857 -0.25 3.6047
vertex create "225b" coordinates 7.142857143 -0.25 3.461842857
vertex create "226b" coordinates 7.428571429 -0.25 3.333271429
vertex create "201c" coordinates 0.28571 -0.75 5.76184
vertex create "202c" coordinates 0.57143 -0.75 5.74756
vertex create "203c" coordinates 0.85714 -0.75 5.76184
vertex create "204c" coordinates 1.14286 -0.75 5.73327
vertex create "205c" coordinates 1.42857 -0.75 5.71899
vertex create "206c" coordinates 1.71429 -0.75 5.71899
vertex create "14" coordinates 2 -0.75 5.71899
vertex create "208c" coordinates 2.28571 -0.75 5.61899
vertex create "209c" coordinates 2.57143 -0.75 5.53327
vertex create "210c" coordinates 2.85714 -0.75 5.41899
vertex create "211c" coordinates 3.14286 -0.75 5.24756
vertex create "212c" coordinates 3.42857 -0.75 5.04756
vertex create "213c" coordinates 3.71429 -0.75 4.91899
vertex create "214c" coordinates 4 -0.75 4.79041
vertex create "215c" coordinates 4.28571 -0.75 4.64756
vertex create "216c" coordinates 4.57143 -0.75 4.46184
vertex create "217c" coordinates 4.85714 -0.75 4.34756
vertex create "218c" coordinates 5.14286 -0.75 4.17613
vertex create "219c" coordinates 5.42857 -0.75 4.03327
vertex create "220c" coordinates 5.71429 -0.75 3.89041
vertex create "221c" coordinates 6 -0.75 3.77613
vertex create "222c" coordinates 6.28571 -0.75 3.6047
vertex create "223c" coordinates 6.57143 -0.75 3.46184
vertex create "224c" coordinates 6.85714 -0.75 3.33327
vertex create "132a" coordinates 2.22857 0.25 1.57613
vertex create "133a" coordinates 2.37143 0.25 1.71899
vertex create "134a" coordinates 2.48571 0.25 1.86184
vertex create "135a" coordinates 2.5 0.25 2.0047
vertex create "136a" coordinates 2.52857 0.25 2.14756
vertex create "137a" coordinates 2.62857 0.25 2.29041
vertex create "138a" coordinates 2.82857 0.25 2.43327
vertex create "139a" coordinates 2.91429 0.25 2.57613
vertex create "140a" coordinates 2.95714 0.25 2.71899
vertex create "141a" coordinates 3 0.25 2.86184
vertex create "132b" coordinates 2.22857 -0.75 1.57613
vertex create "133b" coordinates 2.37143 -0.75 1.71899
vertex create "134b" coordinates 2.48571 -0.75 1.86184
vertex create "135b" coordinates 2.5 -0.75 2.0047
vertex create "136b" coordinates 2.52857 -0.75 2.14756
vertex create "137b" coordinates 2.62857 -0.75 2.29041
vertex create "138b" coordinates 2.82857 -0.75 2.43327
vertex create "139b" coordinates 2.91429 -0.75 2.57613
vertex create "140b" coordinates 2.95714 -0.75 2.71899
vertex create "141b" coordinates 3 -0.75 2.86184
vertex create "232a" coordinates 3 0.25 3.14756
vertex create "233a" coordinates 2.95714 0.25 3.29041
vertex create "234a" coordinates 2.91429 0.25 3.43327
vertex create "235a" coordinates 2.82857 0.25 3.57613
vertex create "236a" coordinates 2.62857 0.25 3.71899
vertex create "237a" coordinates 2.52857 0.25 3.86184
vertex create "238a" coordinates 2.5 0.25 4.0047
vertex create "239a" coordinates 2.48571 0.25 4.14756
vertex create "240a" coordinates 2.37143 0.25 4.29041
vertex create "241a" coordinates 2.22857 0.25 4.43327
vertex create "232b" coordinates 3 -0.75 3.14756
vertex create "233b" coordinates 2.95714 -0.75 3.29041
```

```
vertex create "234b" coordinates 2.91429 -0.75 3.43327
vertex create "235b" coordinates 2.82857 -0.75 3.57613
vertex create "236b" coordinates 2.62857 -0.75 3.71899
vertex create "237b" coordinates 2.52857 -0.75 3.86184
vertex create "238b" coordinates 2.5 -0.75 4.0047
vertex create "239b" coordinates 2.48571 -0.75 4.14756
vertex create "240b" coordinates 2.37143 -0.75 4.29041
vertex create "241b" coordinates 2.22857 -0.75 4.43327
edge create "10-2" straight "10" "2"
edge create "1-13" straight "1" "13"
edge create "13-12" straight "13" "12"
edge create "12-6" straight "12" "6"
edge create "7-11" straight "7" "11"
edge create "11-10" straight "11" "10"
edge create "7-2" straight "7" "2"
edge create "6-1" straight "6" "1"
edge create "10-23" nurbs "10" "101c" "102c" "103c" "104c" "105c" "106c" "23" \
  interpolate
edge create "11-22a" nurbs "11" "101a" "102a" "103a" "104a" "105a" "106a" \
  "107a" "108a" "109a" "22a" interpolate
edge create "2-3" straight "2" "3"
edge create "7-4" straight "7" "4"
edge create "6-5" straight "5" "6"
edge create "1-9" straight "1" "9"
edge create "12-15a" nurbs "12" "201a" "202a" "203a" "204a" "205a" "206a" \
  "207a" "208a" "209a" "15a" interpolate
edge create "13-14" nurbs "13" "201c" "202c" "203c" "204c" "205c" "206c" "14" \
  interpolate
edge create "22a-b" straight "22a" "22b"
edge create "22b-23" straight "22b" "23"
edge create "23-19" nurbs "23" "108c" "109c" "110c" "111c" "112c" "113c" \
  "114c" "115c" "116c" "117c" "118c" "119c" "120c" "121c" "122c" "123c" \
  "124c" "19" interpolate
edge create "19-20" straight "20" "19"
edge create "20-21" straight "20" "21"
edge create "22a-21" nurbs "22a" "111a" "112a" "113a" "114a" "115a" "116a" \
  "117a" "118a" "119a" "120a" "121a" "122a" "123a" "124a" "125a" "126a" "21" \
  interpolate
edge create "22b-20" nurbs "22b" "111b" "112b" "113b" "114b" "115b" "116b" \
  "117b" "118b" "119b" "120b" "121b" "122b" "123b" "124b" "125b" "126b" "20" \
  interpolate
edge create "21-24" straight "21" "24"
edge create "20-25" straight "20" "25"
edge create "24-25" straight "24" "25"
edge create "27-24" straight "24" "27"
edge create "25-26" straight "25" "26"
edge create "26-27" straight "26" "27"
edge create "27-16" straight "16" "27"
edge create "16-17" straight "16" "17"
edge create "16-15a" nurbs "15a" "211a" "212a" "213a" "214a" "215a" "216a" \
  "217a" "218a" "219a" "220a" "221a" "222a" "223a" "224a" "225a" "226a" "16" \
  interpolate
edge create "17-15b" nurbs "15b" "211b" "212b" "213b" "214b" "215b" "216b" \
  "217b" "218b" "219b" "220b" "221b" "222b" "223b" "224b" "225b" "226b" "17" \
  interpolate
edge create "15a-15b" straight "15a" "15b"
edge create "14-15b" straight "14" "15b"
edge create "14-18" nurbs "14" "208c" "209c" "210c" "211c" "212c" "213c" \
  "214c" "215c" "216c" "217c" "218c" "219c" "220c" "221c" "222c" "223c" \
  "224c" "18" interpolate
edge create "17-18" straight "17" "18"
edge create "18-19" straight "18" "19"
edge create "17-20" straight "17" "20"
edge create "16-21" straight "16" "21"
edge create "4-3" straight "3" "4"
```

```
edge create "5-9" straight "5" "9"
edge create "26-17" straight "26" "17"
edge create "8a-b" straight "8a" "8b"
edge create "8b-c" straight "8b" "8c"
edge create "8c-d" straight "8c" "8d"
edge create "8d-a" straight "8a" "8d"
edge create "141a-232a" straight "141a" "232a"
edge create "232a-232b" straight "232a" "232b"
edge create "232b-141b" straight "232b" "141b"
edge create "141b-141a" straight "141b" "141a"
edge create "4-141a" nurbs "4" "132a" "133a" "134a" "135a" "136a" "137a" \
  "138a" "139a" "140a" "141a" interpolate
edge create "232a-5" nurbs "232a" "233a" "234a" "235a" "236a" "237a" "238a" \
  "239a" "240a" "241a" "5" interpolate
edge create "3-141b" nurbs "3" "132b" "133b" "134b" "135b" "136b" "137b" \
  "138b" "139b" "140b" "141b" interpolate
edge create "232b-9" nurbs "232b" "233b" "234b" "235b" "236b" "237b" "238b" \
  "239b" "240b" "241b" "9" interpolate
face create "out" wireframe "24-25" "27-24" "25-26" "26-27" real
face create "L1" wireframe "20-25" "25-26" "26-17" "17-20" real
face create "R1" wireframe "20-21" "21-24" "20-25" "24-25" real
face create "T1" wireframe "21-24" "27-24" "27-16" "16-21" real
face create "RR1" wireframe "26-27" "27-16" "26-17" "16-17" real
face create "LL1" wireframe "17-20" "19-20" "17-18" "18-19" real
face create "R2" wireframe "22a-b" "20-21" "22a-21" "22b-20" real
face create "RR2" wireframe "22b-23" "22b-20" "23-19" "19-20" real
face create "L2" wireframe "16-17" "16-15a" "17-15b" "15a-15b" real
face create "LL2" wireframe "17-15b" "14-15b" "14-18" "17-18" real
face create "R3" wireframe "11-10" "10-23" "11-22a" "22a-b" "22b-23" real
face create "L3" wireframe "13-12" "12-15a" "13-14" "15a-15b" "14-15b" real
face create "T2" wireframe "11-22a" "22a-21" "16-21" "7-11" "7-4" "4-141a" \
  "141a-232a" "232a-5" "6-5" "12-6" "12-15a" "16-15a" real
face create "LL3" wireframe "18-19" "23-19" "10-23" "10-2" "2-3" "3-141b" \
  "232b-141b" "232b-9" "1-9" "1-13" "13-14" "14-18" real
face create "IN1" wireframe "10-2" "7-11" "11-10" "7-2" real
face create "Solid1" wireframe "7-2" "2-3" "7-4" "4-3" real
face create "Solid2" wireframe "141a-232a" "141b-141a" "232b-141b" \
  "232a-232b" real
face create "Solid2R" wireframe "4-141a" "4-3" "3-141b" "141b-141a"
face create "Solid2L" wireframe "232a-5" "232a-232b" "232b-9" "5-9"
face create "Solid3" wireframe "6-5" "1-9" "5-9" "6-1" real
face create "IN2" wireframe "1-13" "13-12" "12-6" "6-1" real
volume create "MixedVolume" stitch "out" "L1" "R1" "T1" "RR1" "LL1" "R2" \
  "RR2" "L2" "LL2" "R3" "L3" "T2" "LL3" "IN1" "Solid1" "Solid2R" "Solid2" \
  "Solid2L" "Solid3" "IN2" real
face create "Sample inlet" wireframe "8a-b" "8b-c" "8c-d" "8d-a" real
face split "Solid2" connected face "Sample inlet"
volume mesh "MixedVolume" tetrahedral size 0.11
volume smooth "MixedVolume" fixed lwlaplacian
physics create ctype "FLUID" volume "MixedVolume"
physics create btype "WALL" face "L1" "R1" "T1" "RR1" "LL1" "R2" "RR2" "L2" \
  "LL2" "R3" "L3" "T2" "LL3" "Solid1" "Solid2R" "Solid2" "Solid2L" "Solid3"
physics create "sheath1" btype "MASS_FLOW_INLET" face "IN1"
physics create "sheath2" btype "MASS_FLOW_INLET" face "IN2"
physics create "outlet" btype "OUTFLOW" face "out"
physics create "sample inlet" btype "MASS_FLOW_INLET" face "face.23"
save
export fluent5 "newshape2.msh"
```

Gambit Grid Generation Procedures

Option A:

1. Open Gambit and select folder where Shape 2m.jou has been saved as the working directory.
2. Go to File>Run Journal and manually find Shape 2m.jou.

Option B:

1. Type and enter each line of Shape 2m.jou in gambit command line. (Note that '\' signifies a continuation of the command on the next line in the '.jou' file)

Repeat the same procedure for Shape 2.jou

Fluent Procedures

1. Start Fluent 3ddp
2. Go to File>Read>Case and select Shape 2m.msh in the Gambit working directory.
3. Go to Grid>Scale and select grid was generated in mm and click scale.
4. Go to Define>Models>Multiphase and select mixture, slip, body force and 2 phases.
5. Go to Define>Models>Discrete Phase and select interaction with continuous phase, 5 iterations per DPM, 5500 Maximum number of steps, non-spherical drag law, and shape factor 5
6. Go to Define>Models>Discrete Phase>Injections>Create and select injection name 'o1', injection type 'single', particle type 'inert', material type 'Calcium Oxide' and specify starting point (sample inlet nozzle), diameter and other properties of the particle.
7. Go to Define>Materials
    a. Upload liquid water from fluent data base
    b. Create blood plasma fluid

c. Create blood cells solid

8. Go to Define>Phases
    a. Set water-liquid as primary phase
    b. Set blood-plasma as secondary phase
9. Go to Define>Boundary Conditions
    a. Set sample_inlet
        i. Water => mdot = 0
        ii. Blood plasma => mdot = xx
    b. Set Sheath 1
        i. Water => mdot = xx
        ii. Blood plasma => mdot = 0
    c. Repeat (b) for Sheath 2
10. Go to Define>Injections
    a. Set injection '01' and correct the material to blood cells
    b. Create more injections (01 to say 20) and distribute starting points at the sample inlet
11. Go to Solutions>Monitor>Residuals and set convergence criterion to 5e-04
12. Go to Solutions>Initialize>Initialize
    a. Select compute from Sample_inlet
13. Go to Solutions>Iterate and set number of iterations and click iterate to start program

Repeat the same procedures for Shape 2.msh and other flow rates.

APPENDIX A.10: FLOW CHAMBER OPTIMIZED PROFILES CURVE FIT

Table A.9: Optimized profile data for tapering flow chamber wall

x	z
0.0000	2.8286
0.2857	2.7571
0.5714	2.7429
0.8571	2.7571
1.1429	2.7286
1.4286	2.7143
1.7143	2.7143
2.0000	2.7143
2.2857	2.6857
2.5714	2.6714
2.8571	2.6143
3.1429	2.5286
3.4286	2.4143
3.7143	2.2429
4.0000	2.0429
4.2857	1.9143
4.5714	1.7857
4.8571	1.6429
5.1429	1.4571
5.4286	1.3429
5.7143	1.1714
6.0000	1.0286
6.2857	0.8857
6.5714	0.7714
6.8571	0.6000
7.1429	0.4571
7.4286	0.3286

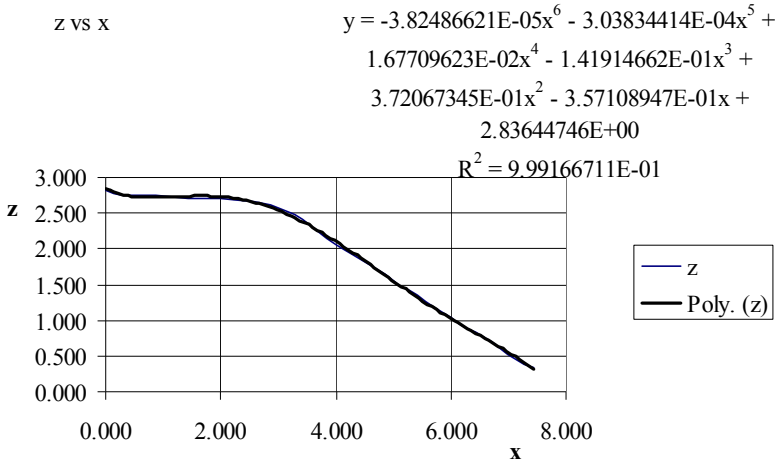

Figure A.9: Curve fit for optimized profile on flow cytometer sides

Table A.10: Optimized Sample inlet wall profile data

Left	
z	x
3.0047	3.0000
3.1476	3.0000
3.2904	2.9571
3.4333	2.9143
3.5761	2.8286
3.7190	2.6286
3.8618	2.5286
4.0047	2.5000
4.1476	2.4857
4.2904	2.3714
4.4333	2.2286
4.5761	2.0000

Right	
z	x
1.4333	2.0000
1.5761	2.2286
1.7190	2.3714
1.8618	2.4857
2.0047	2.5000
2.1476	2.5286
2.2904	2.6286
2.4333	2.8286
2.5761	2.9143
2.7190	2.9571
2.8618	3.0000
3.0047	3.0000

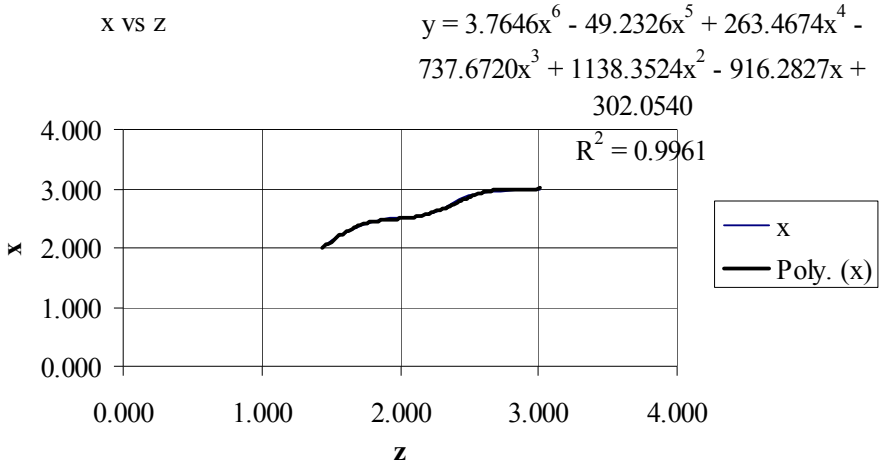

Figure A.10: Curve fit for optimized profile on flow sample inlet left side

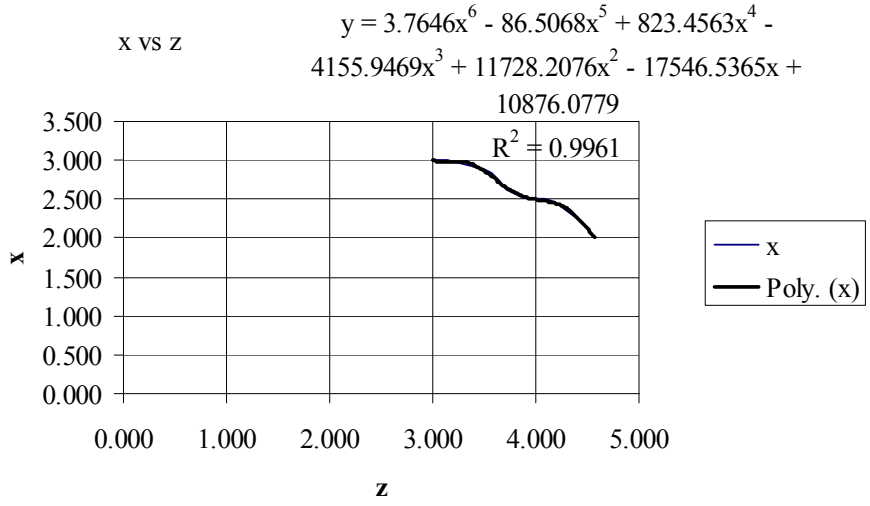

Figure A.11: Curve fit for optimized profile on flow sample inlet left side

APPENDIX A.11: ADDITIONAL FLOW CYTOMETRY SIMULATION RESULTS

This section shows a side-by-side comparison of the original flow cytometer design and the optimized design. This section was created to avoid having too many figures in the main body and as well draw conclusions from here and put in the chapter 3. The simulations here covers Re = 0.01 to 1600. (See section 3.5.3 where this section is referred to.)

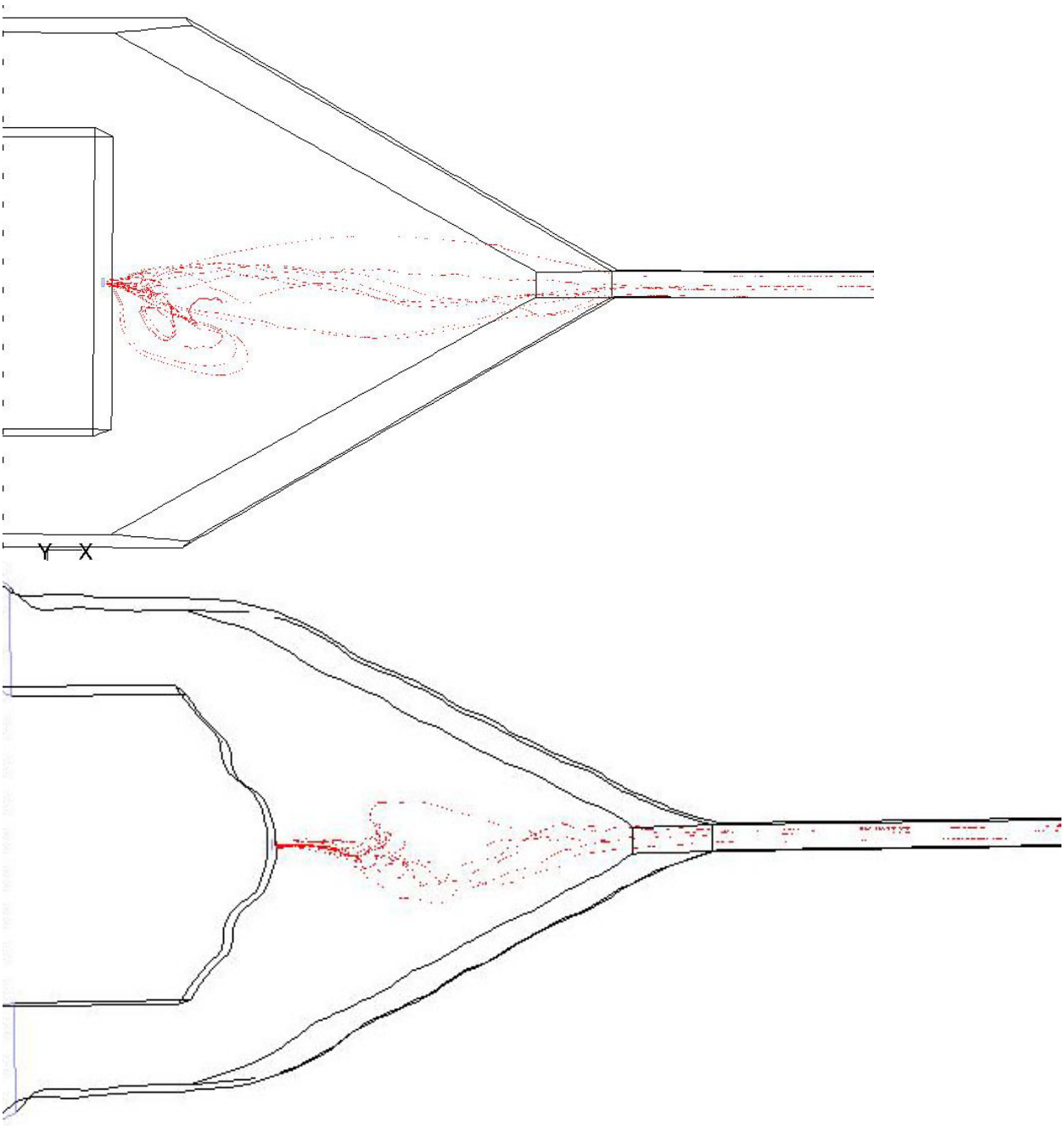

Figure A.12: Blood cells trajectories for sheath flow = 0.000576 kg/s

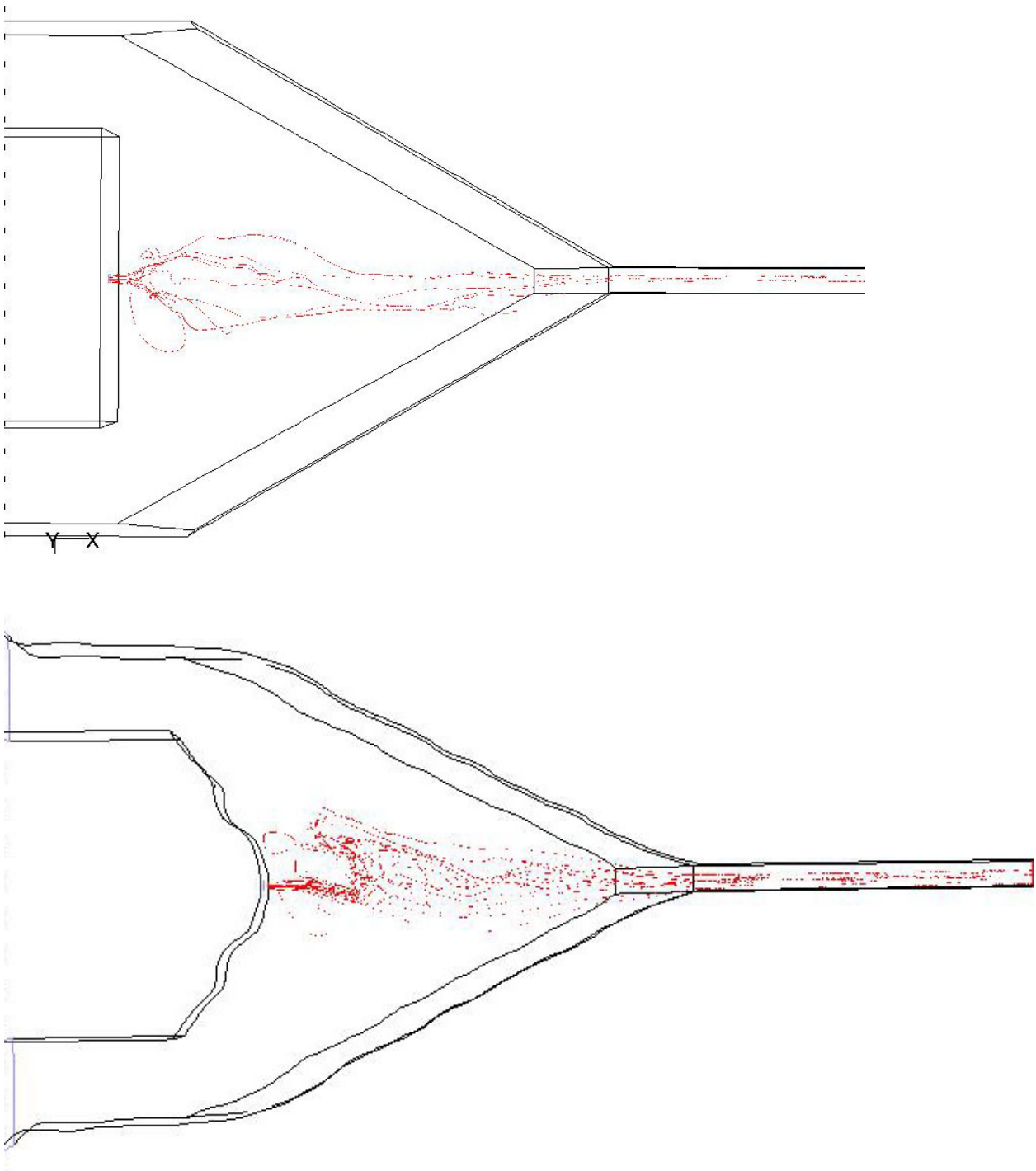

Figure A.13: Blood cells trajectories for sheath flow = 0.000504 kg/s

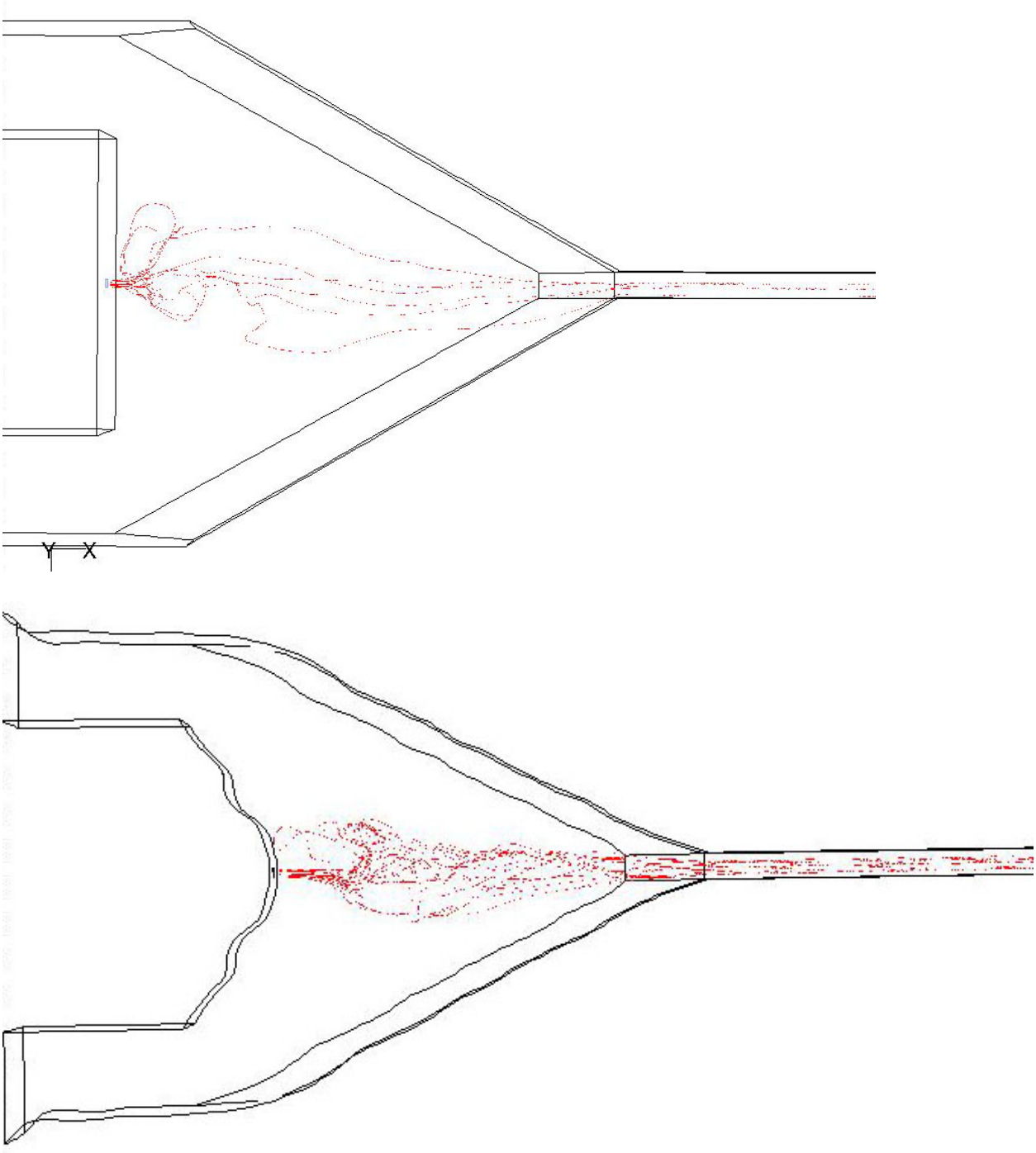

Figure A.14: Blood cells trajectories for sheath flow = 0.000432 kg/s

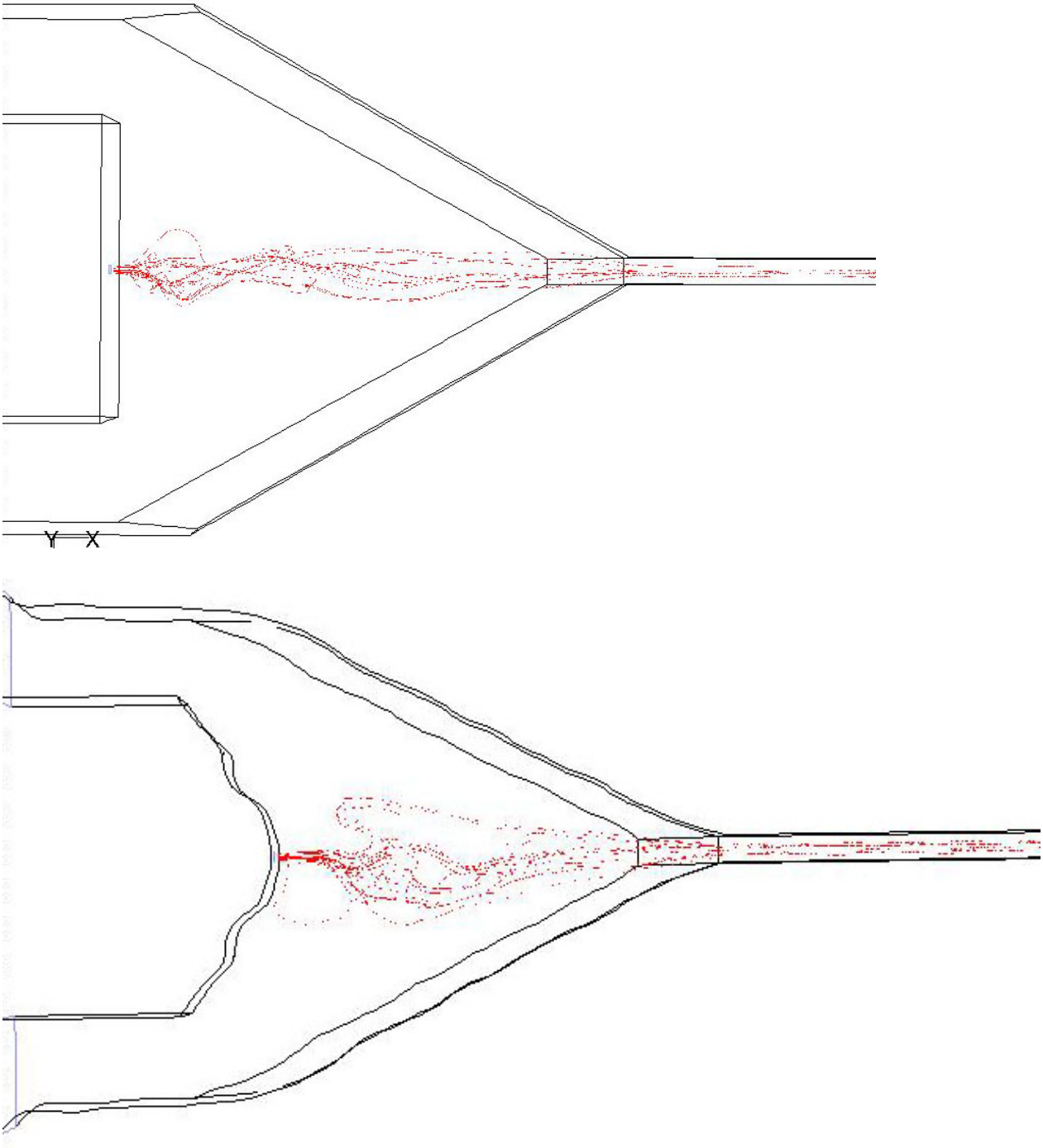

Figure A.15: Blood cells trajectories for sheath flow = 0.00036 kg/s

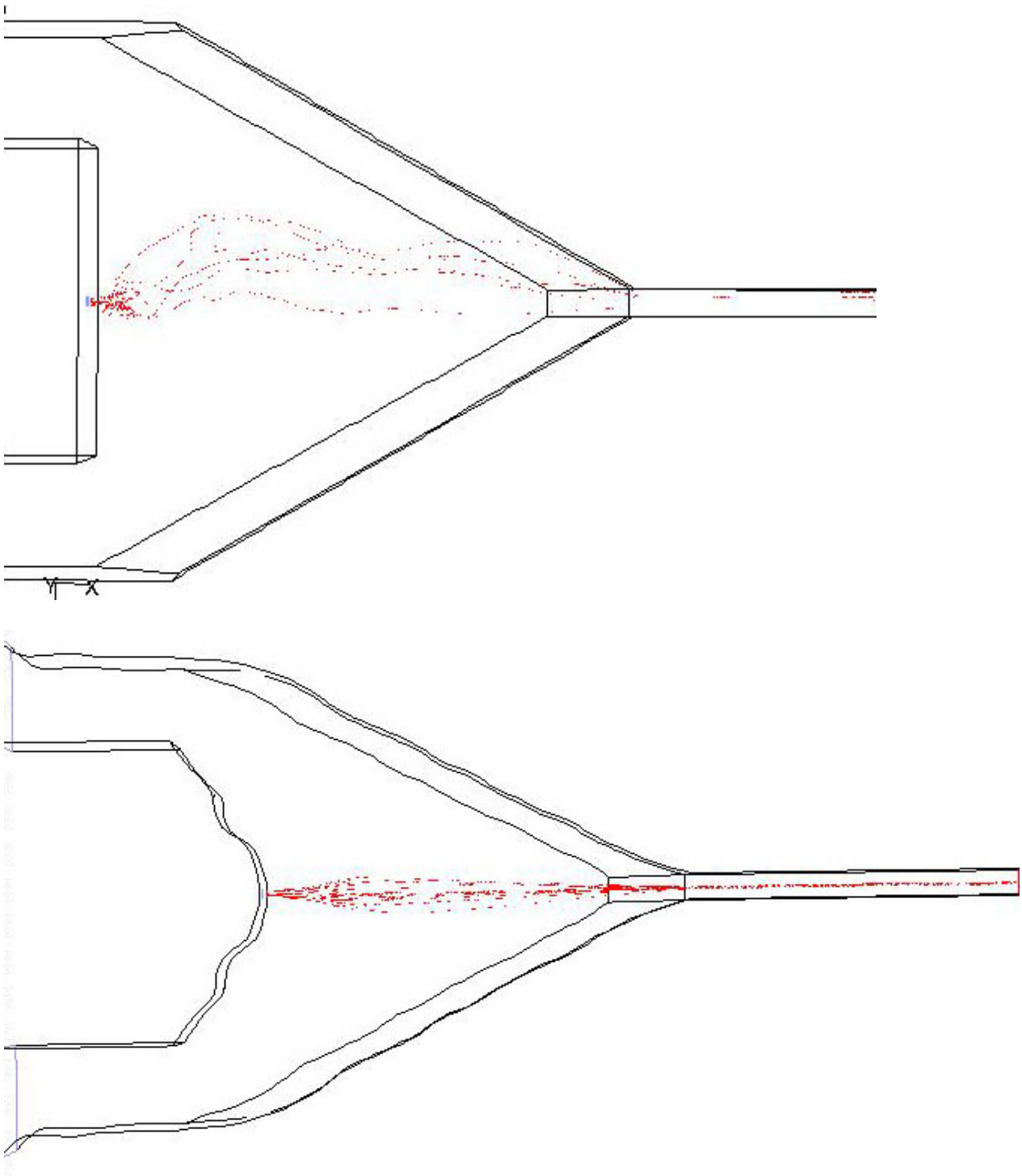

Figure A.16: Blood cells trajectories for sheath flow = 0.000288 kg/s

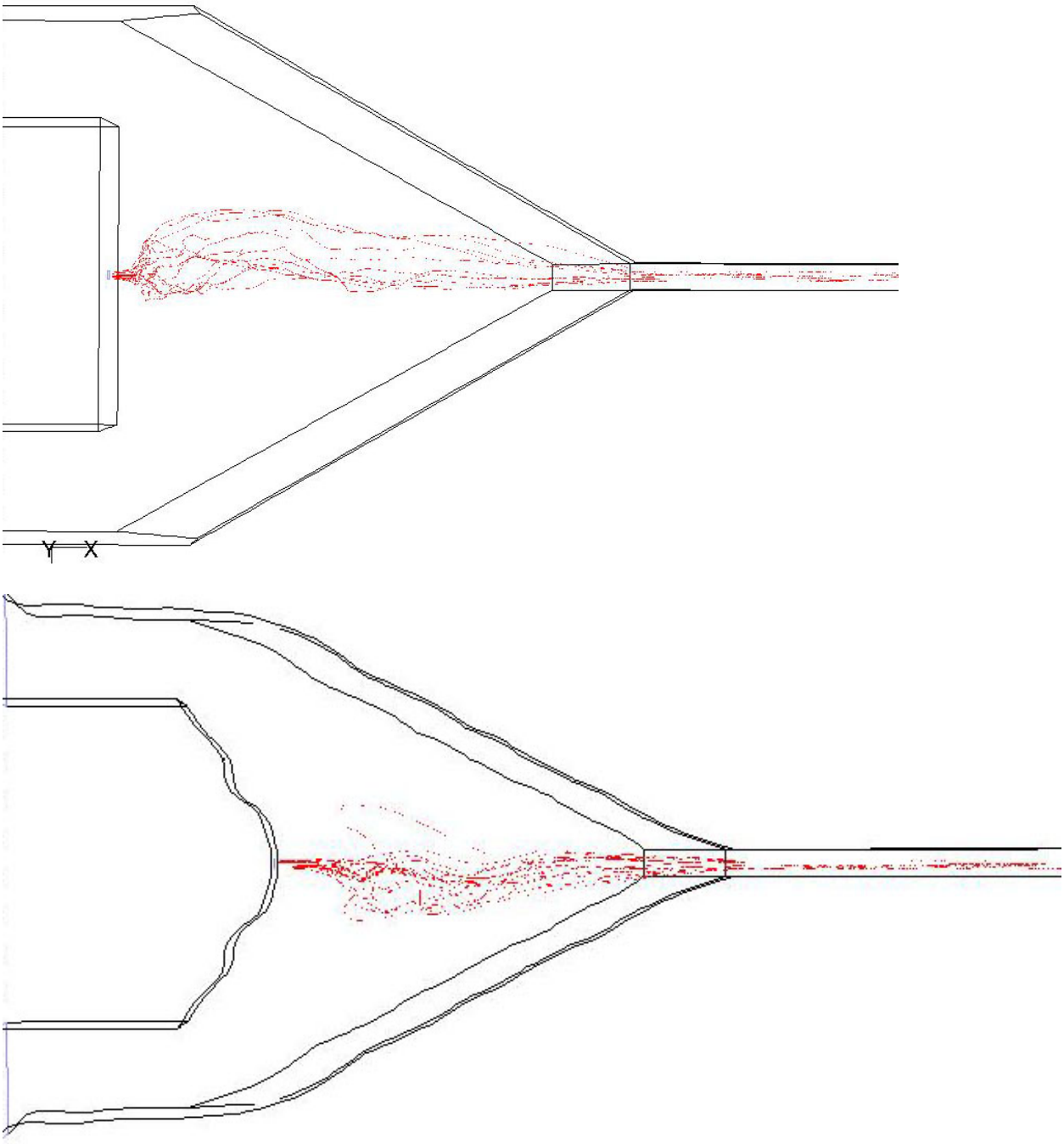

Figure A.17: Blood cells trajectories for sheath flow = 0.000216 kg/s

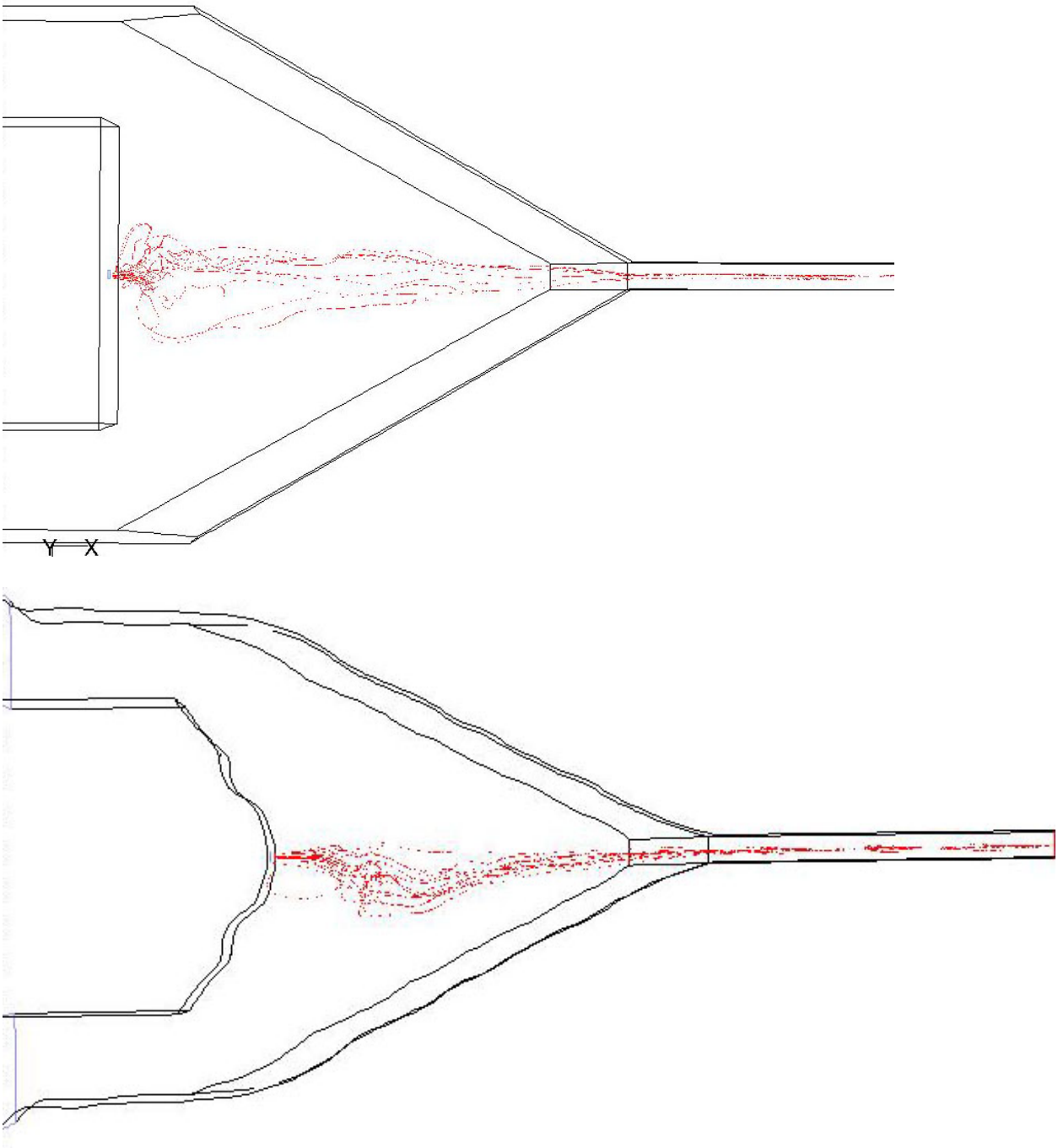

Figure A.18: Blood cells trajectories for sheath flow = 0.000144 kg/s

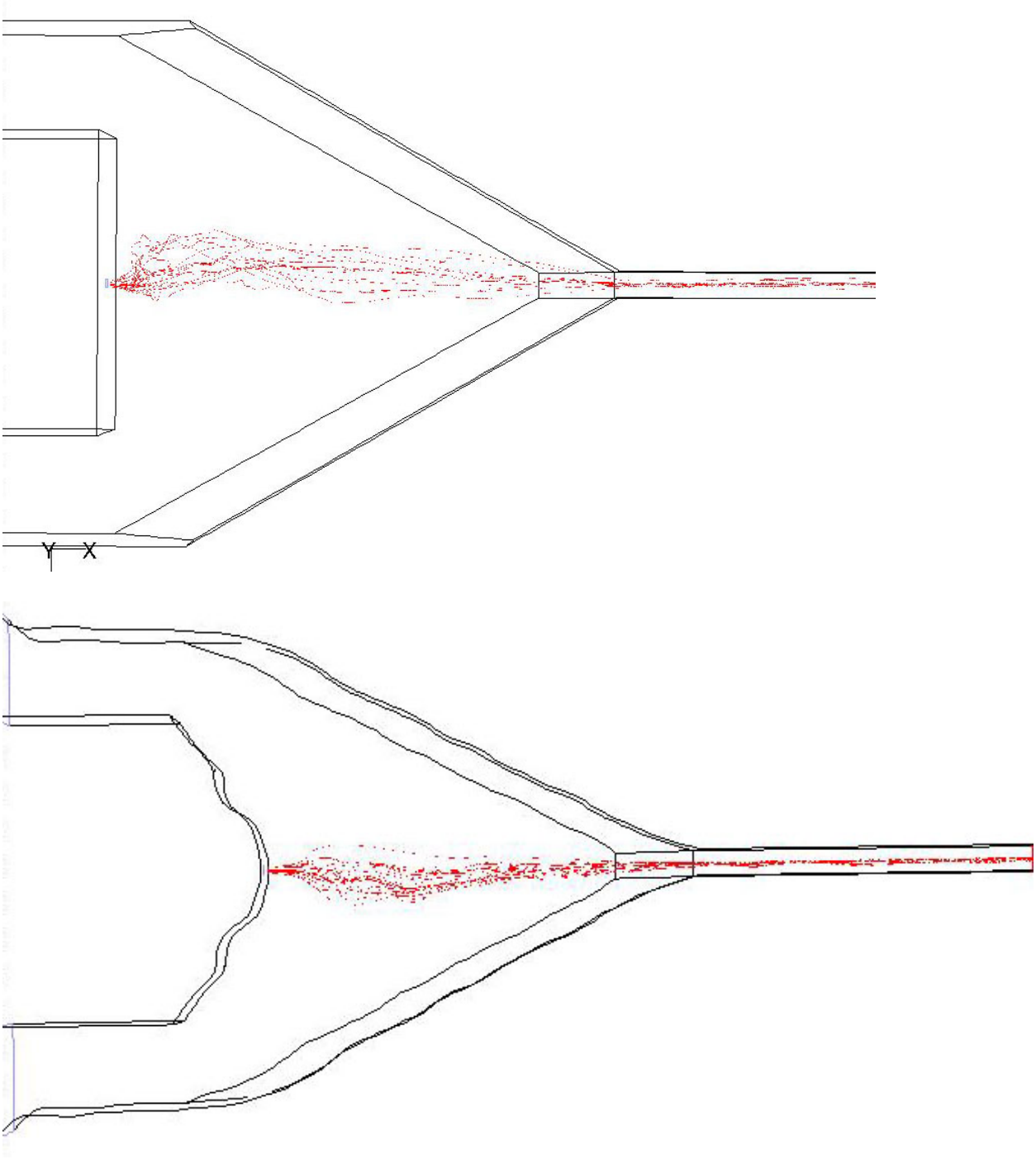

Figure A.19: Blood cells trajectories for sheath flow = 7.2 e-5 kg/s

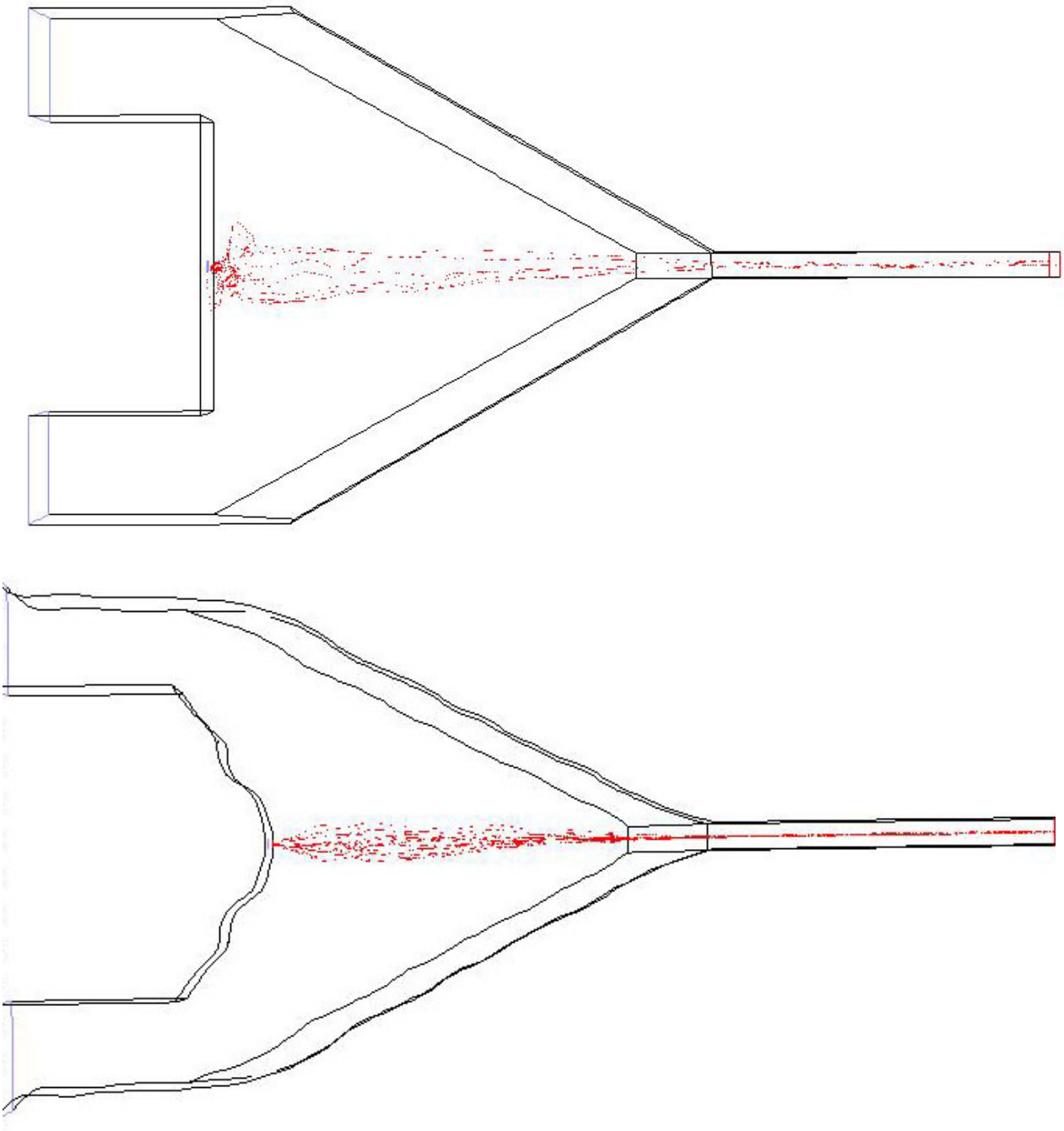

Figure A.20: Blood cells trajectories for sheath flow = 3.6 e-5 kg/s

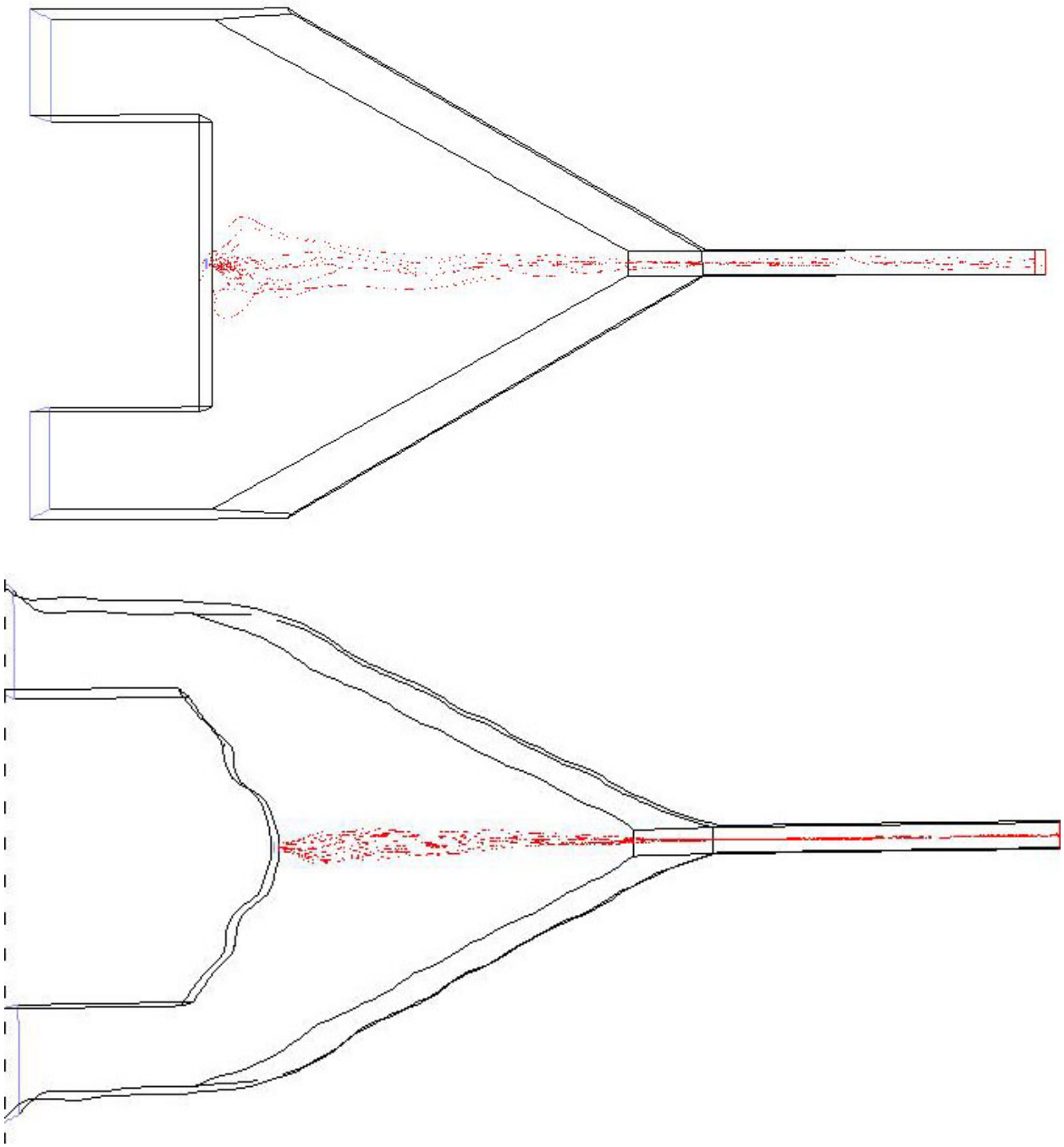

Figure A.21: Blood cells trajectories for sheath flow = 1.8 e-5 kg/s

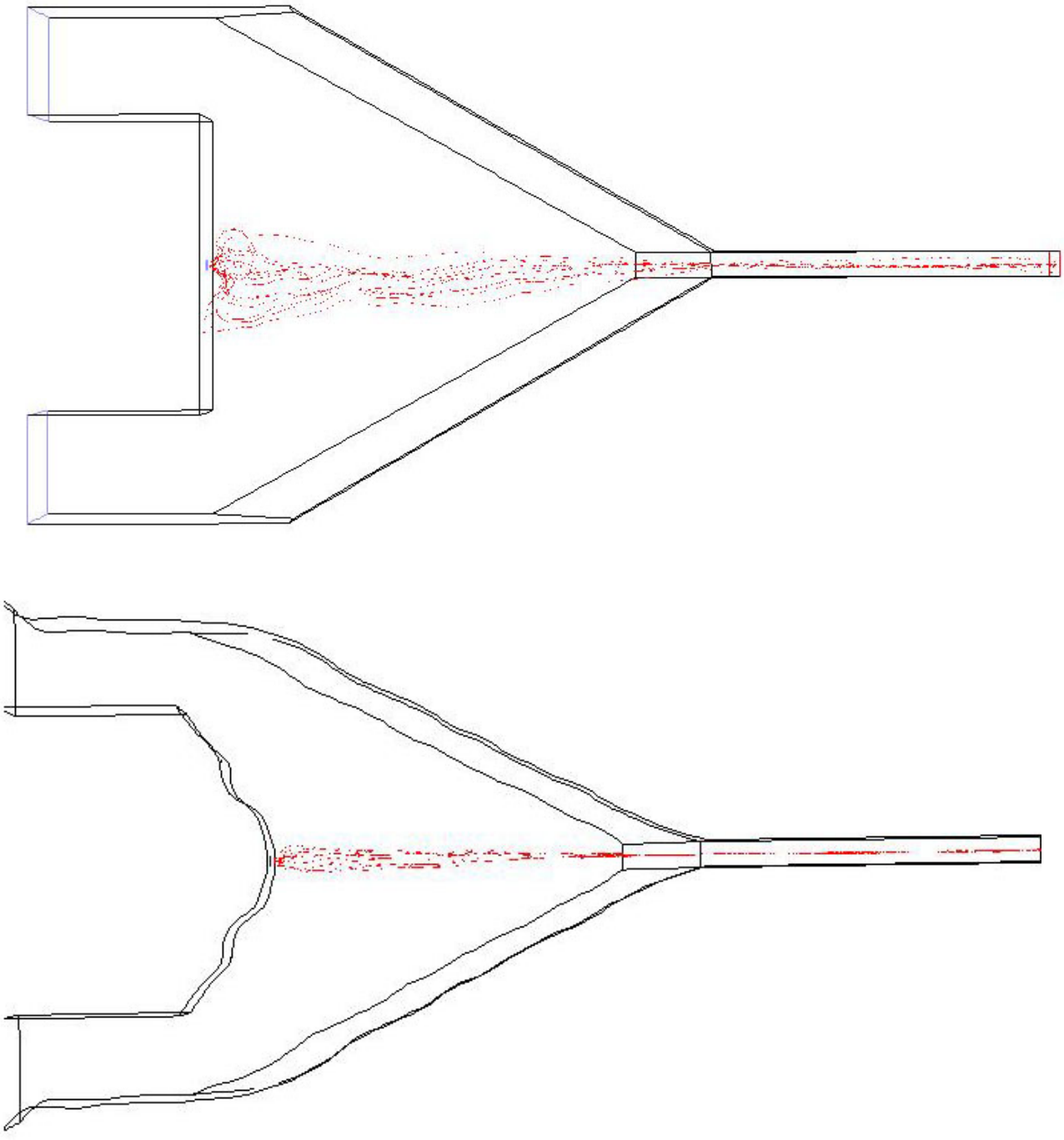

Figure A.22: Blood cells trajectories for sheath flow = 3.6 e-6 kg/s

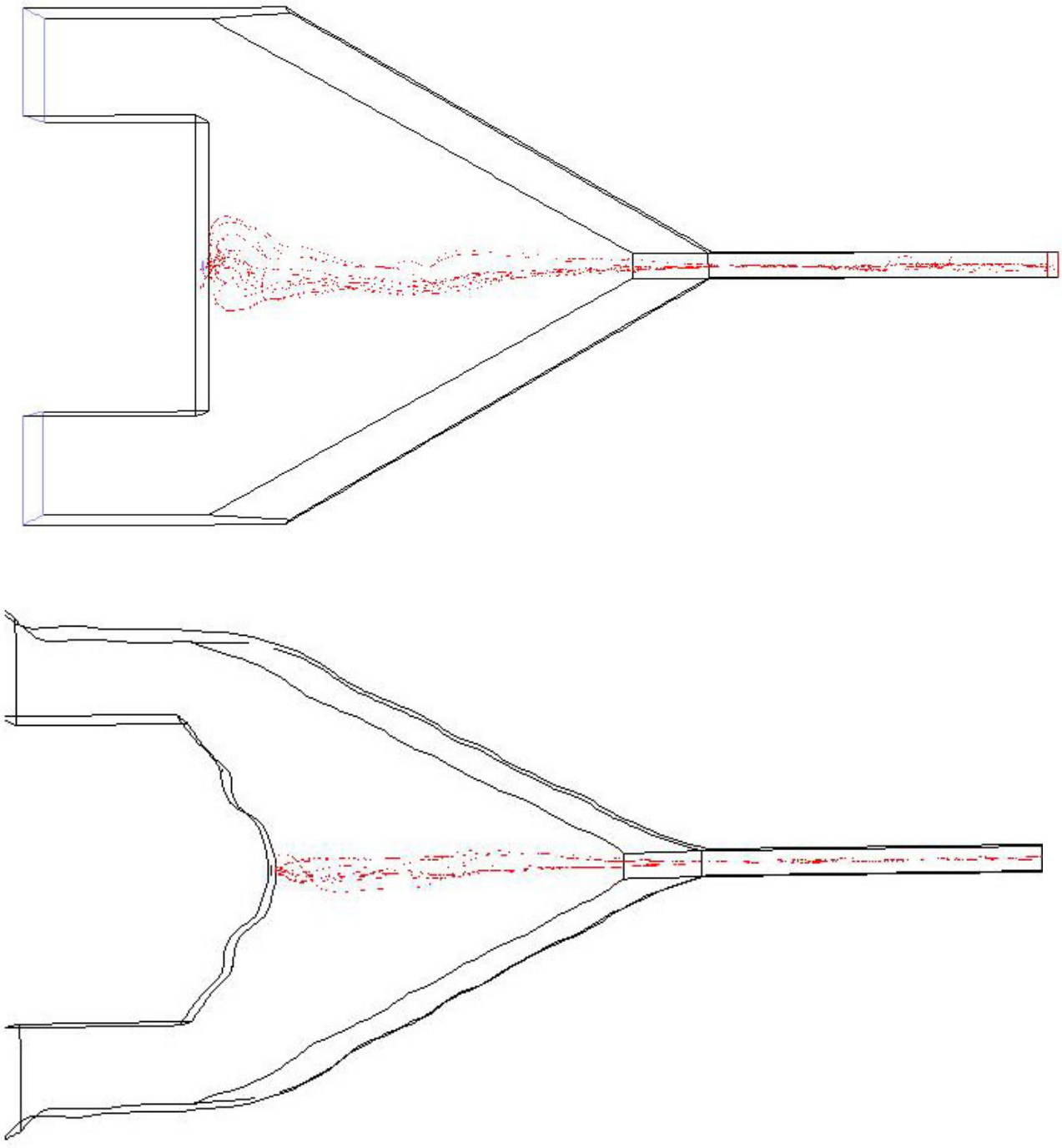

Figure A.23: Blood cells trajectories for sheath flow = 3.6 e-7 kg/s

APPENDIX A.12: INTRODUCTION TO COMPUTATIONAL FLUID DYNAMICS

A.12.1 Background

The equations that govern fluid dynamics problems are differential equations which usually contain non-linear terms. These equations are the continuity, the Navier-Stokes and the energy equations. In some cases, the non-linear terms are negligibly small and can be neglected, so analytical methods can be used to solve the equations. However, in most practical fluid dynamics cases, the non-linear terms are not negligible, so the non-linearity in the equations makes it very difficult to solve analytically. Then numerical methods are needed to obtain the solutions. Invention and advances in high-speed and large-memory computers has enabled engineers to numerically solve complex fluid dynamics problems with a high degree of accuracy. The use of computers to numerically solve fluid dynamics problems is called Computational Fluid Dynamics (CFD) [23].

Modern CFD applications (or softwares) consist of 3 main parts, namely; Preprocessor, Flow Solver and Postprocessor.

1. **Preprocessor:** The preprocessor is used to input the problem geometric model, generate the grid, define flow parameters and define boundary conditions.
2. **Flow Solver:** The flow solver is used to solve the governing equations of fluid flow subject to conditions provided. The solver is an algorithm based on a numerical method.
3. **Postprocessor:** The postprocessor is used to present the results in graphical and easy to read format.

A.12.2 Numerical Method Used in CFD

The main numerical methods used in CFD are the finite difference method (FDM), the finite element method (FEM), the finite volume method (FVM, and the spectral method.

The finite difference method uses the Taylor series expansion to write the derivatives of a variable as the difference between the values of various points in space or time. FDM is easy to formulate. However, for multidimensional problems, meshes must be structured in either 2-D or 3-D. Curved meshes must be transformed into orthogonal Cartesian coordinates, so that the finite difference equations can be written on structure Cartesian meshes. Neuman boundary conditions can only be approximated, not exactly enforced [33].

The finite element method involves dividing the fluid domain under consideration into finite number of sub-domains, known as elements. A simple function is assumed for the variation of each variable inside the element. The summation of variations of variables in each element is used to describe the whole flow domain. FEM formulation requires more mathematical effort than the FDM. FEM easily accommodates complex geometries and unstructured meshes, so no coordinated transformation is needed. Neumann Boundary conditions are enforced exactly.

Finite volume method involves subdividing the fluid flow domain into a finite number of small control volumes. The division of volume is done using a grid which defines the control volume boundaries. The control volumes are solved using either FDM or FEM. The sum of equations for all the control volumes gives a general equation of desired variable for the domain of fluid flow. FVM easily accommodates complex geometries and unstructured meshes, so no coordinate transformation is need.

Spectral method involves solving the governing equations by using Fourier series or series of Chebyshev polynomials to approximate the unknown functions. The numerical process in this method involves generating constants and/or algebraic equations for the coefficients of the Fourier or Chebyshev's series.

The application of the briefed numerical methods involves iterating to arrive at a solution based on convergence criterion, boundary conditions, and initial conditions. However, if the fluid

dynamics problem is set up under simple conditions with negligible non-linearity, modern CFDs have the capability to automatically solve the flow problem using standard solution equation without numerical iterations.

A.12.3 Mesh Generation (or Grid Generation)

The most cumbersome and time consuming part of CFD is the mesh generation. It is usually the first step and it has big effect on the final solutions of the fluid flow problem. The mesh consists of a set of points called nodes. The nodes are connected by straight lines to form a set of areas and/or volumes called cells. The mesh is used to represent the flow field and boundaries. The smaller the cells in the mesh, the higher the degree of accuracy of the result. Too small mesh size may result in undesirable negative volume in the mesh, and small mesh cell size requires more computer memory and time. On the other hand, too big mesh cells size may result in loss of important variable gradient, because in CFD the computation values of dependent variables, such as velocity, pressure, temperature, etc, will be described for each cell or node. The computer cannot automatically generate the best mesh type and mesh cell size, so a high level of users' skill is required. The process of obtaining an appropriate mesh for a volume or area is called mesh generation. There are three types of mesh generation methods namely; structured, unstructured and hybrid mesh generation methods.

Structured grids have gridlines that forms a curvilinear coordinate system. The cells are rectangular in 2-D and hexagonal in 3-D. For complex geometries, it is preferable to use multiblocks structured grid. However, the application of structured grid to complex geometries is limited, which implies that it is not applicable to some complex geometries. Structured grids can be used with both FDM and FVM.

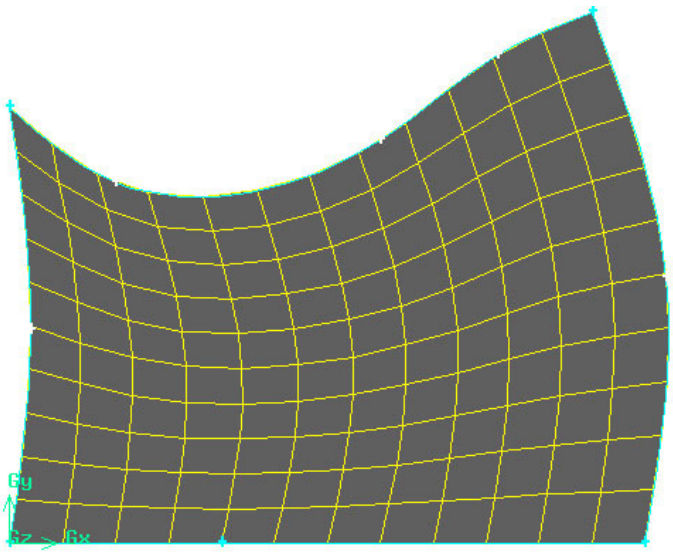

Figure A.24: Structured grid

Unstructured grids have grid lines that do not form curvilinear coordinate system. The grids are unstructured in orientation so it requires more complicated programming. The unstructured grids easily conform to shapes, so less grid generation time is required. Infact, the main advantage of unstructured grids is that they conform to any geometry. Unstructured grids can be used with both FVM and FEM.

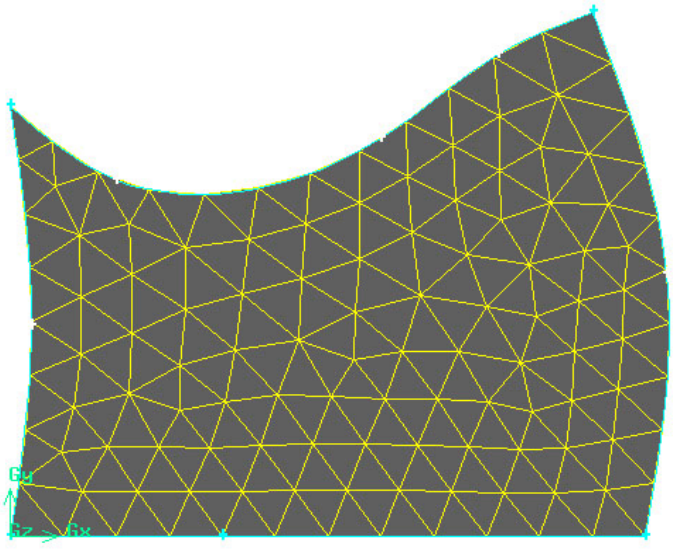

Figure A.25: Unstructured grid

Hybrid grids are a combination of both the structured and unstructured grids to obtain all the capabilities that can be obtained when using only the structured or unstructured grid. The diagram below shows some sample of sketches of the grid generation methods in 2-D.

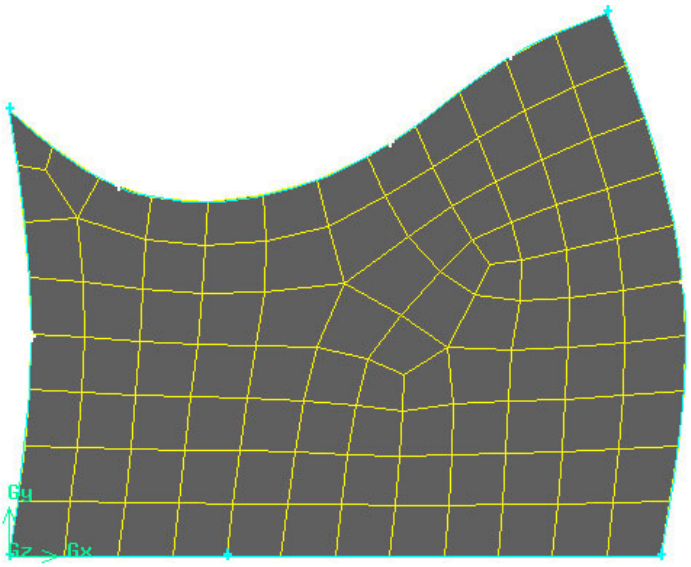

Figure A.26: Hybrid grid

A.12.4 Advantages and Applications of CFD

CFD, when done by an expert, provides results as good as experiments. Therefore, by using CFD, design flaws can be detected early and corrected before building an actual prototype. Consequently, CFD has the advantage of reducing cost.

CFD provides an alternative to analytically solving simple fluid dynamics problems.

Most importantly, CFD makes it possible to solve complex problems that can only be solved by numerical methods or by experimentation. Some of these complex areas of fluid flow that needs CFD application are:

1. Turbulent flows
2. Chemically reactive flows including combustion
3. Acoustics
4. Combined mode heat transfer, etc
5. Multiphase flow

VITA

Etim S Udoetok hails from Akwa Ibom state of Nigeria. He completed his high school with a concentration on science and mathematical subjects. He started his first 3 years in college at Abubakar Tafawa Balewa University (ATBU), Bauchi, Nigeria, where he majored in mechanical and production engineering and took most of the foundation engineering classes. Etim later transferred to Louisiana State University where he completed his Bachelor of Science in Mechanical Engineering degree program in May of 2004.

Etim's extra curricular activities include playing sports, watching sports, participating in social groups activities and so on.